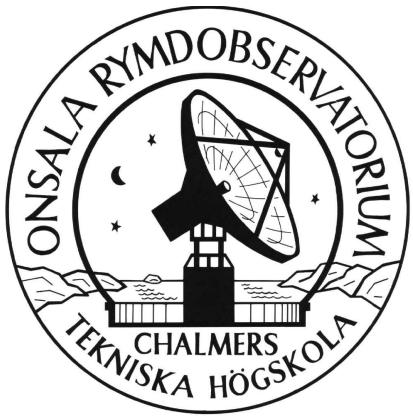

ASTROPHYSICAL DYNAMICS 1999/2000

Edited by

Alessandro B. Romeo

ASTROPHYSICAL DYNAMICS 1999/2000 **Edited by Alessandro B. Romeo**

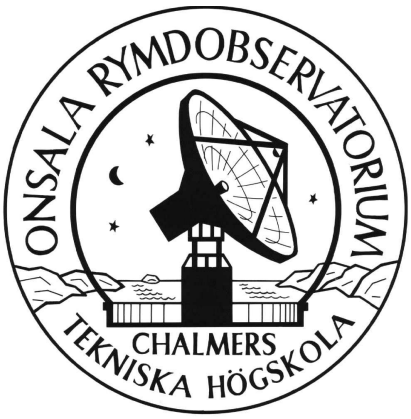

ASTROPHYSICAL DYNAMICS 1999/2000

Proceedings of the workshop held at
Onsala Space Observatory
12 and 13 January, and 1 March, 2000

—

Following a homonymous advanced research course held at
Chalmers University of Technology and Göteborg University
October–December 1999

—

Edited by

Alessandro B. Romeo

Onsala Space Observatory
Chalmers University of Technology
SE-43992 Onsala, Sweden
(romeo@oso.chalmers.se)

Onsala Space Observatory

2000

COVER ILLUSTRATION

This is not a medieval woodcut ...
(Cf. `http://www.earthvisions.net/flat_earth.htm`)

Credit: Camille Flammarion
Courtesy: History of Science Collections, University of Oklahoma
Digitization: Kerry Magruder (OU)
Colouring and Refinements: Alessandro B. Romeo & Achim Tappe (OSO)

Contents

Workshop Presentation and Hot Topics

Alessandro B. Romeo

Onsala Space Observatory
Chalmers University of Technology
SE-43992 Onsala, Sweden
(romeo@oso.chalmers.se)

*

Abstract

The workshop 'Astrophysical Dynamics 1999/2000' followed a homonymous advanced research course, and both activities were organized by me. In this opening paper of the proceedings book, I describe them and document their *strong* impact on the academic life of the local institutions.

1 Introduction

The advanced research course was held at Chalmers University of Technology and Göteborg University in October–December 1999; it was open to graduate students, senior researchers, and motivated under-graduate students with good background in physics and mathematics. The course covered several multi-disciplinary issues of modern research on astrophysical dynamics, and thus also of interest to physicists, mathematicians and engineers. The major topic was gas dynamics, viewed in context with stellar dynamics and plasma physics. The course was complemented by parallel seminars on hot topics given by experts in such fields, and open to a wide scientific audience. In particular, I gave a friendly introduction to *wavelets*, which are becoming an increasingly powerful tool not only for processing signals and images but also for analysing fractals and turbulence, and which promise to have important applications to dynamical modelling of disc galaxies. The course is presented in more detail in Sect. 2. The basic reference is Romeo (1999b); see also the references cited therein and in Sect. 2, and Romeo (1999a) for a discussion of my ideas about teaching (in a different context).

The workshop was held at Onsala Space Observatory on 12 and 13 January, and 1 March, 2000; it was open to a wide scientific audience. The workshop with published proceedings book was, as a matter of fact, the *innovative* form of exam that I proposed for the advanced research course. The contributions were refereed and their quality is high on average, exceptionally high in a few cases. The workshop is presented in more detail in Sect. 3.

*Astrophysical Dynamics 1999/2000, Alessandro B. Romeo (Ed.), Onsala Space Observatory, 2000.

The advanced research course and the workshop all together produced great enthusiasm in the students and welcomed the participation of a hundred different people, which means *an order of magnitude* more than an average graduate course at Chalmers University of Technology and Göteborg University. What else should I say? Enjoy reading the proceedings book!

2 The Advanced Research Course

2.1 Lectures

1. Basics about fluids (2 hours).
2. The equations of motion (4 hours).
3. Simple applications (4 hours).
4. Instabilities (4 hours).
5. Turbulences and fractals (2 hours).
6. Astrophysical fractals: interstellar medium and galaxies (1 hour).
   - References: Combes (1999b).
7. Which thermal physics for gravitationally unstable media? (1 hour).
   - References: Pfenniger (1998).
8. Shocks (4 hours).
9. Magnetic fields (4 hours).
10. Gas dynamics vs. stellar dynamics and plasma physics (2 hours).

References: Shu (1992), unless otherwise specified; see also van Dyke (1982), Shore (1992), Dyson & Williams (1997) and Choudhuri (1998).

2.2 Exercises

1. Birth, life (and death?) of a galaxy: a step-by-step problem (6 hours).

References: Padmanabhan (1996); see also Binney & Tremaine (1987) and Binney & Merrifield (1998).

2.3 Parallel Seminars on Hot Topics

1. 'Wavelets: A Presentation for Scientists' – Alessandro Romeo (2 hours).
   - Multimedia: computer-projector show using the Matlab Wavelet Toolbox, running on a high-performance Linux machine; public computer lab.
   - References: Press et al. (1992), Vetterling et al. (1992), Misiti et al. (1997), Hubbard (1998), Mallat (1998), Bergh et al. (1999) and Wavelet Digest.

2. 'Black-Hole Accretion Discs' – Marek Abramowicz (2 hours).

3. 'Wavelets at Work in Physics' – Alessandro Romeo (2 hours).

   - Multimedia: computer-projector show using the Matlab Wavelet Toolbox, running on a high-performance Linux machine; public computer lab.
   - References: Bowman & Newell (1998), Fang & Thews (1998), Goedecker (1998) and van den Berg (1999).

4. 'Small-Scale Structure and Dynamics in the Interstellar Medium' – John Black (2 hours).

5. 'Wavelets at Work in Astrophysics' – Alessandro Romeo (2 hours).

   - Photographs: `http://www.mvd.chalmers.se/~pergus/alessandro/` .
   - Multimedia: computer-projector show using the Matlab Wavelet Toolbox, running on a high-performance Linux machine, and the documentation of the MR/1-MR/2 Software Packages; public computer lab.
   - References: Fang & Thews (1998), Starck et al. (1998) and van den Berg (1999).

6. 'Magnetic Fields in Galaxies' – Cathy Horellou (2 hours).

7. 'Dynamical Modelling of Disc Galaxies: Multi-Scale Structures' – Alessandro Romeo (2 hours).

   - References: Romeo (1994), Friedli (1996), Zhang (1996), Masset & Tagger (1997), Romeo (1997, 1998a, b), Zhang (1998), Block & Puerari (1999), Combes (1999a), Erwin & Sparke (1999), Friedli (1999), Martini & Pogge (1999), Shlosman (1999), Zhang (1999), Combes (2000), Englmaier & Shlosman (2000), Maciejewski & Sparke (2000) and Shlosman (2000).

3 The Workshop

1. 'Turbulence and Fractal Analysis Using Wavelets' – Michael Försth (1.5 hours).

   - Proceedings: review paper.
   - Referees: Jöran Bergh, Cathy Horellou and Alessandro Romeo.

2. 'Dark Matter and Cold Fractal Clouds' – Achim Tappe (1.5 hours).

   - Proceedings: review paper.
   - Referees: John Black, Alessandro Romeo and Tommy Wiklind.

3. 'Fractals and Large-Scale Structure of the Universe' – Ğirts Barinovs (1.5 hours).

   - Proceedings: paper.
   - Referees: Alessandro Romeo and Tommy Wiklind.

4. 'Magnetohydrodynamic Turbulence in Accretion Discs' – Rim Turkmani (1.5 hours).

- Proceedings: review paper.
- Referees: Arto Heikkilä, Alessandro Romeo and Ulf Torkelsson.

5. 'Galaxy Collisions' – Nils Tarras-Wahlberg (1.5 hours).
   - Proceedings: abstract.
   - Referees: Alessandro Romeo.
6. 'The Outflow-Disc Interaction in Young Stellar Objects' – Michele Pestalozzi (1.5 hours).
   - Proceedings: review paper.
   - Referees: John Conway, Michael Olberg and Alessandro Romeo.
7. 'Jets from Herbig-Haro Objects' – Jiyune Yi (1.5 hours).
   - Proceedings: abstract.
   - Referees: Alessandro Romeo.
8. 'Origin and Propagation of Extragalactic Jets' – Alessandro Laudati (1.5 hours).
   - Proceedings: abstract.
   - Referees: Alessandro Romeo.
9. 'Why Are Evolved-Stellar Atmospheres Clumped?' – Liz Humphreys (cancelled).
10. 'Ionization Fronts and Photo-Dissociation' – Henrik Olofsson (1.5 hours).
    - Proceedings: review paper.
    - Referees: John Black, Åke Hjalmarson and Alessandro Romeo.

Acknowledgements

I would very much like to thank the following people for their invaluable help: the speakers of the parallel seminars on hot topics, the contributors to the workshop and the referees of the proceedings; Christer Andersson (guided visits), Per Gustafson (IT-project), Bert Hansson (transports), Håkan Håkansson (AV-service), Biörn Nilsson and Michael Olberg (computers), Michele Pestalozzi and Achim Tappe (support from A to Z!). Last but not least, I acknowledge the financial support of the Swedish Natural Science Research Council, of the local institutions and the further generous grants by the 'Solveig och Karl G Eliassons Minnesfond'.

References

Bergh J., Ekstedt F., Lindberg M., 1999, Wavelets. Studentlitteratur, Lund

Binney J., Merrifield M., 1998, Galactic Astronomy. Princeton University Press, Princeton

Binney J., Tremaine S., 1987, Galactic Dynamics. Princeton University Press, Princeton (Errata in arXiv:astro-ph/9304010)

Block D.L., Puerari I., 1999, A&A 342, 627

Bowman C., Newell A.C., 1998, Rev. Mod. Phys. 70, 289

Choudhuri A.R., 1998, The Physics of Fluids and Plasmas: An Introduction for Astrophysicists. Cambridge University Press, Cambridge

Combes F., 1999a, ASP Conf. Ser. 187, 59

Combes F., 1999b, arXiv:astro-ph/9906477

Combes F., 2000, ASP Conf. Ser. 197, 15

Dyson J.E., Williams D.A., 1997, The Physics of the Interstellar Medium. Institute of Physics Publishing, Bristol

Englmaier P., Shlosman I., 2000, ApJ 528, 677

Erwin P., Sparke L.S., 1999, ApJ 521, L37

Fang L.-Z., Thews R.L. (Eds.), 1998, Wavelets in Physics. World Scientific, Singapore

Friedli D., 1996, ASP Conf. Ser. 91, 378

Friedli D., 1999, ASP Conf. Ser. 187, 88

Goedecker S., 1998, Wavelets and Their Application for the Solution of Partial Differential Equations in Physics. Presses Polytechniques et Universitaires Romandes, Lausanne

Hubbard B.B., 1998, The World According to Wavelets: The Story of a Mathematical Technique in the Making. Peters, Wellesley

Maciejewski W., Sparke L.S., 2000, MNRAS 313, 745

Mallat S., 1998, A Wavelet Tour of Signal Processing. Academic Press, San Diego

Martini P., Pogge R.W., 1999, AJ 118, 2646

Masset F., Tagger M., 1997, A&A 322, 442

Matlab Wavelet Toolbox: `http://www.mathworks.com/products/wavelet/`

Misiti M., Misiti Y., Oppenheim G., Poggi J.-M., 1997, Wavelet Toolbox for Use with Matlab: User's Guide. The MathWorks, Natick

MR/1-MR/2 Software Packages: `http://www.multiresolution.com/`

Padmanabhan T., 1996, Cosmology and Astrophysics through Problems. Cambridge University Press, Cambridge

Pfenniger D., 1998, Mem. S.A.It. 69, 429

Press W.H., Teukolsky S.A., Vetterling W.T., Flannery B.P., 1992, Numerical Recipes in Fortran: The Art of Scientific Computing. Cambridge University Press, Cambridge

Romeo A.B., 1994, A&A 286, 799

Romeo A.B., 1997, A&A 324, 523

Romeo A.B., 1998a, A&A 335, 922

Romeo A.B., 1998b, *N*-Body Simulations of Disc Galaxies Can Shed Light on the Dark-Matter Problem. In: Salucci P. (ed.) Dark Matter. Studio Editoriale Fiorentino, Firenze, p. 177

Romeo A.B., 1999a, arXiv:physics/9906028

Romeo A.B., 1999b, Astrophysical Dynamics. Course Notes, Onsala Space Observatory (unpublished)

Shlosman I., 1999, ASP Conf. Ser. 187, 100

Shlosman I., 2000, ASP Conf. Ser. 197, 23

Shore S.N., 1992, An Introduction to Astrophysical Hydrodynamics. Academic Press, San Diego

Shu F.H., 1992, The Physics of Astrophysics – Vol. II: Gas Dynamics. University Science Books, Sausalito

Starck J.-L., Murtagh F., Bijaoui A., 1998, Image Processing and Data Analysis: The Multiscale Approach. Cambridge University Press, Cambridge

van den Berg J.C. (Ed.), 1999, Wavelets in Physics. Cambridge University Press, Cambridge

van Dyke M., 1982, An Album of Fluid Motion. Parabolic Press, Stanford

Vetterling W.T., Teukolsky S.A., Press W.H., Flannery B.P., 1992, Numerical Recipes Example Book (Fortran). Cambridge University Press, Cambridge

Wavelet Digest: `http://www.wavelet.org/`

Zhang X., 1996, ApJ 457, 125

Zhang X., 1998, ApJ 499, 93

Zhang X., 1999, ApJ 518, 613

Turbulence and Fractal Analysis Using Wavelets

Michael Försth

Department of Experimental Physics
Chalmers University of Technology and Göteborg University
SE-41296 Göteborg, Sweden
(forsth@fy.chalmers.se)

*

Abstract

We review two methods for analysing experimental velocity data in turbulence, and the wavelet techniques on which they are based. The first method (Li 1998; Li et al. 1999) uses wavelet autocorrelations to study the hierarchical organization of spatial structures, eddies, in a jet flow. The second method (Arneodo et al. 1999) describes how the rapid fluctuations in the turbulent velocity can be characterized in terms of fractal dimensions. In the latter method, much of the toolbox is borrowed from statistical thermodynamics.

1 Introduction

One of the first scientific approaches to turbulence was made in 1894 when Reynolds proposed to separate the velocity field into a mean field $\mathbf{u}$ and a fluctuating field $\mathbf{u}'$. Since then, progress has been made but many unsolved problems remain. Indeed, some researchers even claim that the theory of fully developed turbulence is in what may be called a pre-scientific phase (Farge et al. 1999).

The equations describing fluid motion are the *Navier-Stokes* equations:

$$\frac{\partial \mathbf{u}}{\partial t} + \overbrace{(\mathbf{u}\cdot\nabla)\mathbf{u}}^{advection} + \frac{1}{\rho}\nabla p = \overbrace{\nu\Delta\mathbf{u}}^{dissipation} + \mathbf{F}, \tag{1}$$

$$\nabla\cdot\mathbf{u} = 0, \tag{2}$$

where $\mathbf{u}$ is the velocity field, ρ is the density, ν is the kinematic viscosity, and $\mathbf{F}$ is the external force acting on the fluid. A well defined fluid-dynamic problem also includes initial and boundary conditions. Turbulence occurs when the advection term $(\mathbf{u}\cdot\nabla)\mathbf{u}$, which is non linear in the velocity, becomes much greater than the dissipation term $\nu\Delta\mathbf{u}$, which transforms kinetic energy into heat. A rough estimate of the ratio between advection and dissipation is:

$$\frac{\text{advection (non linear)}}{\text{dissipation (linear)}} \sim \frac{UL}{\nu} = R_e, \tag{3}$$

*Astrophysical Dynamics 1999/2000, Alessandro B. Romeo (Ed.), Onsala Space Observatory, 2000.

where U is a characteristic speed, and L is a characteristic dimension (typically a pipe-diameter). This ratio, R_e, is called the *Reynolds number* and is an important parameter in fluid dynamics. The transition from laminar to turbulent flow occurs when R_e becomes greater than $\sim 10^3$. The inertial forces, described by the advection term, become much larger than the viscous dissipation forces. Since dissipation is the damping factor via heat production this means that damping becomes too small for the system to remain stable: a stable laminar flow is transformed into an unstable turbulent flow. Some typical values of the Reynolds number are given below:

$10^2 - 10^6$ in hydraulics and naval engineering,
$10^6 - 10^8$ in aeronautics,
$10^8 - 10^{12}$ in meteorology and oceanography,
$> 10^{12}$ in astrophysics.

Better understanding of turbulence is of special importance to astrophysics. The reason why flow in outer space is so turbulent is that L in Eq. 3 is very large.

A central concept in turbulence theory is the *scale*, and more specifically how energy is transferred between scales. In 1941 the Soviet scientist Kolmogorov proposed that the energy is distributed according to the power law:

$$E(k) = K\epsilon^{2/3}k^{-5/3}, \tag{4}$$

where K is Kolmogorov's constant, ϵ is the rate of energy transfer, and k is the wavenumber $2\pi/\lambda$. This law should only be valid in the so called *inertial range*, of intermediate k. The general theory is that energy is injected at the large-scale end of the spectrum (i.e., at small k), while energy leaves the fluid motion via dissipation into heat at small scales (i.e., at high k). Today this theory is not taken as a general truth but rather as a crude approximation. One deviation from the statistical description given in Eq. (4) are the *coherent structures*, which can exist even for very large Reynolds numbers. Coherent structures are spatial structures that exist for relatively long times, which make the statistical treatment of turbulent data insufficient (Farge et al. 1999).

In this paper, we review two methods for analysing experimental velocity data in turbulence. Both methods are based on wavelet techniques, which are described in a friendly way (Lewalle 1995). The first method (Li 1998; Li et al. 1999) uses wavelet autocorrelations to study the hierarchical organization of spatial structures, eddies, in a jet flow. The second method (Arneodo et al. 1999) describes how the rapid fluctuations in the turbulent velocity can be characterised in terms of fractal dimensions. In the latter method, much of the toolbox is borrowed from statistical thermodynamics.

This paper does not discuss turbulence modelling, which is another area where wavelets have shown to be a valuable tool (Farge 1999).

2 Fundamentals of Wavelet Analysis

Wavelet analysis is a fairly new discipline in mathematics, born in the early 80s. It was originally conceived for the analysis of seismic data and acoustic signals (Arneodo et al. 1999). The short and gentle introduction to wavelets given here is mainly inspired from (Lewalle 1995), and all figures in Sect. 2 are taken from this source.

2.1 Basic Definitions

We start with a Mexican hat function, see Fig. 1. This is an example of what a wavelet is: an oscillation which is localised in time, here around t=0, and whose average is zero.

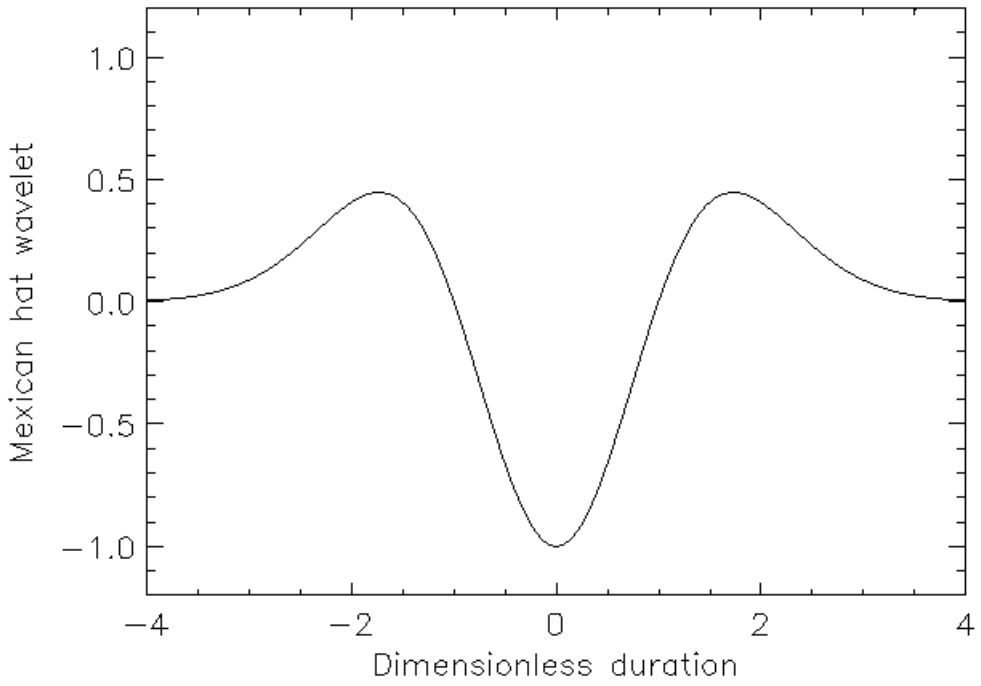

Figure 1: The Mexican hat wavelet. From Lewalle (1995).

This wavelet is used in wavelet analysis in the same way that sine and cosine functions are used in Fourier analysis. Assume that we have a periodic signal, such as $f(t) = 2cos(\pi t) + 7cos(2\pi t)$, then a very efficient way to analyse this function is to use Fourier analysis:

$$Ff(\omega) = \int_{-\infty}^{\infty} f(t) \exp(i\omega t) dt \tag{5}$$

Or, inserting f(t):

$$Ff(\omega) = \int_{-\infty}^{\infty} (2\cos(\pi t) + 7cos(2\pi t))(\cos(\omega t) + i\sin(\omega t)) dt \tag{6}$$

Because of the orthogonality between sine and cosine functions, and between cosine functions of different frequencies, we will only get a non-vanishing value of the integral for $\omega = \pi$ and $\omega = 2\pi$. For these frequencies the Fourier transform $Ff(\omega)$ will be infinitely high, the "Dirac peak", with the weights 2 and 7, respectively.

If instead of $\exp(i\omega t)$ we use the wavelet in Fig. 1 to probe our function, we will not get such a precise result about which frequencies our function contains. On the other hand, we will keep some information regarding how the function behaves in time. This latter information is entirely lost in the Fourier transform. Figure 2 shows the wavelet transform of a cosine function, using the Mexican hat wavelet. The cosine function, which is to be analyzed, is shown with a solid line at the top of the Figure. The dotted lines show the Mexican hat wavelet. Going from top and descending, the wavelet is squeezed more and more. The dashed lines show the result of the scalar product, or the integral of the product, of the wavelet and the function at the top of the figure. We notice that the wavelet that has been "medium squeezed", in the middle, manages to follow the analyzed function pretty well. Thus by looking at the wavelet transform we can follow how the analyzed function behaves in time. This might not seem that impressive since if we were only interested in the temporal behaviour of the function the best would be to look directly

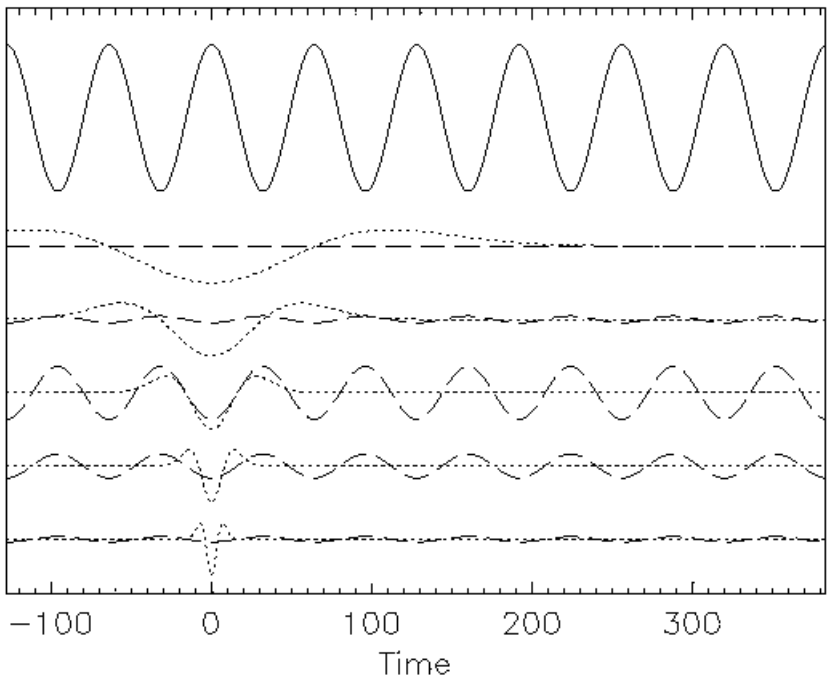

Figure 2: The upper solid line is the signal to be analyzed. The dotted lines are the Mexican hat wavelet that has been squeezed and stretched to different degrees. The dashed lines show the wavelet transform. From Lewalle (1995).

at the function itself. However, we have got more information. The Mexican hat wavelet yields almost a vanishing result in the wavelet transform when it is elongated, as in the upper part of Fig. 2, or when it is very squeezed, as in the lower part of Fig. 2. It is only the wavelet in the middle, with the medium period, which gives a significant result of the wavelet transform. This means that we have also got information about the frequency of the studied function, or its characteristic scale.

It is now time to formally define the wavelet transform. The wavelet transform maps a one-dimensional function to a two-dimensional function:

$$f(t) \mapsto Wf(a,b) \tag{7}$$

where

$$Wf(a,b) = \int_{-\infty}^{\infty} \Psi_{ab}^{*}(t) f(t) dt, \tag{8}$$

where * means complex conjugate. Here $\Psi(t)$ is the wavelet. For example the Mexican hat wavelet in Fig. 1 is defined as:

$$\Psi(t) = (t^2 - 1)\exp(-\frac{t^2}{2}). \tag{9}$$

This is in fact nothing else than the second derivative of the Gaussian bell function. The subindex $_{ab}$, as in $\Psi_{ab}(t)$ in Eq. 8, means that the wavelet is parametrized. It is this parametrization that makes it possible to detect both scales, via a, and temporal position, via b:

$$\Psi_{ab}(t) = \frac{1}{a}\Psi(\frac{t-b}{a}) \tag{10}$$

What really set wavelet analysis apart from Fourier analysis are mainly two things:

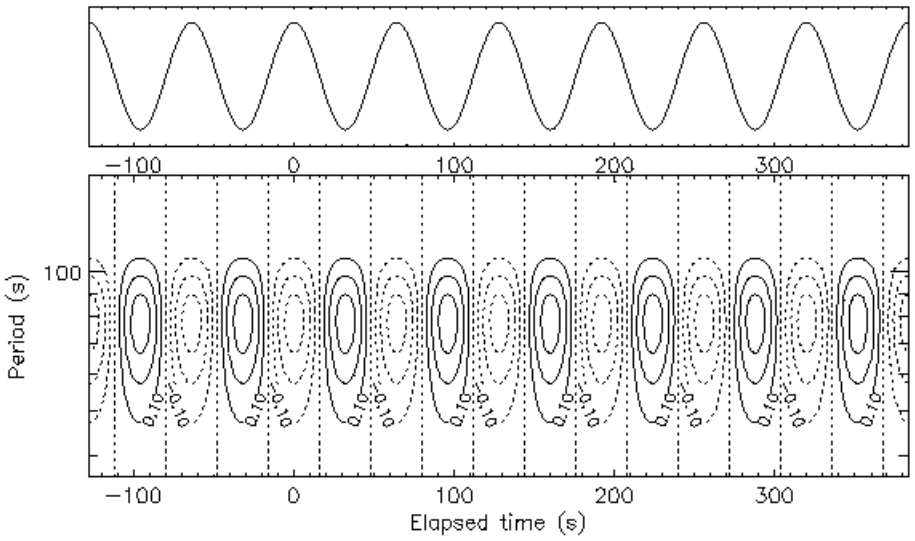

Figure 3: The two-dimensional Mexican hat wavelet transform shown as a contour map. The cosine curve at the top is the analyzed signal. From Lewalle (1995).

- The analyzing function, that is, the wavelet, can be almost any function. However, it must be zero on average, that is, $\int_{-\infty}^{\infty} \Psi(t)dt = 0$. Sometimes the wavelet is required not only to be orthogonal to a constant, which is in fact what was just stated, but rather orthogonal to polynomials up to order n. This is formulated as

$$\int_{-\infty}^{\infty} x^m \Psi(t)dt = 0, \qquad m = 0, 1, \ldots, n. \tag{11}$$

  These requirements are however quite moderate as compared to Fourier analysis, where only cosine and sine functions are allowed!

- The parameter b has the property that it translates the wavelet. For different b's the wavelet probes different parts of the function to be analyzed. This is what makes it possible to keep information about both the temporal and the frequency behaviour of the analyzed function. The latter is probed with the scale parameter a, which has its correspondence in Fourier analysis as the wavenumber, or inverse wavelength.

It is time to study a wavelet transform. Since the wavelet transform is a two-dimensional function it is shown as a contour map, Fig. 3. On top of Fig. 3 we have the cosine function that we want to analyze. At the bottom the wavelet transform of the cosine function is shown. The wavelet that has been used in Eq. 8 is again the Mexican hat, Eq. 9. The x-axis of Fig. 3 corresponds to the translation parameter b, and the y-axis corresponds to the scale parameter a. It is clear that we get information about both temporal behaviour, along the x-axis, and the frequential, or scale, behaviour, along the y-axis. As can be noticed in Fig. 3 the Mexican hat wavelet is good at detecting maximas and minimas in a signal, while its ability to determine scale, or frequency, is less good.

2.2 Wavelet Analysis of Non-Periodic Functions

We have thus far only analysed a simple cosine function. This is a bad example since Fourier analysis is most suited to analyse infinitely periodic functions. Wavelet analysis is

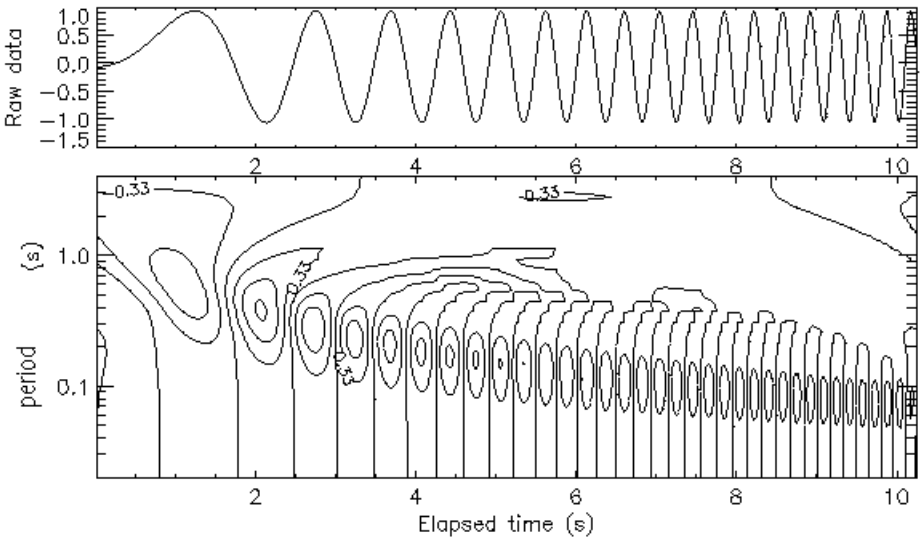

Figure 4: The top shows the analyzed signal which is $f(t) = \sin(t^2)$. The contour map of the wavelet tranform, using the Mexican hat wavelet, shows how the main scale decreases with time. From Lewalle (1995).

more powerful for non-periodic functions. In Fig. 4 the function $\sin(t^2)$ is shown, together with its wavelet transform. Here we see that the most important scale, or frequency, changes with time. This is something that is not at all revealed with Fourier analysis, where the correspondance to the x-axis in Fig. 4 does not exist. Thus, using the wavelet transform we can follow how the scale of the analyzed function changes with time.

An even more complicated signal is shown in Fig. 5. The function to be analyzed is a combination of signal with different frequencies, together with noise added at the beginning and at the end. From the wavelet transform we can see what the main frequencies are during the different intervals of the function. Furthermore, in each interval we can see when the function has its minimas (for clarity only the positive parts of the wavelet transform are shown in Fig. 5, if the negative parts were also plotted we could detect the maximas). Notice how the scale on the logarithmic y-axis goes to very small values at the beginning and the end of the function. This indicates that the added noise contains high frequency components.

As mentioned above one of the major differencies between wavelet analysis and Fourier analysis is that we are free to choose a wavelet that best suits our needs, we are not limited to the sine and cosine functions. We have seen that the Mexican hat wavelet is good at detecting maximas and minimas, but not so good at precise scale determinations. Another wavelet which is better at scale-determination and still has the ability to detect particular events in time is the *Morlet wavelet* which is shown in Fig. 6. The Morlet wavelet is "the wavelet of the wavelets", since it is a product of an event detecting factor, the Gaussian bell, and a frequency, or scale, detecting factor, the exponential $\exp(i\omega t)$

$$\Psi(t) = \underbrace{\exp(i\omega t)}_{\text{scale probe}} \cdot \underbrace{\exp(-\frac{t^2}{2})}_{\text{event probe}} \quad . \tag{12}$$

The Morlet wavelet is a complex function. In Fig. 6 the solid line shows the real part of

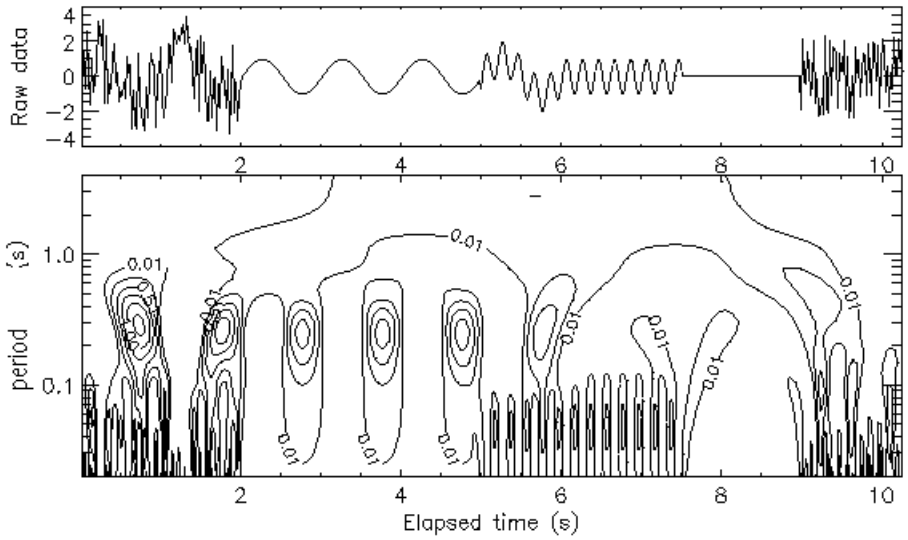

Figure 5: Wavelet transform of complicated raw data using the Mexican hat wavelet. The contour map does only show positive contours for clarity. From Lewalle (1995).

the Morlet wavelet while the dashed part shows the imaginary part[1].

Let us now use the Morlet wavelet, instead of the Mexican hat wavelet, to analyze the complicated signal in Fig. 5. The Morlet wavelet transform is shown in Fig. 7. The difference between Figs. 5 and 7 is striking. Figure 7 is much better to study if we are mainly interested in which scale, of frequency, components are characteristic for different parts of the signal. This is less obvious to see on Fig. 5 where the scale information has been smeared out along the y-axis. Instead, Fig. 5 gives us more information about particular events, such as maximas and minimas, as time goes by.

Summarizing this section we have seen that wavelet analysis is a powerful tool to study non-periodic signals. Because of our freedom in choosing a wavelet we can focus on different aspects of the analyzed signal, such as detection of particular events or on frequencies. These properties of wavelets are useful for the study of turbulence, as will be shown below.

3 Auto-Correlation Analysis of Turbulent Data

Our first application of wavelets in the analysis of turbulent data is taken from the work of Li et al. at Kagoshima University in Japan (Li 1998; Li et al. 1999). The work is focussed on planar gas jets. The aim is to analyze the velocity signal with auto-correlation methods, which are commonly used in turbulence studies.

[1]To be completely honest it should be said that Eq. 12 and Fig. 6 does not show the same thing. Equation 12 does not fulfil the requirement on a wavelet that it should be zero on average. In Fig. 6 a constant has been subtracted from Eq. 12, which is necessary in order for the mathematical analysis to work out.

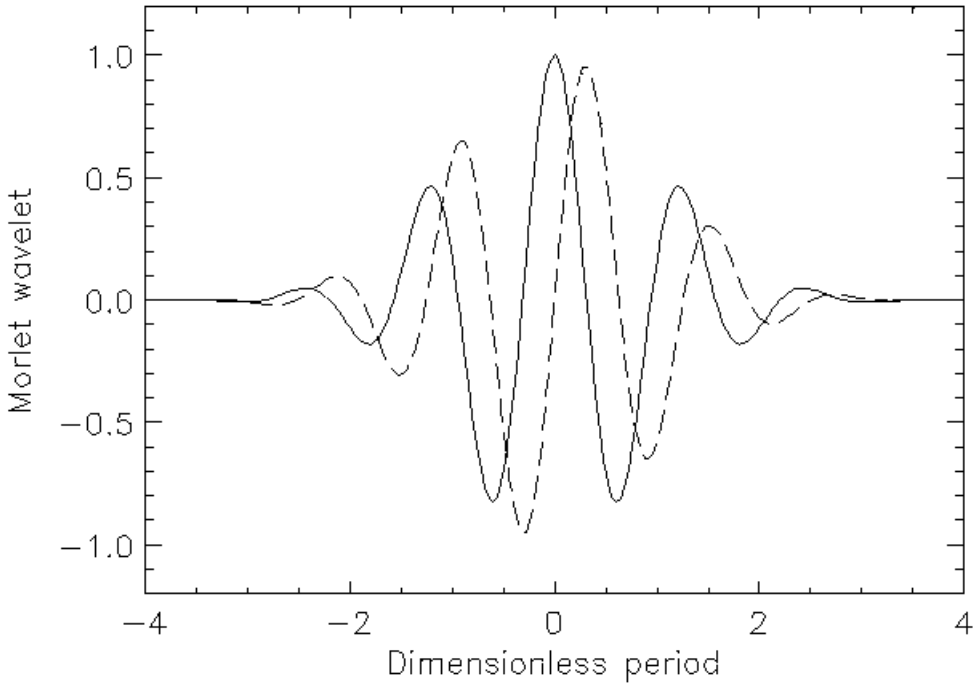

Figure 6: The Morlet wavelet. The solid line shows the real part, $\Re(\psi)$, while the dashed line shows the imaginary part, $\Im(\psi)$. From Lewalle (1995).

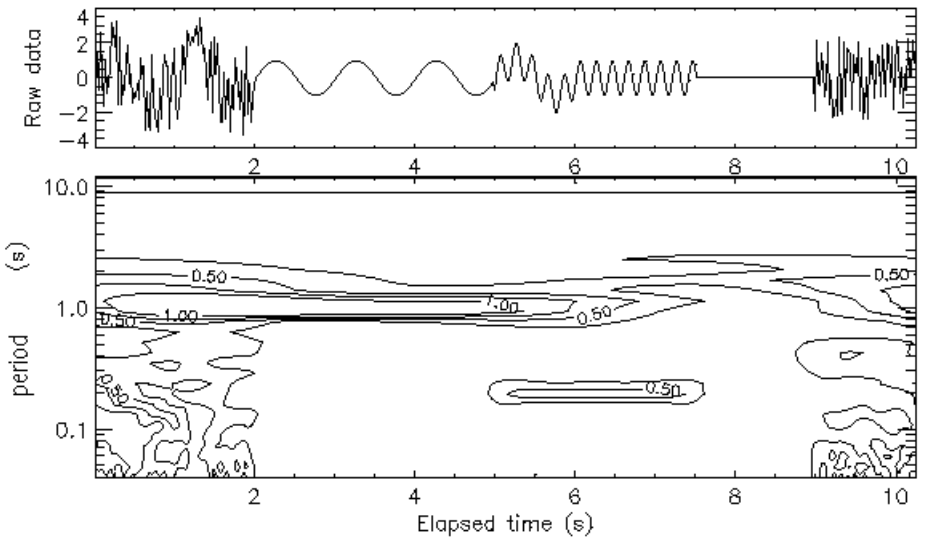

Figure 7: Wavelet transform of complicated raw data using the Morlet wavelet. The contour map does only show positive contours for clarity. Notice the different result obtained when the Mexican hat wavelet is used (Fig. 5). From Lewalle (1995).

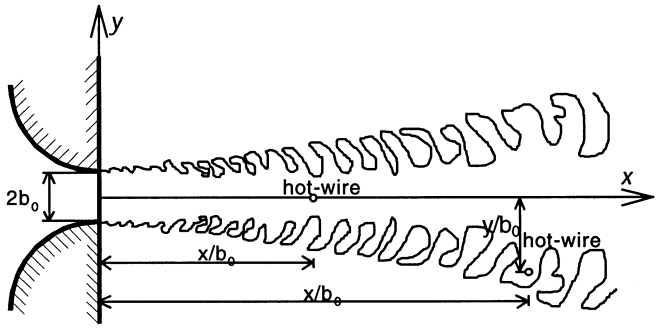

Figure 8: Schematic view of the experimental setup. The nozzle width is $d = 2b_0 = 25$ mm. From Li et al. (1999).

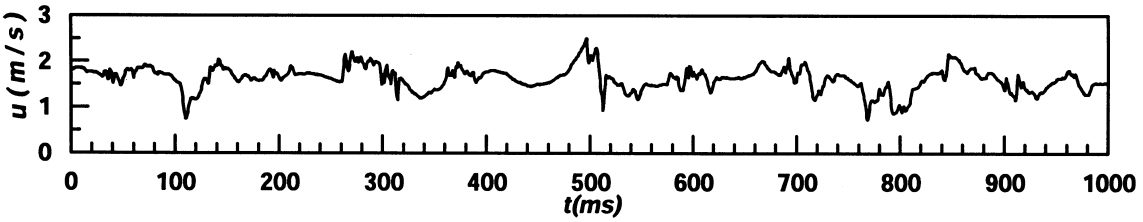

Figure 9: Example of a 1000 ms sample of the fluctuating speed in the x-direction, $u_x(t)$. The sample rate was 2 kHz. This particular data set was measured on the centerline a distance $x = 8.5d = 212.5$ mm away from the nozzle. From Li et al. (1999).

3.1 Experimental Setup

A schematic picture of the planar jet is shown in Fig. 8. The jet is created by a wind tunnel whose width is contracted by a factor 24. The wind tunnel blows out gas from a nozzle which is 300 mm high and 25 mm wide. The exit velocity was 2 m/s and the Reynolds number $R_e = 3330$, where the characteristic length scale is taken as $d = 25$ mm. The turbulent data that was measured was the gas jet speed in the x-direction, $u_x(t)$. This was measured with a standard hot wire anemometer technique with a sampling rate of 2 kHz. An example of the measurements is given in Fig. 9.

3.2 Wavelet Auto-Correlations

The traditional auto-correlation is calculated as:

$$C(\tau) = \lim_{T\to\infty} \frac{1}{T} \int_{-T/2}^{T/2} f(t) f(t+\tau) dt, \tag{13}$$

where $f(t)$ in this case is the speed in the x-direction. It is often normalized:

$$R(\tau) = \frac{C(\tau)}{C(0)}. \tag{14}$$

An example of the traditional auto-correlation is shown downmost in Fig 10. More information is obtained if instead of calculating the auto-correlation of the speed directly we calculate the auto-correlation of the wavelet transform of the speed:

$$WC(a,\tau) = \lim_{T\to\infty} \frac{1}{T} \int_{-T/2}^{T/2} Wf^*(a,b) Wf(a,b+\tau) db. \tag{15}$$

In Fig. 10a the Morlet wavelet has been used. This means that $WC(a,\tau)$ will be complex, which makes it difficult to illustrate the result. Therefore one defines $RWC(a,\tau)$, which is simply the real part of Eq. 15. It was shown in (Li 1998), for the case of this experiment, that the real part gives almost exactly the same information as the magnitude of the wavelet auto-correlation. In addition, the real part also contains information about the sign of the auto-correlation. The auto-correlation shown in Fig. 10a and b are what Li et al define as the *wavelet auto-correlation coefficient*:

$$RWR(a,\tau) = \frac{RWC(a,\tau)}{C(0)}. \tag{16}$$

The $RWR(a,\tau)$ is thus normalized with one denominator for all scales a. Another way is to normalize the auto-correlation locally for each scale, which gives us:

$$LRWR(a,\tau) = \frac{RWC(a,\tau)}{WC(a,0)}. \tag{17}$$

The last in our menagerie of different auto-correlations to be defined is the phase:

$$\theta WC(a,\tau) = \arctan(\frac{\Im(WC(a,\tau))}{\Re(WC(a,\tau))}), \tag{18}$$

which of course is the complement to $RWC(a,\tau)$ $WC(a,\tau)$ is to be described in polar coordinates in the complex plane. This last auto-correlation θWC will not be given any more attention. It was only included here since it is present in Fig.11. Time to move on to the results.

3.3 Results

It has been emphasized in section 2 that we are free in our choice of wavelet. This adds a part in the analysis process which does not exist in Fourier analysis: the choice of appropriate wavelet. Figure 10 shows the wavelet auto-correlation coefficient, as defined in Eq. 16, using two different wavelets: the Morlet wavelet, Fig. 10a, and the Mexican hat wavelet, Fig. 10b.

Figure 10c shows the traditional normalized auto-correlation. Both Figs. 10a and b show nearly periodic peaks which appear at $a = 70 - 90$ ms. Since the Morlet wavelet is better in measuring frequencies, two more nearly periodic peaks appear at $a = 50 - 70$ ms. These periodicities could not be detected with the Mexican hat wavelet in Fig. 10b. Therefore, the Morlet wavelet is used in the rest of this section because of its better scale probing performance.

Comparing the two-dimensional wavelet auto-correlation in Fig. 10a with the one-dimensional traditional ditto in Fig. 10c it can be seen that the large period peaks, $a = 70 - 90$ ms, in Fig. 10a correspond to the large period peaks in Fig. 10c. Moreover, the small period peaks, $a = 50 - 70$ ms, in Fig. 10a correspond to the small period peaks in Fig. 10c. We have thus gained information using wavelet methods as compared to traditional methods. Since, $R(\tau)$ gives us information about certain periodicities in the auto-correlation of the speed $u_x(t)$, but $RWR(a,\tau)$ also gives us information about the time scales on which these periodicities occur. The wavelet auto-correlation coefficient $RWR(a,\tau)$ can be interpreted as a frequency (time-scale) windowed auto-correlation.

Next figure to be analyzed is Figure 11. The difference between Fig. 11a and c is that $RWR(a,\tau)$ in Fig. 11a is normalized with one single denominator $C(0)$ for all scales a on

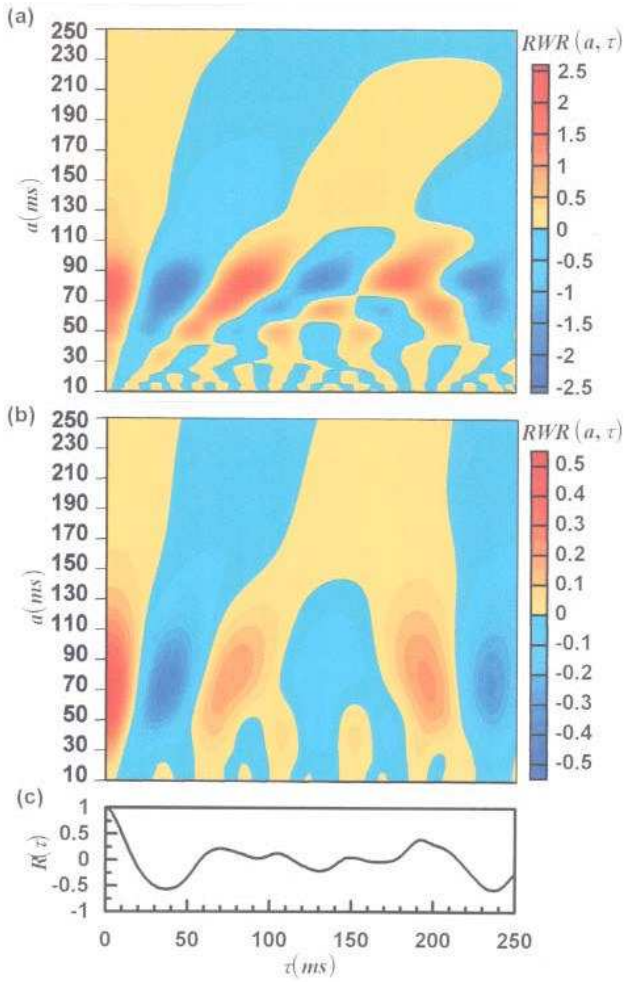

Figure 10: Measurement on centerline at $x = 4d = 100$ mm. a) Wavelet auto-correlation coefficients $RWR(a, \tau)$ using the Morlet wavelet. b) Ditto but using the Mexican hat wavelet. c) Traditional normalized auto-correlation $R(\tau)$. From Li (1998).

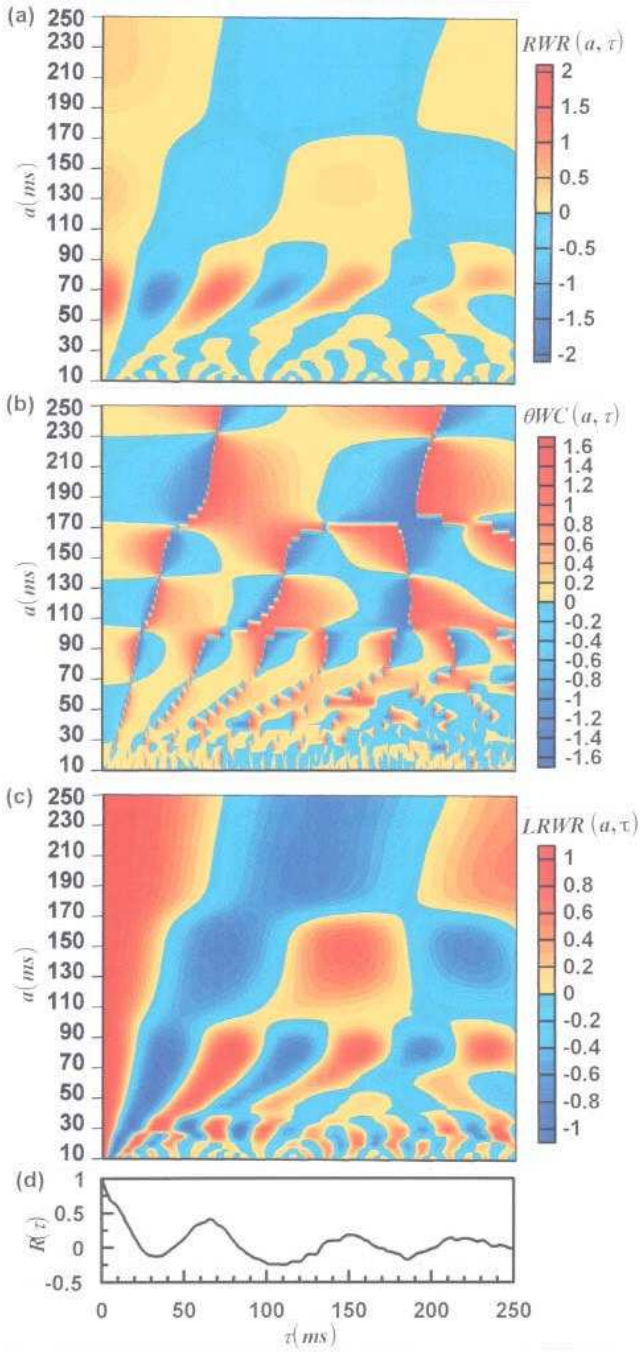

Figure 11: Measurement off the centerline at $y = d = 25$ mm, $x = 5d = 125$ mm. a) Wavelet auto-correlation $RWR(a, \tau)$. b) Phase of wavelet auto-correlation, $\theta RWR(a, \tau)$. c) Local wavelet auto-correlation, $LRWR(a, \tau)$. d) Traditional normalized auto-correlation $R(\tau)$. From Li (1998).

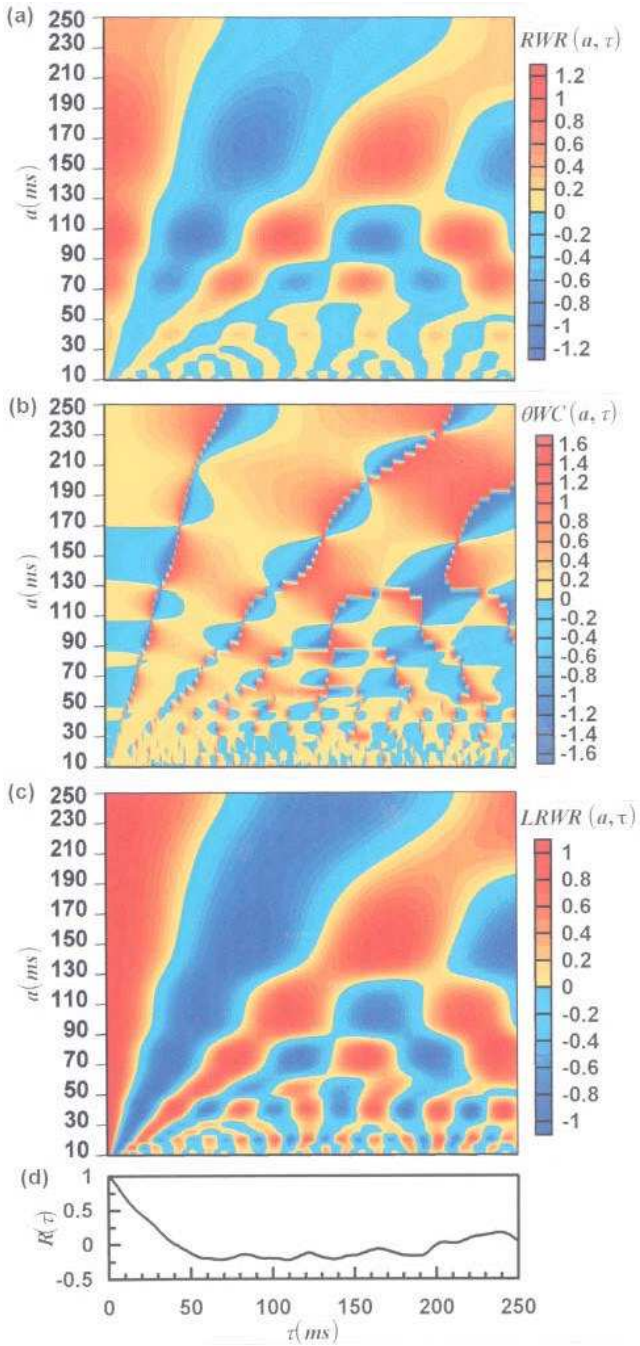

Figure 12: Measurement off the centerline at $y = 2.5d = 62.5$ mm, $x = 10d = 250$ mm. a) Wavelet auto-correlation $RWR(a, \tau)$. b) Phase of wavelet auto-correlation, $\theta RWR(a, \tau)$. c) Local wavelet auto-correlation, $LRWR(a, \tau)$. d) Traditional normalized auto-correlation $R(\tau)$. From Li (1998).

the y-axis, see Eq. 16. Whereas $LRWR(a,\tau)$ in Fig. 11c is normalized individually for each scale a, see Eq. 17. This gives a better visual resolution: the many different levels in $LRWR(a,\tau)$ for $a = 250$ ms in Fig. 11c cannot be seen in Fig. 11a for the same scale. A plot of $LRWR$ therefore appears to contain more information than a plot of RWR. On the other hand, $LRWR$ in Fig. 11c does not allow vertical comparisons, that is comparing $LRWR(a,\tau)$ with $LRWR(a',\tau)$, since they are normalized differently.

From a more fundamental point of view, we notice that the agreement between $LRWR(a \approx 75,\tau)$ and $R(\tau)$ is striking. But, again, Fig. 11c contains much more information since it contains data for different scales a. It should also be noticed how the general periodicity in the τ-direction, along the x-axis, decreases with decreasing scale a. This was also seen in Fig. 10.

Finally, in Fig. 12 we look at the result for $u_x(t)$ measurements for a point far away from the nozzle, $x = 10d = 250$ mm, and quite much off-axis, $y = 2.5d = 62.5$ mm. At this point the traditional $R(\tau)$ in Fig. 12d quickly decays with time, suggesting that there is little or no self-correlation in $u_x(t)$ for delays $\tau > 50$ ms. However, using the wavelet technique, as in Figs. 12a-c, we see that this is completely wrong. The speed contains several periodicities in its auto-correlation, but they are different for different time scales a of the speed fluctuations. This illustrates the remarkable strength of the wavelet technique. The traditional auto-correlation mixes different periodicities so the net result averages out to near zero, while the wavelet technique manages to resolve the different periodicities, and to assign time scales a for each of them.

Another striking feature of Fig. 12 is the branching that occurs for $\tau \approx 170$ ms. For $a \approx 150$ ms this is one single maximum. When the time scale is decreased to $a \approx 100$ ms the maximum is broken up in three bumps. Continuing to $a \approx 75$ ms these are broken up into 6 bumps, and so on. This indicates the existence of complex periodic large eddy structures, which contain smaller eddy structures, which in turn contain even smaller structures, and so on.

Summarizing section 3, we have seen that it is important to make preparatory tests to determine which wavelet is most appropriate for a particular problem.

We have seen that the wavelet auto-correlation coefficients allow to resolve different periodicities which are hidden when we use traditional methods, due to averaging.

Finally we have seen that using wavelets it is easy to show the hierarchic structure of turbulent data. There is a continuing branching of the wavelet auto-correlation as we go to smaller and smaller scales. This can be depicted by a little poem, *"Richardson's ditty"* [Shu 1992], which also leads us to the next section.

> Large eddies have small eddies,
> which feed on their vorticity.
> Small eddies have smaller eddies,
> and so on to viscosity.

4 Revealing the Fractal Nature of Turbulent Data

In the previous section we saw how wavelet autocorrelations could succesfully be used to characterize turbulent data. In this section we will see how the jerky behaviour of turbulent data can be characterized in a more global sense. Compare for example Figs. 15a and 16a. Figure 15a shows the velocity signal from a wind tunnel experiment at ONERA in Paris. Figure 16a shows something completely different: a realization of fractional Brownian motion. Still, comparing the two it is difficult to make a statement about

which figure describes which phenomenon. However, by studying the fractal nature of the data, with help from thermodynamical methods, and wavelets of course, we will see that the data can be characterized in an unambigous way. The material presented here is entirely based upon Arneodo et al. (1999).

4.1 The Singularity Spectrum

The cusps in the curves of Figs. 15a and 16a describe singularities of various degrees of seriousness, or strengths. The strength of a singularity can be defined by the *Hölder exponent*, $h(x_0)$. If there exists a polynomial P_n of degree $n < h$ such that

$$|f(x) - P_n(x - x_0)| \leq C|x - x_0|^h, \tag{19}$$

then the Hölder exponent is the supremum of all such $h(x_0)$. Therefore the Hölder exponent is a local measure of the singularity strength of a function $f(x)$. From Eq. 19 we see that the bigger the h, the more regular, or less singular, the function $f(x)$.

A function with Hölder exponent $h(x_0)$ can be expanded, around x_0, as:

$$f(x)_{x_0} = c_0 + c_1(x - x_0) + \ldots + c_n(x - x_0)^n + C|x - x_0|^{h(x_0)}. \tag{20}$$

Let us now calculate the wavelet transform of f, as expressed above. If our analyzing wavelet is orthogonal to polynomials of order less or equal to n, see Eq. 11, the result will be, according to Eqs. 8 and 10:

$$Wf(a, x_0) = \frac{1}{a}\int C|x - x_0|^{h(x_0)}\psi(\frac{x - x_0}{a})dx = C|a|^{h(x_0)}\int |x'|^{h(x_0)}\psi(x')dx'. \tag{21}$$

And therefore the wavelet transform of f scales as the scale a to the power of the Hölder exponent $h(x_0)$:

$$Wf(a, x_0) \sim |a|^{h(x_0)}. \tag{22}$$

The *singularity spectrum* $D(h)$, which is the ultimate goal of this section, is a characteristic of the function f, and is defined as the Hausdorff dimension $D(h)$ of the set of points x where the Hölder exponent is equal to h. The Hausdorff dimension is, roughly, the required dimension for the measuring-rod used to size a set of points, such as the set $\{x : h(x) = h\}$ in this case. This dimension needs not necessarily be an integer, for fractals the Hausdorff dimension D is not an integer.

It then seems rather straightforward to obtain the singularity spectrum $D(h)$. First calculate the Hölder exponent $h(x)$ for all points x by calculating the wavelet transform of $f(x)$ with smaller and smaller scales. Plotting the logarithm of $Wf(a, x)$ against the logarithm of the scale a in Eq. 22 we obtain the Hölder exponent $h(x)$. The second and last step would be to calculate the Hausdorff dimension of all sets $\{x : h(x) = h\}$ for all different obtained h, and then we have the singularity spectrum $D(h)$. Unfortunately things are not that easy. The main problem lies in the fact that experimental data do not contain information at infinitely small scales a. If our data contain information down to a certain scale a_{min}, the wavelet transform $Wf(a \geq a_{min}, x_0)$ will not only involve the point x_0 for which we want the estimate the Hölder exponent, but due to the finite size of the probing wavelet the singular behaviour of nearby points will mix with the point x_0.

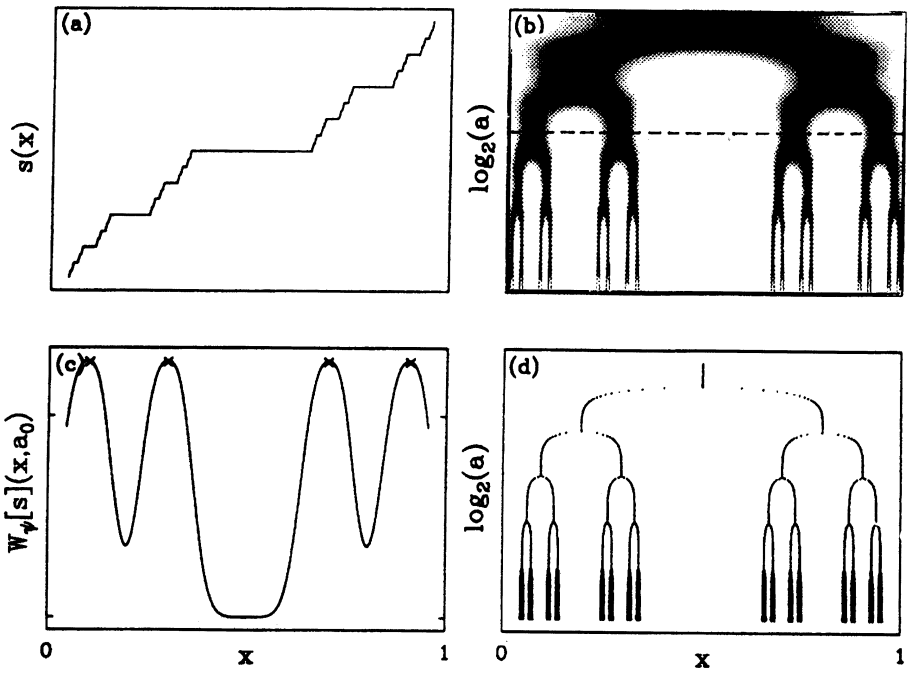

Figure 13: a) "Devil's staircase", which is an often used example of a fractal. b) The wavelet transform of the devil's staircase. The analysing wavelet is the first derivative of the Gaussian function. c) The profile of the wavelet transform for a given scale a, showed dashed in b. d) The maxima tree indicating the locations of the maxima of the wavelet transform in b. From Arneodo et al. (1999).

4.2 The Wavelet Transform Modulus Maxima (WTMM) Method

Instead of observing the dependence of the wavelet transform on the scale a for a local point x we make a global approach where we make use of a *partition function*. This partition function could be defined as:

$$Z(q,a) = \int |Wf(a,x)|^q dx \tag{23}$$

However, for negative moments q the partition function in Eq. 23 will diverge if $Wf(a,x) = 0$ for any (a,x). The idea of the WTMM method is to replace the integral over $|Wf(a,x)|^q$ to an analogous sum over maximas in $|Wf(a,x)|$: Let $\mathcal{X}(a_0)$ be the set of all x_i such that $|Wf(a,x_i)|$ is maximum with respect to x, at the scale a_0. In the example with the devil's staircase the content of the set $\mathcal{X}(a_0)$ for a given scale a_0 is the four crosses in Fig. 13c.

$$Z(q,a) = \sum_{x_i \in \mathcal{X}(a)} |Wf(a,x_i)|^q \tag{24}$$

The risk for divergences, that is, very small $|Wf(a,x_i)|$ in Eq. 24, can be further reduced be requiring that the wavelet transform should be evaluated not necessarily at the scale a but at any scale less or equal to a. Let $\mathcal{L}(a_0)$ be the set of all maxima lines that contain maxima at the scale a_0 and at all scales $a \leq a_0$. The latter requirement is the same thing as saying that the lines should be continous down to the limit $a \to 0^+$. The partition function is then defined as:

$$Z(q,a) = \sum_{l \in \mathcal{L}(a)} \left(\sup_{(x,a') \in l} |Wf(a',x)|^q \right) \tag{25}$$

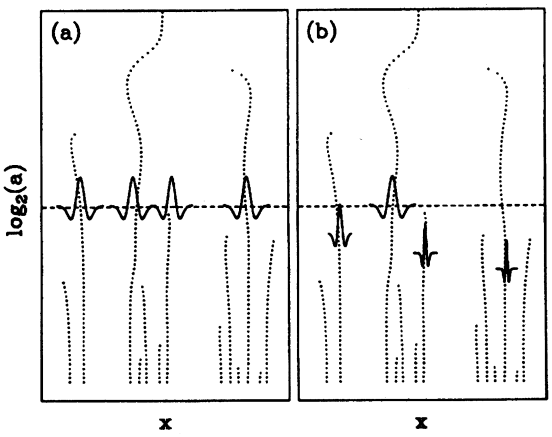

Figure 14: The difference between the definitions in Eqs. (24) and (25) for the partition function. In a) the summation is done at a constant scale a_0, while in b) the summation is done for the maximum value on the maxima line from a_0 to all smaller scales. From Arneodo et al. (1999).

The difference between the evaluation of the partition functions in Eqs. 24 and 25 is illustrated in Fig. 14.

We now define exponents, $\tau(q)$, from the scaling behaviour of the partition functions in the limit as $a \to 0^+$:

$$Z(q,a) \sim a^{\tau(q)} \tag{26}$$

The exponents $\tau(q)$ can be transformed into the singularity spectrum $D(h)$ via a *Legendre transformation*:

$$D(h) = \min_q(qh - \tau(q)). \tag{27}$$

But if $qh - \tau(q)$ is a minimum with respect to q then its derivative with respect to q should be zero. We therefore get the equation system:

$$D(h) = qh - \tau(q) \tag{28}$$

$$h = \frac{\partial \tau}{\partial q} \tag{29}$$

Now we have the tools necessary for calculating the singularity spectrum $D(h)$ for our experimental data with limited resolution. Figure 15b shows the wavelet transform of the turbulent velocity data in Fig. 15a. In Fig. 15c the tree of maxima lines has been extracted. (Notice that the scale a decreases upwards in the figures, the label on the y-axis should be $\log_2(1/a)$.) If we calculate the partition function in Eq. 25 using the data in Fig. 15c for smaller and smaller scales, we can obtain $\tau(q)$ from a plot of the logarithm of $Z(q,a)$ against the logarithm of a. The result is shown as filled circles in Fig. 17c. The corresponding $\tau(q)$ for the fractional Brownian motion in Fig. 16a is shown as filled triangles. From Fig. 17c we get the Hölder exponent h from Eq. 29, and for each h we get its dimension from Eq. 28. And, *voilà*, the singularity spectrum $D(h)$ for the turbulent velocity data in Fig. 15a is plotted in Fig. 17d. Notice that for the fractional Brownian motion $\tau(q)$ is linear in q with $\tau(q) = q/3 - 1$, which means that it only has one single Hölder exponent, $h = 1/3$. This gives that the entire singularity spectrum for the fractional Brownian motion reduces to a single point $D(h = 0.33) = 1$. This is in sharp contrast to the spectrum of the turbulent data. It is clear that the singularity spectrum is

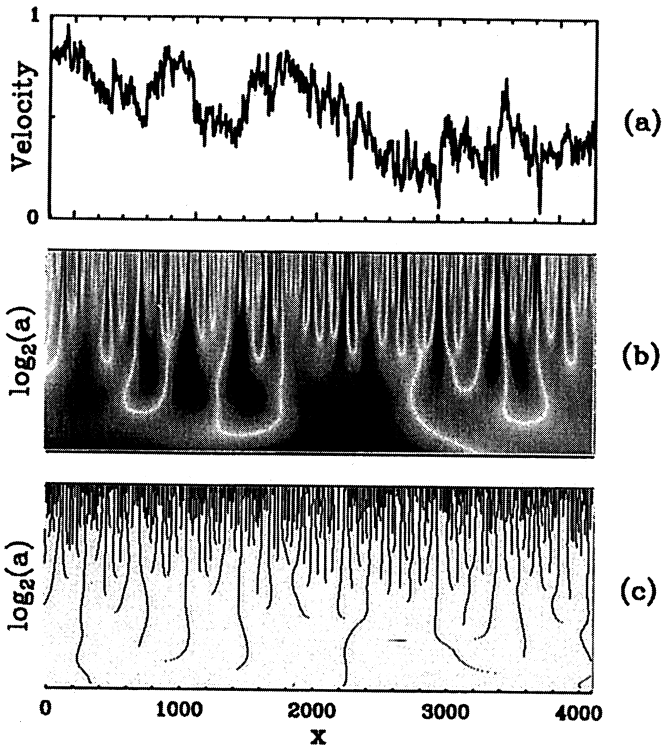

Figure 15: a) Turbulent velocity data. b) The wavelet transform of the turbulent velocity data, the analysing wavelet is the second derivative of the Gaussian function, that is, the Mexican hat wavelet [Eq. (9)]. c) The maxima tree indicating the locations of the maxima of the wavelet transform in b. *Note* that the scale a decreases upwards in the figures. The label on the y-axis should therefore be $\log_2(1/a)$. From Arneodo et al. (1999).

a powerful tool for characterizing and discriminating such jerky data as those in Figs. 15a and 16a.

It should be kept in mind, however, that this technique only works for isolated singularities. If the singularities are not isolated but dense, which means that they are located infinitely close to each other, the calculation of $\tau(q)$ from Eq. 26 will not be possible since the wavelet transform $|Wf(a,x)|$ in $Z(q,a)$ will always contain contributions from several singularities. Furthermore the sum would contain an infinite number of terms as $a \to 0^+$, which is an obvious numerical problem.

We summarize this section by pointing out the close relationship between much of the formulae used above with thermodynamics. In fact, q is the equivalence to the Boltzmann temperature $\beta = 1/(k_B T)$. This leads us to identify $|Wf(a', x_i)|$ with $\exp(-E_i)$, where E_i is the internal energy for microstate i. We then see that the partition function defined in Eqs. 23, 24, and 25 resemble the more well-known $Z = \sum_i \exp(-\beta E_i)$. Furthermore, the limit $a \to 0^+$ corresponds to the thermodynamic limit of infinite volume. Lastly, Legendre transforming $\tau(q)$ into the singularity spectrum $D(h)$ corresponds to Legendre transforming the free energy $F(\beta)$ into the entropy S. Fascinating!

5 Summary

Two examples of turbulent velocity data from two different experiments have been studied. We have shown that the use of wavelets helps us reveal information that may otherwise

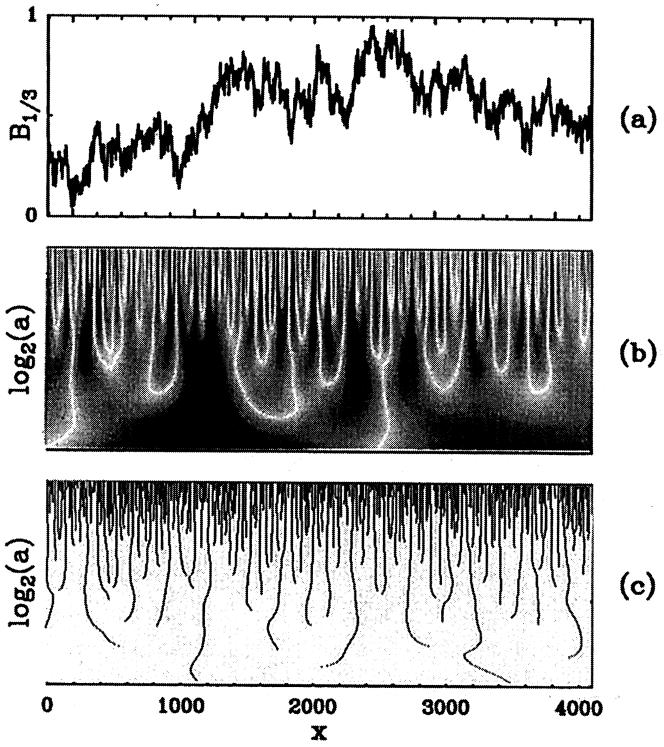

Figure 16: a) Fractional Brownian motion data. b) The wavelet transform of the fractional Brownian motion data, using the Mexican hat wavelet [Eq. (9)]. c) The maxima tree indicating the locations of the maxima of the wavelet transform in b. *Note* that the scale a decreases upwards in the figures. The label on the y-axis should therefore be $\log(1/a)$. From Arneodo et al. (1999).

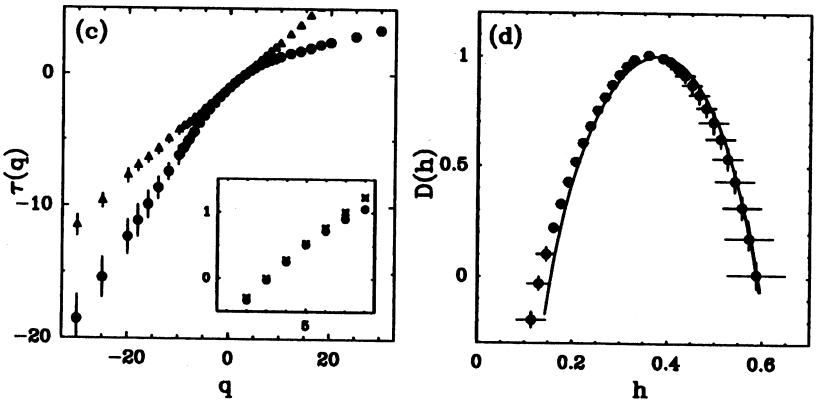

Figure 17: c) $\tau(q)$, the filled circles correspond to the turbulent velocity data in Fig. 15 while the filled triangles corresponds to the fractional Brownian motion data in Fig. 16. d) The singularity spectrum for the turbulent velocity data, obtained by Legendre transforming $\tau(q)$ in c. The singularity spectum for the fractional Brownian motion is not shown in d, since it consists of one single point $D(h = 0.33) = 1$. From Arneodo et al. (1999). (The original a) and b) have been omitted since they are not relevant to the material presented in this paper.)

be hidden.

More specifically, in the first example using wavelet autocorrelation functions, the wavelet technique displays periodicities at several different time scales. This is in contrast to the conventional autocorrelation technique where much information is lost since it only displays the average of the different time scales.

In the second example we have seen how wavelets together with a formalism borrowed from statistical thermodynamics permit us to unambigously characterize the behaviour of turbulent data via the singularity spectrum.

Acknowledgements

This paper is part of the examination for the course 'Astrophysical Dynamics 1999/2000' given by Alessandro Romeo. It is difficult to explain in written words the enthusiasm Alessandro shows for his students and for the science he is teaching, it must simply be seen and heard! I gratefully acknowledge Alessandro for his excellent course, as well for being a severe peer-reviewer of this paper. I also thank Onsala Space Observatory for hospitality.

In addition to Alessandro two more persons have generously accepted to peer-review this paper. These are Cathy Horellou at Onsala Space Observatory and Jöran Bergh at the Department of Mathematics. All these people work at Chalmers University of Technology.

I also gratefully acknowledge Prof. Hui Li, Prof. Jacques Lewalle, and Profs. A. Arneodo, E. Bacry, and J.F. Muzy for kindly permitting me to use their material in this paper.

References

Arneodo A., Bacry E., Muzy J. F., 1999, The Thermodynamics of Fractals Revisited with Wavelets. In: van den Berg J. C. (Ed.) Wavelets in Physics. Cambridge University Press, Cambridge

Farge M., Kevlahan N.K.-R., Perrier V., Schneider K., 1999, Turbulence Analysis, Modelling, and Computing Using Wavelets. In van den Berg J. C. (Ed.) Wavelets in Physics. Cambridge University Press, Cambridge

Lewalle J., 1995, Tutorial on Continous Wavelet Analysis of Experimental Data. http://www.mame.syr.edu/faculty/lewalle/tutor/tutor.html

Li H., 1998, Flow Structure Identification of a Turbulent Shear Flow with Use of Wavelet Statistics. In: CD-ROM Proceedings of the 8th International Symposium on Flow Visualization, No. 145, p. 1

Li H., Takei M., Ochi M., Saito Y., Horii K., 1999, Structure Evaluation of Unsteady Turbulent Flow with Continous and Discrete Wavelet Transforms. In: Proceedings of the 3rd ASME/JSME Joint Fluids Engineering Conference, p. 7167:1

Shu F. H., 1992, The Physics of Astrophysics—Volume II: Gas Dynamics. University Science Books, Sausalito

Dark Matter and Cold Fractal Clouds

Achim Tappe

Onsala Space Observatory
Chalmers University of Technology
SE-43992 Onsala, Sweden
(achim@oso.chalmers.se)

*

Abstract

There is strong evidence for a large fraction of dark matter in the Universe. Some of the evidence and candidates for dark matter are reviewed. Dark matter in spiral galaxies may be in the form of cold dense clouds of molecular hydrogen. This model is presented in more detail and perspectives for detecting the cold H_2 are discussed.

1 Introduction

The question of what makes up the mass density in the Universe is of great importance to astrophysics and cosmology. According to the widely accepted Big Bang model, the Universe originated from a very hot and dense state and has been expanding since then. Whether this expansion will ever stop, or even reverse, depends on the mass density (see Sect. 1.3 for more details). To determine this density it seemed at first expedient to look at the distribution of visible matter.

The current state of research is both exciting and embarrassing. We actually do not know what makes up 99 % of our Universe (cf. Sect. 1.3). Or in other words: 99 % of stuff constituting the Universe is apparently invisible to us (cf. Sect. 1.2), so that we are unable to observe it directly so far. Therefore we prefer to call this invisible matter "dark matter".

1.1 What Do We Mean by "Dark Matter"?

Let me start with some very fundamental thoughts on the role of experiment and observation in science (see Feynman 1998 for a more elaborate and delightful discussion on this). Science is basically a method of finding things out. This method is based on the principle that experiment or observation is the only judge of whether something is so or not. If one cannot answer a question by means of experiment or observation, it is not a scientific question according to this principle. Astronomy has a rather unique position among the

*Astrophysical Dynamics 1999/2000, Alessandro B. Romeo (Ed.), Onsala Space Observatory, 2000.

sciences, since essentially all information is obtained via observation at a distance, with no control over the experiment. One could simply say that astronomy is the study of light (photons) that reaches Earth from space.

Now, what is then a "dark" object in this sense? There are basically two possibilities. The first is that the object emits, absorbs or scatters so few photons that the photon flux, or in other words the intensity, is too low to be detected on earth. The second is that the object is not interacting with photons at all.

To go more into detail it is useful to introduce the Standard Model of particle physics. The following introduction is mainly based on an Internet article by Wagner (1999). The Standard model is our current theory of elementary particles and forces. Particles whose spins are half-integer multiples of Planck's constant $\hbar$ are called fermions (see Table 1). They make up all the matter that we see in the world around us.

Generation	Leptons		Quarks	
1	e	ν_e	d	u
2	μ	ν_μ	s	c
3	τ	ν_τ	b	t

Table 1: Particles (fermions)

Important points to note are:

- The fermions come in three generations. The particles in the first generation represent all the matter that we know about. The particles in generation 2 and 3 are almost identical to the corresponding particles in the first generation, except that they are more massive. They usually decay quickly into the lighter first generation particles.
- There are three charged massive leptons: the electron, the muon and the tau. Each has a neutral massless partner called a neutrino[1].
- A particle that consists of quarks (named "down", "up", "strange", "charm", "bottom" and "top") is called a hadron. A bound state of three quarks (e.g. the proton is a 'uud' state) is called a baryon.
- For each of the particles, there is a corresponding antiparticle. For example, the partner of the electron is the positron and the partner of the top quark is the top anti-quark. There are twelve particles and twelve antiparticles.

Particles whose spins are integer multiples of $\hbar$ are called bosons (see Table 2). They act as carriers of the forces by which particles of matter interact with one other.

Force	Particle
electromagnetic	γ (photon)
weak	$W^{\pm}$, Z^0
strong	g (gluon)
gravity	G (graviton)

Table 2: Carriers of forces (bosons)

[1]Recent experiments seem to confirm that the neutrino has in fact a small rest mass.

We note the following points:

- The electromagnetic force couples in general only to charged particles (that means: light is only absorbed, emitted or scattered by charged particles, e.g. neutrinos do not interact with light). However, note that the uncharged neutron has a small magnetic moment and therefore it does interact with light.

- The weak force couples to every particle, but in general its effect is only seen in the radioactive decay of particles.

- The strong force holds ("glues") the quarks together to form the hadrons.

- Gravity is not really part of the Standard Model. It is described by Einstein's general theory of relativity. So far, there is no unification of the Standard Model, which is based upon quantum mechanics and general relativity. This unification is one of the most fundamental aims of modern physics (Weinberg 1999).

Let us now come back to the original question: what does "dark matter" mean? We have learned the following:

- We use the term 'matter' basically for fermions (see Table 1).

- If we speak about 'baryonic matter', we mean the normal matter made up from protons and neutrons. The electrons are usually included although they are not baryons but leptons (see Table 1). Electrons are about 2000 times lighter than protons or neutrons and are therefore often not mentioned.

- In general, we cannot see uncharged particles, since they are not interacting with light. Neutrinos for example are invisible (note that invisible does not mean undetectable).

Thus dark matter could be either uncharged and therefore invisible particles or baryonic matter, whose interaction with light is too weak to be detectable on Earth.

1.2 Evidence for Dark Matter

How can we detect dark matter without actually seeing it? Well, we cannot see dark matter directly, but we can see its effect on other matter. Apart from the electromagnetic force, which acts only between charged particles, there is the gravitational force acting between all objects with nonzero mass. As a consequence one can infer something about the mass of an object by studying its gravitational interaction with another object. If there is no dark matter at all, such an investigation should give us the same value for the mass as the one inferred from observations of electromagnetic radiation.

In the following I will present two examples where this is not the case[2]. These two examples provide the most striking evidence for the presence of dark matter.

[2]Instructive computer simulations can be found in the dark matter tutorial by Dursi (1998).

1.2.1 The First Evidence: Clusters of Galaxies

A galaxy cluster is a group of a few to a few thousand galaxies, which are gravitationally bound together but otherwise isolated in space. The Milky Way, for example, is part of the so-called Local Group with 36 counted members in total (van den Bergh 2000). It is important to note that a galaxy cluster is not a static object. All the galaxies of the cluster have individual velocities, which can differ very much in value and direction from the average velocity. This velocity dispersion is normally of the order of a few hundred km/s.

In the thirties, Fritz Zwicky examined the velocities of galaxies in the Coma cluster and observed a large velocity distribution. Assuming that the cluster is stable, i.e. that the group is gravitationally bound and neither collapsing nor expanding on average, he was able to infer the total mass of the cluster. In other words, the individual velocities indicate the mass of the cluster. Galaxies with too high velocities would be able to break free of the gravitational pull of the cluster. By assuming that the cluster is in virial equilibrium, one can estimate the total mass (for more details see e.g. Binney & Tremaine 1987). The surprising result was that the visible matter was apparently not enough to explain the observed high velocity dispersion. Much more matter would be needed to keep the cluster together. This early result was later qualitatively confirmed by more accurate measurements. In fact, the gravitational mass of the Coma cluster derived from images taken by the X-ray satellite ROSAT suggest that the fraction of dark matter is about 60 % (Briel et al. 1992).

Another possibility for determining the gravitating mass of a galaxy cluster makes use of the effect of gravitational lensing. According to Einstein's general theory of relativity, space is curved due to the presence of mass or energy respectively. Light is affected by this curvature in the way that it travels on a bent path. Hence a massive object can act as a lens by means of its gravitational potential. In the case of galaxy clusters one can observe arches or arclets, which are "lensed" images of background galaxies. This is shown in the case of the galaxy cluster Abell 2218 by an impressive picture taken by the Hubble Space Telescope (see `http://oposite.stsci.edu/pubinfo/pr/2000/08/`).

The lensing effect depends on the mass of the lensing object and the spatial geometry of observer, lensing object and lensed object. So, by knowing the geometry one can infer something about the gravitating mass of the lensing object. This has been done in the case of Abell 2218 (Squires et al. 1996) and the detection of dark matter was reported.

1.2.2 The Second Evidence: Rotation Curves of Galaxies

For a long time it has been known that spiral galaxies spin around their center. From measuring the Doppler shifts of stars one is able to calculate their rotational velocity v. To obtain a rotation curve one plots this quantity versus the distance R of the star against the galactic center. According to Newtonian dynamics one would expect the rotation curve to fall off in proportion to $1/R^{1/2}$. Invariably, it is observed that the stellar rotational velocity remains more or less constant with increasing distance from the galactic center (e.g. Persic & Salucci 1995). These facts are shown schematically in Fig. 1. If one assumes the validity of Newtonian dynamics, the observed rotation curves suggest that galaxies contain significant amounts of dark matter. Another possible model is the so-called MOND-theory (MOdified Newtonian Dynamics; McGaugh 1999 and references therein).

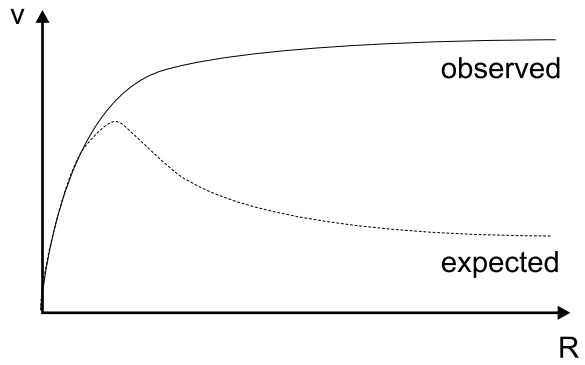

Figure 1: Expected and observed galactic rotation curves (schematic). The rotational velocity v is plotted versus the distance R from the galactic center.

1.3 How Much Dark Matter Is There in the Universe?

In the introduction I stated that we do not know what makes up 99 % of the Universe. However, some recent reviews on cosmology claim that, for the first time, we have a plausible and complete accounting of matter and energy in the Universe (Turner 1999, Turner & Tyson 1999). This is not a contradiction because we still do not have a complete understanding of all the ingredients.

In cosmology, mass or energy densities ϱ respectively are expressed in terms of the so-called critical density ϱ_{crit}, which is necessary to give the Universe an Euclidean (flat) geometry. The resulting dimensionless parameter is called Omega: $\Omega = \varrho/\varrho_{\mathrm{crit}}$. Several components contribute to the total density of the Universe Ω_{total}. In general, one distinguishes between:

Ω_{m} the density of matter (note that $\Omega_{\mathrm{m}} = \Omega_{\mathrm{CDM}} + \Omega_{\mathrm{b}}$)

Ω_{CDM} the density of (non-baryonic) cold dark matter (see Sect. 1.4)

Ω_{b} the total density of baryonic matter (visible and dark baryonic matter)

Ω_{vis} the density of visible baryonic matter

Ω_{Λ} the density of the vacuum energy (cosmological constant Λ)

Let me just briefly comment on the vacuum energy. Even a perfect vacuum has a nonzero energy according to quantum field theory. It is called zero point or vacuum energy and can be imagined as virtual particles coming in and out of existence. This mysterious energy behaves unusually in a way that it does not slow down but rather speeds up the expansion of the Universe.

The prospering model of inflationary cosmology demands $\Omega_{\mathrm{total}} = 1$ (cf. cosmology textbooks, e.g. Rowan-Robinson 1996 for an introduction or Coles & Lucchin 1995 for a more advanced treatment). The complete "inventory" of matter and energy totalling to $\Omega_{\mathrm{total}} = 1$ is shown in Fig. 2 (adapted from Lineweaver 1999). As already mentioned, we do not understand all the components shown in Fig. 2. What we understand rather well is the visible matter, which makes up only about 1 % of all the matter and energy in the Universe. However, intergalactic hydrogen gas, not previously visible, was recently traced with the Hubble Space Telescope (`http://oposite.stsci.edu/pubinfo/pr/2000/18/`, Tripp et al. 2000). This eventually increases the amount of visible matter to about 2 %.

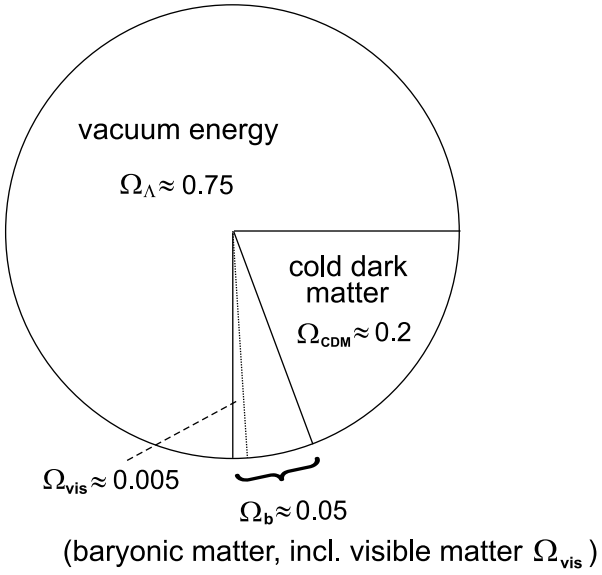

Figure 2: Matter and Energy in the Universe totalling to $\Omega_{\rm total} = 1$.

Note here that the theory of Big Bang Nucleosynthesis in combination with measurements of the light elements (Deuterium, Helium, Lithium) restricts the amount of baryonic matter in the Universe to $\Omega_{\rm b} \lesssim 0.05$. A significant amount of non-baryonic matter is needed to make $\Omega_{\rm total} = 1$ and to explain the structure formation in the early Universe.

What about the implications for the fate of the Universe? Let us at first consider a cold dark matter (CDM) model with a cosmological constant $\Lambda = 0$. If the overall mass density $\Omega_{\rm total} > 1$, the expansion will reverse in the future (closed Universe). For values of $\Omega_{\rm total} < 1$, the Universe will expand forever (open Universe). In the case of $\Omega_{\rm total} = 1$, the expansion of the Universe slows down gradually until it converges to zero at infinity (flat Universe). This scenario is shown in Fig. 3.

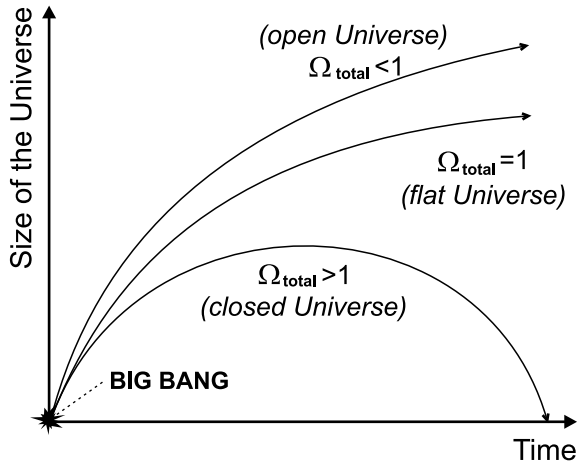

Figure 3: The parameter $\Omega_{\rm total}$ and the future of the Universe for $\Lambda = 0$.

With vacuum energy present (non-zero cosmological constant), the shape of the curves in Fig. 3 and likewise the fate of the Universe will change dramatically (see Lineweaver 1999). For example, with $\Omega_{\rm total} = 1$ and $\Omega_\Lambda \approx 0.75$ the expansion and the size of the

Universe will increase exponentially in the future. A recent analysis of distant supernovae seems to support this hypothesis (see Perlmutter et al. 1999).

However, the following questions remain (see Lineweaver 1999 and Turner 1999 for more details):

1. What is the nature of the vacuum energy?
2. What is the non-baryonic (cold) dark matter?
3. What is the baryonic dark matter?
4. Is Ω_{total} really equal to one?

Some advance has been made concerning the last question. A number of recent cosmic microwave background observations show convincing evidence for a flat Universe (e.g. BOOMERANG, Balloon Observations Of Millimetric Extragalactic Radiation ANd Geomagnetics, see `http://antwrp.gsfc.nasa.gov/apod/ap000509.html` and for first results de Bernardis et al. 2000; MAT, Microwave Anisotropy Telescope, see `http://imogen.princeton.edu/~page/matdir/www/`; Viper telescope, Peterson et al. 2000). A recent review on vacuum energy and the cosmic background radiation is given by Dodelson & Knox (2000).

In the following section I will present some of the possible candidates for the baryonic and non-baryonic dark matter.

1.4 Dark Matter Candidates

An overview of the proposed baryonic and non-baryonic dark matter candidates is given in Fig. 4.

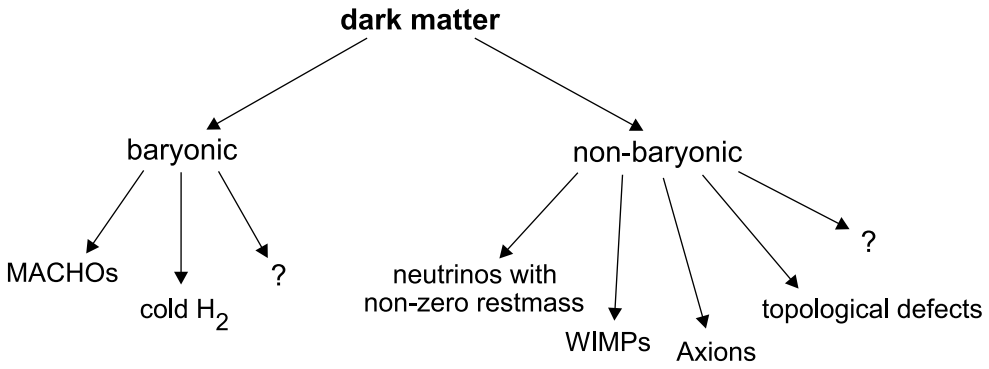

Figure 4: Candidates for baryonic and non-baryonic dark matter.

Let me briefly comment on these candidates (see Raffelt 1997 for more details). The term MACHO stands for MAssive Compact Halo Object. Galaxies are presumably enshrouded by a halo consisting mainly of dark matter. What is the nature of dark matter in these halos? It could be in the form of massive compact objects (e.g. brown or white dwarfs), which are too faint to be detected from Earth. But massive objects reveal themselves due to gravitational microlensing effects (see Sect. 1.2.1).

The search for MACHOs in the halo of the Milky Way was proposed emphatically in 1986 (see Paczynski 1986) and began finally in 1989 (EROS, Expérience de Recherche d'Objects Sombres, MACHO and OGLE, Optical Gravitational Lens Experiment, see Paczynski 1996). The first detection of a MACHO adorned the cover page of Nature in 1993 (Alcock et al. 1993). But there are probably not enough MACHOs in the halo to account for the observed rotation curve.

It has been proposed that dark matter in spiral galaxies may be cold molecular hydrogen distributed either in an extended disk (Pfenniger, Combes & Martinet 1994, hereafter PCM94, Pfenniger & Combes 1994), or in a spheroidal halo enshrouding the galaxy (de Paolis et al. 1995, Gerhard & Silk 1996, de Paolis et al. 1998). I will discuss the model of PCM94 in more detail in Sect. 2.

As for the non-baryonic dark matter, we address first the neutrinos. Having even a tiny mass, they could make up all of the non-baryonic dark matter. Low-mass neutrinos, however, are problematic dark matter candidates since they represent hot dark matter. The terms 'cold' and 'hot' dark matter refer to the early Universe. When the Universe became transparent to radiation (about 300 000 years after the big bang), matter was no longer in thermodynamic equilibrium with radiation. At that time, hot dark matter particles had relativistic speeds, whereas the speeds of cold dark matter particles were non-relativistic. This had important implications for the formation of structures in the early Universe. Hot dark matter basically cannot form small-scale structures such as galaxies in the first place, which is indicated by observations. So, the idea of low mass neutrinos accounting for most of the non-baryonic dark matter is ruled out.

What about other candidates? WIMPs (Weakly Interacting Massive particles) and axions are both non-baryonic cold dark matter candidates. As the name implies, WIMPs are massive particles which interact or couple only weakly with other matter. The most promising candidate is the neutralino, a particle predicted by an extension of the Standard Model called Supersymmetry (SUSY, see Wagner 1999). The existence of axions, which are very weakly interacting low-mass bosons, is a hot topic in theoretical physics. They were introduced to explain the CP (Charge Parity) problem of QCD (Quantum Chromodynamics; see Raffelt 1997 for a discussion of this problem). Topological defects of space include the so-called monopoles (point-like defects) and strings (line-shaped defects). They could have been formed during phase transitions in the early Universe.

It is important to note that all of the non-baryonic dark matter candidates, except the neutrinos, have not been observed yet. Their existence, and the validity of the theories predicting them, is still controversial. Laboratory searches and astronomical observations regarding these exotic particles and structures are among the most important scientific enterprises for understanding the Universe.

2 Molecular Hydrogen as a Dark Matter Candidate

Cold molecular hydrogen is a possible candidate for baryonic dark matter (see Sect. 1.4). PCM94 suggested that a large fraction of dark matter in spiral galaxies is cold molecular hydrogen. I will discuss the proposed model in the following section. In Sect. 2.2, I briefly comment on some perspectives for detecting cold molecular hydrogen.

2.1 The Cold Fractal Cloud Model

PCM94 proposed that dark matter in spiral galaxies may be in the form of cold fractal clouds in an extended disk. The smallest building blocks of these clouds are cold, dense clumps of molecular hydrogen gas, called "clumpuscules". According to the model of PCM94, the clumpuscules have a radius of the order of 30 AU, which is about the radius of the solar system, and a mass of approximately a Jupiter, that is $10^{-3}\,M_{\odot}$. The density is about 10^9 H atoms per cm^3.

By discussing some fundamental questions, I would like to emphasize some of the supporting as well as critical arguments concerning this model.

2.1.1 Why Is Molecular Hydrogen a Good Candidate for Dark Matter in Spiral Galaxies?

First of all, hydrogen is by far the most abundant element in the Universe. So, one might as well suspect that molecular hydrogen (H_2) is the most abundant molecule. It is a symmetric diatomic molecule and has no permanent dipole moment. Therefore electromagnetic dipole transitions are forbidden. H_2 has, however, a small permanent quadrupole moment. As a consequence, H_2 shows no strong rotational-vibrational (rovib) spectrum. What you can observe instead are weak rovib and pure rotational lines in the infrared, due to electromagnetic quadrupole transitions. These lines can only be seen when the molecular hydrogen is excited, e.g. caused by thermal collisions or absorption of UV starlight followed by fluorescence. Another possibility is to observe H_2 lines in absorption against IR sources, e.g. young stellar objects (YSOs). The resulting lines are usually weak, typically only a few percent of the continuum, which makes the observations very difficult. H_2 is well-studied in absorption against UV sources, usually O- or B-type stars. But the extinction and scattering of UV radiation by interstellar dust makes these observations either difficult or sometimes impossible, particularly in the case of dust-obscured or very distant regions.

To cut a long story short, there is probably a great deal of H_2 which we cannot see with current instruments, especially when it is cold, that means below 100K, and not exposed to UV radiation. It is therefore a good candidate for baryonic dark matter.

Another supporting argument for H_2 as a dark matter candidate is its consistency with the evolution of spiral galaxies along the Hubble Sequence (see Fig. 5). It was proposed that the evolution goes from late to early Hubble types (Pfenniger, Combes & Martinet 1996). During that process the fraction of dark matter seems to decrease but the amount of visible stars increases. The most straightforward explanation is that dark matter is at least partly consumed by star formation in the visible disk of spiral galaxies. Hydrogen would therefore be a reasonable candidate for dark matter in spiral galaxies.

2.1.2 Why Is the H_2 Cold?

No detailed model describing the thermal state of the dark H_2 clouds exists so far. This is mainly because the precise heating rates and mechanisms in the outer regions of galaxies are unknown. So, the thermal stability of cold clouds in an extended visible disk is not obvious. The heating by cosmic rays, for example, can probably be an important factor governing the temperatures in steady state with the cooling in the clouds (Walker & Wardle 1999, Sciama 2000).

However, one can try to set approximate upper limits to the temperature. High temperatures will eventually result in the evaporation of the denser clouds into the hot HI-gas component of the Galactic halo. This and observational constraints probably limit

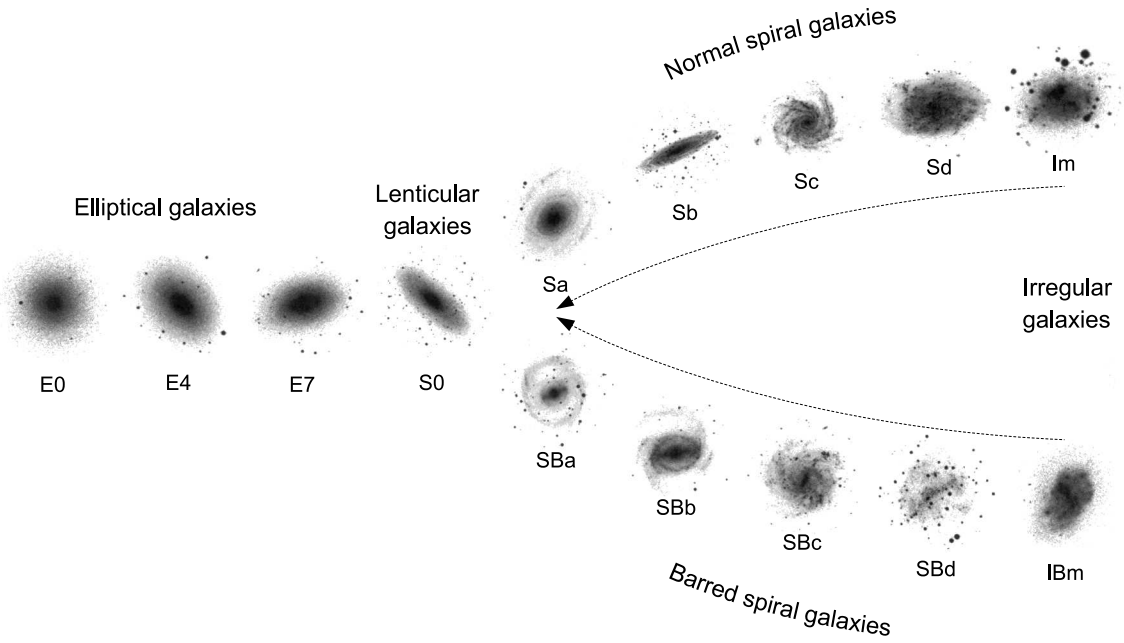

Figure 5: The Hubble Sequence of galaxies. The proposed evolution of spiral galaxies is indicated by the dashed arrows (Fig. adapted from Laustsen et al. 1987).

the temperatures of the dense H_2 clouds to values of about 10K or below. PCM94 suppose that they are in thermal equilibrium with the cosmic background radiation and hence have a temperature of around 3K.

2.1.3 What Determines the Size, Density and Distribution of the Clumpuscules?

If the clumpuscules are dense ($n_H \approx 10^9 cm^{-3}$) and have low temperatures ($T \lessapprox 10K$) then the critical question is why the gas clouds do not form stars. Presumably any such gas clouds have spent a long time, possibly several Gyr, in the extended disk. Why was there no star formation even at low efficiency?

Pfenniger and Combes propose that the clouds have a fractal structure with the clumpuscules representing the smallest building blocks (Pfenniger & Combes 1994). This is not implausible since the fractal nature of the interstellar cold gas is rather well known (Falgarone et al. 1992, Pfenniger 1996, Combes 1999). An analogy of such a fractal distribution is shown in Fig. 6.

A basic feature of every fractal structure is its self-similarity. Going to smaller and smaller scales one encounters the same structure again and again (see Fig. 6). In theory this behaviour would continue to infinitely small scales. In reality fractals show self-similarity only over a certain number of scales since there is a natural limit for the size of the building blocks. It is important to note that physical properties of fractal objects could be quite different from normal, smooth objects (e.g. objects with a roughly fractal surface have a much bigger effective surface area).

What about the implications of the fractal distribution? First of all, space would not be occupied homogeneously. Actually there are large regions of emptiness (again see Fig. 6) making the detection of such objects more difficult. But the clumpuscules themselves are in fact closer together, meaning that there are local regions with high concentration. That makes the collision timescale of the clumpuscules smaller than their collapse time. In

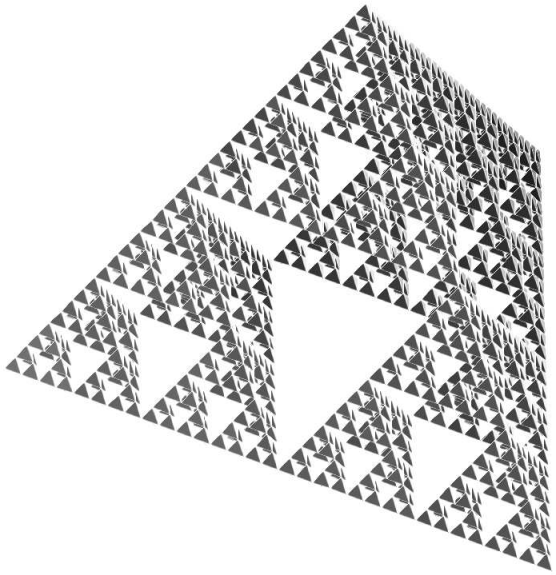

Figure 6: A fractal skewed web (Sierpinski tetrahedron, cf. Mandelbrot 1983)

other words, frequent collisions prevent the clumpuscules from gravitational collapse and hence from forming stars. The proposed size and density can be understood as a result of the dynamical equilibrium between collisions and gravitational collapse (see Pfenniger & Combes 1994 for a more detailed discussion).

2.2 Perspectives for Detecting Cold H_2 in the Galactic Disk and Halo

Many observational probes for detecting cold gas clouds of molecular hydrogen in an extended disk of our Galaxy have been suggested (e.g. Combes and Pfenniger 1997). The most promising are the study of quasar absorption lines, gravitational microlensing effects and extreme scattering events (ESE).

2.2.1 Quasar Absorption Lines

Absorption is a promising way to trace the cold H_2 gas (see Sect. 2.1.1). The absorption due to H_2 in the outer parts of our Galaxy could, in principle, be detected in the UV spectra of quasars. However, there are several difficulties.

First of all, H_2 absorbs in the UV at wavelengths around 1000 Å (Lyman and Werner bands). Ground based observations are impossible because of strong atmospheric absorption. Only the recently launched FUSE satellite (Far Ultraviolet Spectroscopic Explorer, see `http://fuse.pha.jhu.edu`) is currently able to perform measurements at these wavelengths from space.

Another complication is the line damping due to the proposed high column densities ($N_H \approx 10^{25}\,cm^{-2}$). The absorption lines would become extremely saturated and broadened (natural line widths far exceed the Doppler widths). As a consequence, all H_2 lines in the UV overlap, meaning that all the light with wavelengths $\lambda \lesssim 3000\,Å$ is absorbed (see Combes and Pfenniger 1997 for a simulated absorption profile). These absorptions

may appear and disappear on scales of one year, since the clumpuscules are supposed to have a proper motion of around 100 km s^{-1}.

The detection probability of such an absorption event is unclear. Due to the fractal distribution of the clumpuscules (see Sect. 2.1.3), the surface filling factor is less than 1 %. That would make absorption events very rare and the chance of detection with a satellite like FUSE would be very low.

2.2.2 Gravitational Microlensing

Another promising approach for detecting dark matter in our Galaxy makes use of gravitational microlensing effects. MACHOs have already been detected by that method (see Sect. 1.4). In addition the clumpuscules are able to act as gravitational microlenses (Draine 1998). The principle of gravitational lensing is shown in Fig. 7:

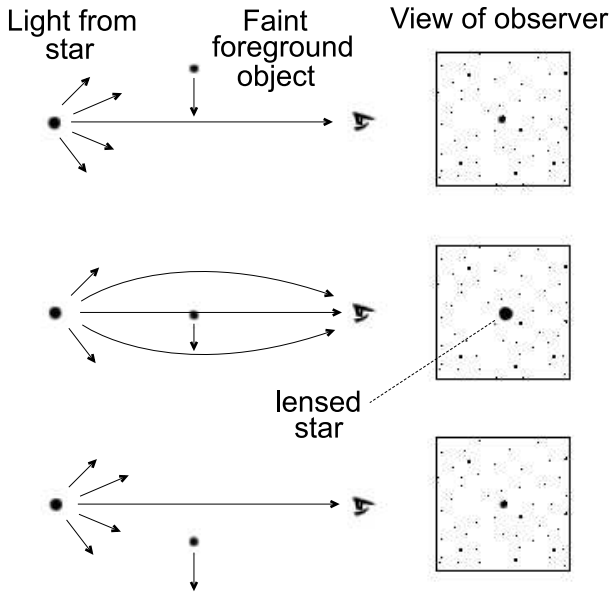

Figure 7: Gravitational lensing of a background star (schematic, adapted from Brau 1999).

The foreground object in Fig. 7 can be any massive object. The mass and proper motion of the object mainly determine the duration of the lensing event (Paczynski 1996). In fact, lensing events resulting from MACHOs and from clumpuscules would resemble each other. But there is a way to distinguish between MACHO and "gaseous lensing" events. If the lensing object consists of H_2 gas, absorption lines imposed on the stellar spectrum could be seen (Draine 1998). Supplementing any existing searches for gravitational microlensing events by spectroscopy would allow the detection of such gas clouds.

Another method for detecting dark matter is to study the distortion of background galaxy images caused by gravitational lensing. Large samples are needed to perform statistics and obtain information on the distribution of dark matter. The first results of two surveys were presented recently (see Fischer et al. 1999, `http://www.sdss.org` and Van Waerbeke et al. 2000, `http://www.cfht.hawaii.edu/News/Lensing`).

2.2.3 Extreme Scattering Events

Extreme scattering events are significant flux changes detected whilst observing compact radio quasars (Fiedler et al. 1994). The variations are believed to originate from refractive

effects due to plasma lenses crossing the line of sight. Photoionized material and free electrons around the clumpuscules may explain these events (Walker and Wardle 1998).

The photoionized "skin" of a clumpuscule is produced by its interaction with the cosmic ray background radiation. This interaction would also produce γ-ray emission, which is possibly explaining the observed γ-ray background emission (Kalberla et al. 1999, de Paolis et al. 1999).

3 Conclusions

Only about 1 % of the matter in our Universe is visible to us. About 25 % is dark matter and can only be detected via its gravitational interaction with the visible matter. The rest is probably vacuum energy and could make $\Omega_{\text{total}} = 1$ (flat Universe).

According to the theory of Big Bang Nucleosynthesis most of the dark matter has to be non-baryonic. But there is strong evidence that spiral galaxies contain a large amount of baryonic matter, presumably in the form of cold dense clouds of molecular hydrogen. The most promising perspectives for detecting them are quasar absorption lines, gravitational microlensing and extreme scattering events.

However, our current models of dark matter are still rather vague and tentative. Observations and experiments shedding light on its true nature are hard to perform. This quest leads us to the very foundations of modern physics and cosmology and will almost certainly have a deep impact on our understanding of the Universe.

4 Questions and Discussion

This is a summary of the questions asked during the discussion after the talk.

Dr. Thomasson asked: If you derive galaxy cluster masses you are assuming that they are in virial equilibrium. Is that a reasonable assumption?

A. Tappe answered: Yes, it is a reasonable assumption if the age of the cluster is much larger than its dynamical timescale. However, departures from virial equilibrium can be significant, especially in the outer parts. Besides, the assumption of virial equilibrium is the only way to get a simple estimate of the total mass of a cluster with a given velocity distribution. The errors are expected to be comparable to the statistical uncertainties of the measurements and should be at least an order of magnitude less than the mass estimated for the dark matter. For a more complete discussion see Binney & Tremaine (1987, pp. 26-29 and 610-616).

Dr. Thomasson continued: How do spiral galaxies evolve along the Hubble Sequence from type Sd to Sa by forming stars from H_2 gas in the extended disk? How is this gas able to form stars?

A. Tappe replied: I pointed out that spiral galaxies evolve along the Hubble Sequence from late to early types. During that process dark matter seems to be consumed by star formation. According to the model of PCM94 H_2 in spiral galaxies is in the form of cold clouds of molecular hydrogen. Frequent collisions among the clumpuscules, the smallest building blocks of the fractal structure, would prevent star formation.

However, galaxy evolution is a dynamical process. H_2 clouds can possibly join the visible disk and contribute to star formation by loosing angular momentum (see Pfenniger 1997 for more details).

M. Försth asked: What is the source of the X-ray emission from galaxy clusters?

A. Tappe said: Galaxy clusters are among the brightest X-ray sources in the sky. This radiation comes from very hot gas occupying the space between the galaxies of the cluster. The temperature of the gas ranges from 20 to 100 million K, which is probably due to heating caused by the interaction with the galaxies moving through that gas. Its origin is not exactly known. It could in principal be accreted from the outside or blown out from the galaxies in the cluster.

Dr. Liu asked: You mentioned the velocity distribution of galaxies in clusters and the rotation curves of galaxies as evidence for dark matter. Where is the majority of dark matter? Is it inside the galaxies or in between them?

A. Tappe answered: The rotation curves of disc galaxies suggest that we see only about one tenth of the gravitating mass. That means that the amount of dark matter is up to 90 %. Much less is known about the dark matter fraction in elliptical and dwarf galaxies. Observing galaxy clusters in the visible and X-ray light, we sense roughly 20 to 30 % of its total gravitating mass. So, the dark matter fraction is 70 to 80 %. The hot intergalactic gas giving rise to the X-ray emission of the cluster makes up approximately 10 % of the gravitating mass.

In general, a ratio of dark to visible matter around 10:1 could still be caused entirely by baryonic dark matter (consistent with the total amount of visible $\Omega_{\rm vis} \approx 0.005$ and baryonic matter $\Omega_{\rm b} \approx 0.05$). But there is probably a much larger amount of non-baryonic dark matter (note that $\Omega_{\rm CDM} \approx 0.2$). Many candidates have been suggested but so far we only know that these particles are very weakly interacting with themselves and other matter. As a consequence they are probably distributed rather homogeneously.

Since galaxy clusters contain many galaxy types (spirals, ellipticals, dwarfs, ...) in varying amounts, it is difficult to figure out where the majority of dark matter might be. It depends on how much dark matter is contained in all these types. By knowing that we would be able to constrain the amount of dark matter located in between the galaxies. This stuff could be baryonic as well as non-baryonic.

Note finally, that it is probably not easy to distinguish between the "inside" and "outside" of a galaxy. The halos and disks can be quite extended, so that sometimes neighbour galaxies are actually overlapping.

References

Alcock C., et al. 1993, Nature, 365, 621

Binney J., Tremaine S. 1987, Galactic dynamics (Princeton:Princeton university press)

Brau J. 1999, http://blueox.uoregon.edu/~courses/BrauImages/Chap23/FG23_021.jpg

Briel U. G., Henry J. P., Böhringer H. 1992, A&A, 259, L31

Coles P., Lucchin F. 1995, Cosmology - The origin and evolution of cosmic structure (Chichester:Wiley)

Combes F. 1999, http://xxx.lanl.gov/abs/astro-ph/9906477

Combes F., Pfenniger D. 1997, A&A, 327, 453

de Bernardis P., et al. 2000, Nature, 404, 955

de Paolis F., Ingrosso G., Jetzer P., Roncadelli M. 1995, A&A, 295, 567

de Paolis F., Ingrosso G., Jetzer P., Roncadelli M. 1998, ApJ, 500, 59

de Paolis F., Ingrosso G., Jetzer P., Roncadelli M. 1999, ApJ, 510, L103

Dodelson S., Knox L. 2000, PhRvL, 84, 3523

Drain, B. T. 1998, ApJ, 509, L41

Dursi J. 1998, http://www.astro.queensu.ca/~dursi/dm-tutorial/dm1.html

Falgarone E., Puget J.-L., Pérault M. 1992, A&A, 257, 715

Feynman R. P. 1998, The meaning of it all (London:Penguin books); John Danz lectures given by R. P. Feynman in 1963

Fiedler R., et al. 1994, ApJ, 430, 581

Fischer P., et al. 1999, http://xxx.lanl.gov/abs/astro-ph/9912119

Gerhard O., Silk J. 1996, ApJ, 472, 34

Kalberla P. M. W., Shchekinov Yu. A., Dettmar R.-J. 1999, A&A, 350, L9

Laustsen S., Madsen C., West R M. 1987, Exploring the southern sky (Berlin:Springer Verlag)

Lineweaver C. H. 1999, http://xxx.lanl.gov/abs/astro-ph/9911294

Mandelbrot B. B. 1983, The fractal geometry of nature (New York:Freeman)

McGaugh S. S. 1999, ApJ, 523, L99

Paczynski B. 1986, ApJ, 304, 1

Paczynski B. 1996, ARA&A, 34, 419

Perlmutter S., et al. 1999, ApJ, 517, 565

Persic M., Salucci P. 1995, ApJS, 99, 501

Peterson J. B., et al. 2000, ApJ, 532, L83

Pfenniger D. 1996 in New Extragalactic Perspectives in the New South Africa, ed. D. L. Block & J. M. Greenberg (Dordrecht:Kluwer Academic Publishers)

Pfenniger D. 1997 in Dark and visible matter in galaxies, ed. M. Persic & P. Salucci (San Francisco:APS conference series vol. 117)

Pfenniger D., Combes F., Martinet L. 1994, A&A, 285, 79 (PCM94)

Pfenniger D., Combes F., Martinet L. 1996 in New Extragalactic Perspectives in the New South Africa, ed. D. L. Block & J. M. Greenberg (Dordrecht:Kluwer Academic Publishers)

Pfenniger D., Combes F. 1994, A&A, 285, 94

Raffelt G. G. 1997, http://xxx.lanl.gov/abs/hep-ph/9712538

Rowan-Robinson M. 1996, Cosmology (Oxford:Clarendon Press), 3^{rd} edition

Sciama D. W. 2000, MNRAS, 312, 33

Squires G., et al. 1996, ApJ, 461, 572

Tripp T. M., Savage B. D., Jenkins E. B. 2000, ApJ, 534, L1

Turner M. S. 1999, PhyS to appear, http://xxx.lanl.gov/abs/astro-ph/9901109

Turner M. S., Tyson, J. A. 1999, http://xxx.lanl.gov/abs/astro-ph/9901113

van den Bergh S. 2000, PASP, 112, 529
van Waerbeke L., et al. 2000, http://xxx.lanl.gov/abs/astro-ph/0002500
Wagner D., 1999, http://hep-www.colorado.edu/~wagner/susynlc/susynlc.html
Walker M., Wardle M. 1998, ApJ, 498, L125
Walker M., Wardle M. 1999, ApJ, 527, L109
Weinberg S. 1999, SciAm, 12, 36

Fractals and Large-Scale Structure of the Universe

Ģirts Barinovs

Department of Chemistry
Physical Chemistry
Göteborg University
SE-41296 Göteborg, Sweden
(durvis@email.com)

*

Abstract

Important information about the large scale structure of the Universe can be obtained by analysing data from galaxy surveys or luminosity counts. Different mathematical methods of galaxy distribution analysis reveal different aspects of the large scale structure. Classical methods based on correlation function analysis do not work if the distribution of galaxies has fractal properties. Pietronero et al. (1997) used conditional density in order to show that the galaxy distribution is fractal-like on scales up to 1000 h^{-1} Mpc. These results seem to contradict COBE observations, which showed that the mass distribution in the Universe is homogeneous at the same scale. Further important information about the structure of the Universe may be obtained in the future by improving experimental data and refining theoretical methods.

1 Introduction

If we look at pictures from different galaxy surveys, we see that in some parts of the Universe there are huge voids, while in others the concentration of galaxies is very high. In a survey, the position of a galaxy is characterized by two angles on the sky and the redshift, which gives an approximate measure of distance. The first two coordinates can be measured with high accuracy, whereas the redshift requires knowledge of the spectrum and is harder to obtain. Moreover, deducing the distance from the redshift is not trivial, because the redshift contains contributions from both the Universe expansion and the peculiar motion of galaxies. We could imagine that, if in some region all galaxies move in one preferred direction, this could introduce a systematic error into our studies and lead to fake structures.

Galaxy surveys test scales smaller than $100h^{-1}$ Mpc, where $h = H/100$ km s^{-1} Mpc^{-1} and H is the Hubble constant (e.g., Wu et al. 1999). COBE (Cosmic Background Explorer) gives information about scales larger than 1000 h^{-1} Mpc. Studies of X-ray

*Astrophysical Dynamics 1999/2000, Alessandro B. Romeo (Ed.), Onsala Space Observatory, 2000.

background radiation tests intermediate scales. However, the interpretation of X-ray observations depends on the nature and origin of the X-rays.

Some idea about the distance to a galaxy can be obtained from its luminosity. The luminosity distribution turns out to be very useful, but at large distances it is strongly affected by evolutionary effects, thus complicating the interpretation of data.

Another problem is that most of the mass is dark and we observe only a small fraction of the matter present in the Universe (see paper by Tappe in this proceedings book). For example, it is not known how to match the clustering of galaxies with the fluctuations in the cosmic microwave background or results of a numerical simulation. The assumption that fluctuations of mass linearly follows fluctuations of luminosity could be too simple. The relationship could be non-local, nonlinear, stochastic and epoch-dependent as well (e.g., Wu et al. 1999).

2 Distribution of Galaxies

The N-particle distribution function $n(\boldsymbol{r}_1, \boldsymbol{r}_2, \boldsymbol{r}_3, ..., \boldsymbol{r}_N)$ gives complete information about the positions of galaxies in 3-D space. However, it contains too much information and is usually averaged over all coordinates except one, giving the density of the system $n(\boldsymbol{r}_1)$. For homogeneous systems the density is constant.

To characterize the clumpiness of the system, the two-particle distribution function $n(\boldsymbol{r}_1, \boldsymbol{r}_2)$ is used. It describes the probability to find two galaxies at the points $\boldsymbol{r}_1$ and $\boldsymbol{r}_2$.

It is clear that we are not always interested in the exact positions $\boldsymbol{r}_1$ and $\boldsymbol{r}_2$. More convenient is the probability to find a galaxy at distance $|\boldsymbol{r}_1 - \boldsymbol{r}_2|$ from a galaxy located at $\boldsymbol{r}_1$. If this probability is different from that for a homogeneous system, matter is clumped.

In cosmology, a correlation function $\xi(\boldsymbol{r})$ is used:

$$\xi(\boldsymbol{r}) = \frac{< n(\boldsymbol{r}_1) n(\boldsymbol{r}_1 + \boldsymbol{r}) >_{\boldsymbol{r}_1}}{< n >^2} - 1, \tag{1}$$

which is zero for a homogeneous distribution.

3 Fractals

Fractals are ensembles, which are self similar (look the same) at all scales. Pure mathematical fractals do not exist in reality, where objects can only show fractal properties between some limiting scales. The dimension of a fractal can also depend on the scale we are looking at. For a fractal characterized by dimension D, the number of objects N within a volume of radius R can be found as

$$N(R) = BR^D, \tag{2}$$

where B is a proportionality constant. If $D < 3$, the mean density

$$< n >= \frac{N(R)}{V(R)} \tag{3}$$

is not constant. Using

$$V(R) = \frac{4}{3}\pi R^3, \tag{4}$$

we find that

$$< n >= \frac{3}{4\pi} B R^{D-3}, \tag{5}$$

i.e. the average density depends on the size of the sample. If we increase the size of the sample, $R \to \infty$, then the mean density falls to zero, $< n > \to 0$. Therefore the correlation function $\xi(\boldsymbol{r})$ is not uniquely defined (it contains the mean density) and depends on the size of the sample.

The conditional density $\Gamma(r)$ used by Pietronero et al. (1997) is independent of the sample size and thus overcomes that problem:

$$\Gamma(r) = \frac{< n(\boldsymbol{r}_1) n(\boldsymbol{r} + \boldsymbol{r}) >_{\boldsymbol{r}}}{< n >}. \tag{6}$$

It can be shown (e.g., Pietronero et al. 1997) that the conditional density depends only on the intrinsic properties of the fractal:

$$\Gamma(r) = \frac{D}{4\pi} B r^{D-3}. \tag{7}$$

4 Is the Universe Fractal?

Analysing different galaxy catalogues, Pietronero et al. (1997) found that galaxies show a fractal distribution with dimension $D = 2$ up to $150h^{-1}$ Mpc. Using the mass-radius relation, fractal range was extended up to $1000h^{-1}$ Mpc with the same dimension $D = 2$. The fractal properties deduced using different catalogues are similar.

The analysis of luminosity function made by Montuori et al. (1997) seems to confirm these results. They found that for a small sample radius the statistical data are affected by low-statistics fluctuations, resulting in a fractal dimension $D = 3$. For a larger size of the sample, the calculated fractal dimension falls to $D = 2$, confirming the results obtained from the redshift survey analysis.

These results are heavily attacked by other researchers, because they do not show any transition to homogeneity up to the scale tested by COBE. Is the Universe homogeneous at very large scales?

As already mentioned, the galaxy surveys test scales $\leq 100h^{-1}$ Mpc and show a fractal distribution, whereas COBE tests scales $\geq 1000h^{-1}$ Mpc and finds a homogeneous distribution. It is obvious that, in order to test the intermediate scales, we should improve the angular resolution of the cosmic microwave background studies or make deeper galaxy surveys. Indeed, there are plans to explore the cosmic microwave background at scales $\leq 300h^{-1}$ Mpc (balloon experiments and ground based observations will map small areas of sky, while MAP and Planck satellites will achieve all-sky coverage).

There are many technical details that should be considered when calculating the correlation function $\xi(r)$ or the conditional density $\Gamma(r)$ (Martinez, 1999). The results are scaled at small sample radii, in order to correct for the fluctuations arising in the density due to nonstatistical behaviour when the number of galaxies inside the sample is small. It is not clear how to do it correctly, therefore different approaches could introduce artificial homogeneity or spurious fractal structure.

The completeness of the sample should also be ensured, otherwise the data would heavily depend on our assumptions about the galaxy distribution. Furthermore, different estimators are used to correct for boundary effects and evolutionary effects (become important at scales $\geq 300h^{-1}$ Mpc).

Most researchers agree that there is strong evidence for a fractal distribution of matter, at least at small scales (e.g., Wu et al. 1999). But large controversy arises when discussing the scale of transition to a homogeneous distribution.

As we already mentioned, another problem with most surveys is that they test the distribution of luminosity, not the distribution of mass. Therefore, a fractal distribution of galaxies does not mean a fractal distribution of mass. In contrast, numerical simulations, test the distribution of mass.

COBE (1992) found fluctuations in the microwave background of about 10^{-5}, which are thought to be fluctuations in the metric and therefore to describe the distribution of mass.

There are several possibilities to measure the mass distribution:

- from studies of peculiar velocities of galaxies;
- from studies of the cosmic microwave radiation;
- from studies of gravitational lensing.

The fractal distribution of galaxies can by explained by numerical simulations using the cold dark matter model, at scales $\leq 100h^{-1}$ Mpc (Wu et. al 1999). Models involving bubbles are also suggested and give a fractal dimension $D = 2$ at small scales and $D = 3$ at scales larger than the bubble size.

The next generation of redshift surveys and COBE successors, together with more sophisticated mathematical methods, could give more conclusive data about the large-scale structure of the Universe.

5 Questions and Discussion

Magnus Thoomasson

The large-scale structure in the Universe is fractal, but also small-scale structures like interstellar clouds. How do fractal structures at those different scales fit together?

Ģirts Barinovs

Real fractals are different from mathematical fractals because they exhibit fractal properties between two limiting scales. The smallest unit when studying the large scale structure of the Universe is a galaxy, the largest is the visible Universe. For the interstellar clouds the fractal properties are observed starting from a size from 0.0001 pc up to the scale of the largest interstellar clouds, 100 pc, and therefore they do no overlap.

Acknowledgements

I would like to thank Alessandro for the interesting course he has given. I would also like to thank my Latvian friends, K. Bērziņš and F. Pianca, for helping me to find the literature and for exciting discussions about the structure of the Universe.

References

Martinez V. J., 1999, Sci 284, 445

Montuori M., Sylos Labini F., Gabrielli A., Amici A., Pietronero L., 1997, Europys. Lett. 39, 103

Pietronero L., Montuori M., Sylos Labini F., 1997, In: Schramm D. N., Galeotti P. (eds.) Generation of Cosmological Large-Scale Structure. Kluwer Academic Publishers, Dordrecht, p. 105

Wu K. K. S., Lahav O., Rees M. J., 1999, Nat, 397, 225

Magnetohydrodynamic Turbulence in Accretion Discs

Rim Turkmani

Department of Theoretical Physics
Chalmers University of Technology and Göteborg University
SE-41296 Göteborg, Sweden
(rim@fy.chalmers.se)

*

Abstract

One key question in astrophysics is to explain how gas can be accreted onto compact objects. Molecular viscosity is generally too low for transporting angular momentum outwards at a sufficient rate, so there should be a source of anomalous viscosity responsible for the process of accretion, which is believed to be turbulence. But how is turbulence generated? In 1991, Balbus and Hawley suggested that it may be driven by MagnetoHydroDynamical (MHD) instabilities. Since then, considerable effort has been devoted to investigate such instabilities. In this paper, I review theory and computer simulations of magnetohydrodynamic turbulence in accretion discs, and discuss certain major numerical works. In particular, I focus on measurements of the turbulent shear stress α in shearing-box models. I also briefly compare the results of numerical simulations with observations.

1 Introduction

In a binary system containing an ordinary star and a compact object (white dwarf, neutron star or black hole), gas can spiral from the star onto the object, so producing a flow of matter with the shape of a disc: an accretion disc. The importance of accretion power was recognized in the 1960s and early 1970s, following the expansion of observational techniques into new wavelength bands. Shakura & Sunyaev (1973), and also Lynden-Bell & Pringle (1974), layed the foundation for the 'standard model' of accretion discs. After such works, great effort has been devoted to understand the physics of accretion discs, but the critical problem concerning the origin of turbulence is not yet satisfactorily solved. The equations that describe the disc cannot be solved analytically without restrictive assumptions. So numerical solutions have been obtained by using methods developed in computational fluid dynamics. To make numerical simulations practicable, one needs to select the major physical contributions. Early works neglected magnetic fields but, since the discovery of a linear instability in weakly magnetized discs (Balbus & Hawley 1991), it has become clear that such an approximation misses important physical effects.

*Astrophysical Dynamics 1999/2000, Alessandro B. Romeo (Ed.), Onsala Space Observatory, 2000.

The paper is organized as follows. In Sects. 2 and 3, I review the basic theory of MHD turbulence in accretion discs. In Sect. 4, I review relevant numerical methods of computational fluid dynamics. In Sect. 5, I discuss MHD simulations and, specifically, certain leading papers published in this field. I focus on measurements of the turbulent shear stress α in shearing-box models and compare the values of α obtained with different simulations. In Sect. 6, I further discuss the results of such simulations and compare them with observations.

Table 1: Symbols and Quantities

Symbol	Quantity
$\mathbf{A}$	Magnetic vector potential
B	Magnetic field
c	Speed of light
c_s	Sound speed
H	Half thickness of the disk
$\mathbf{F}_{\rm rad}$	Radiative flux
G	Gravitational constant
$\mathbf{J}$	Current
P	Pressure
$\mathbf{U}$	Fluctuating velocity
$\mathbf{v}$	Fluid velocity
T	Temperature
$\mathbf{V}_{\rm A}$	Alvén velocity
$r_{\rm in}$	Inner edge of the disk
α	viscosity parameter
α_M	Maxwell stress tensor
α_R	Reynolds stress tensor
β	Ratio of gas pressure to total pressure
γ	Polytropic index
η_B	Magnetic diffusivity
η_v	Dynamic viscosity
ν	Kinematic viscosity
ρ	Density
Σ	Surface density of the disk
θ	Polar angle
Φ	Gravitational potential

2 Basic Equations

The basic equations of magnetohydrodynamics are (Balbus and Hawley 1998):

$$\frac{\partial \rho}{\partial t} + \nabla \cdot (\rho \mathbf{v}) = 0, \tag{1}$$

$$\rho \frac{\partial \mathbf{v}}{\partial t} + (\rho \mathbf{v} \cdot \nabla)\mathbf{v} = -\nabla \left(P + \frac{B^2}{8\pi} \right) - \rho \nabla \Phi + \left(\frac{\mathbf{B}}{4\pi} \cdot \nabla \right) \mathbf{B} + \eta_v \left(\nabla^2 \mathbf{v} + \frac{1}{3} \nabla (\nabla \cdot \mathbf{v}) \right), \tag{2}$$

$$\frac{\partial \mathbf{B}}{\partial t} = \nabla \times (\mathbf{v} \times \mathbf{B} - \eta_B \nabla \times \mathbf{B}). \tag{3}$$

Eqs. (1), and (2) express the conservation of mass and momentum, respectively, and Eq. (3) is the induction equation. In writing (2) and (3) I have assumed a magnetized plasma of ions and electrons. The constraint $\nabla \cdot \mathbf{B} = 0$ is fulfilled by Eq. (3), if it is imposed as an initial condition.

2.1 Energy

For a gas of adiabatic index 5/3 (fully ioneized hydrogen), the equation for the internal energy reads:

$$\rho(\frac{\partial}{\partial t} + \mathbf{v} \cdot \nabla)\frac{3P}{2\rho} = -P\nabla \cdot \mathbf{v} - \nabla \cdot \mathbf{F}_{\rm rad} + \Psi, \tag{4}$$

where Ψ is the volumetric heating rate due to both viscous and ohmic dissipation.

2.2 Angular Momentum

If the accreting gas has a non-zero angular momentum with respect to the accreting object, it will not accrete directly into the compact Object. The disc evolves as the gas gives up some of its angular momentum and spiral down the gravitational potential. The transport of angular momentum is the most fundamental process in an accretion disc. The equation of angular momentum conservation follows from considering the azimuthal component of Eq. (2):

$$\begin{aligned}\frac{\partial}{\partial t}(\rho R v_\Phi) + \nabla \cdot R\left[\rho v_\Phi \mathbf{v} - \frac{B_\phi}{4\pi}\mathbf{B_p} + (P + \frac{B_p^2}{8\pi})\hat{e}_\phi\right] \\ -\nabla \cdot \left[\frac{R\eta_v}{3}(\nabla \cdot \mathbf{v})\hat{e}_\phi + \eta_v R^2 \nabla \frac{v_\Phi}{R}\right] = 0.\end{aligned} \tag{5}$$

Where $\hat{e}_\phi$ is the unit vector in the azimuthal direction, B_ϕ and B_p are the azimuthal and the poloidal components of the magnetic field, respectively.

2.3 Alpha

In all the steady state models, the viscosity was parameterized in term of the so-called α which was introduced by (Shakura & Sunyaev 1973). The only constrain about α is that it is constant and can be less than or equal to unity. The vertically integrated viscous stress, W is responsible for this transport, and it has been assumed to be propotional to the vertically integrated pressure, P

$$W = -\alpha P. \tag{6}$$

Another formulation for α is provided by (Pringle 1981)

$$\nu_t = \alpha c_s H, \tag{7}$$

which is a scaling based on the form of a microscopic shear viscosity.

3 Instabilities and Turbulence in Accretion Discs

The most fundamental process in accretion discs is angular momentum transport. The disc cannot evolve unless the gas in the disc can be persuaded to give up some of its angular momentum and spiral down the gravitational potential. Turbulence in discs is astrophysicaly important because it can transport angular momentum through shear stresses and thus allow discs to evolve and accrete. Turbulence can be initiated by magnetic, gravitational, or purely hydrodynamic instabilities. Numerical experiments with a local model (Balbus et al. 1996), however, failed to find any evidence of nonlinear instability in Keplerian shear flows, thus suggesting that Keplerian discs are nonlinearly stable.

3.1 Magnetohydrodynamic Instabilities

The linear MHD instability was first discovered by Velikhov (1959), and first understood in the context of accretion discs by Balbus and Hawley (1991). The simplest fluid system displaying this instability (BH instability) is an axisymmetric gas disc in the presence of a weak vertical magnetic field. The field has no effect on the disc equilibrium, which is determined by a balance of gravitational and rotational forces. The mechanical analog, developed by Balbus & Hawley (1992), is the easiest way to illustrate the BH instability. Consider two particles with equal masses in a Keplerian orbits. The masses are close together in the sense that $\frac{|\delta r|}{r} \ll 1$, (where r is the radius of the orbit) and they are connected by a spring with a natural frequency γ. The masses represent fluid elements and the spring represents the magnetic field if

$$\gamma^2 = (\mathbf{k} \cdot \mathbf{V_A})^2, \tag{8}$$

where $\mathbf{V_A} \equiv \frac{\mathbf{B}}{\sqrt{4\pi\rho}}$ is the Alfven velocity and $\mathbf{k}$ the wave vector. This analog is exact in the case of a purely vertical magnetic field and a vertical wave vector in ideal MHD.

There are two effects which can shut off the powerful BH instability:

- *Low-ionization fluids:* The weak-field magnetic instability will be important only if the fluid is sufficiently ionized that there is a good coupling between the gas and $\mathbf{B}$. When the disc is poorly ionized the instability can be damped by either ordinary resistivity or ambipolar diffusion.

- *A strong magnetic field:* To determine the stability conditions here one must examine the vertical or radial structure of a specific disc model to determine the precise stability conditions. A strong field can shut off the instability only if the smallest-scale unstable mode has a wavelength comparable to the disc scale height, so that the unstable modes no longer fit within the disc.

4 Numerical Methods

Computational fluid dynamics (CFD) is the science of obtaining numerical solutions to a system of partial differential equations that describes a fluid flow. It is a fast growing branch of computational physics which relates to different topics, fluid mechanics, the theory of partial differential equations, numerical analysis, and computer science. CFD is done by discrete methods like: finite difference methods (FDM), finite element method

(FEM), and smooth particle hydrodynamics (SPH), finite volume methods, spectral methods. I will discus here the differences between FDM and SPH. SPH is a Lagrangian method, that is the particles follow the fluid flow. The particles carry all the computational information. Thus, there is no "computational grid". The particles themselves are the computational framework on which the fluid equations are solved. This makes the method easy to implement even for problems with complicated geometries. FDM is more difficult to implement than SPH but easier than FEM. Most SPH calculations have treated shocks using variants of the von Neumann-Richtmyer artificial viscosity. This spreads shock fronts over a few particle smoothing lengths, which can be considered as a large distance in 3D simulations. In FDM the shocks are more sharp due to the lower value of the effective viscosity. There have been some attempts to solve the equations of (generally) ideal magnetohydrodynamics within a particle based framework but it is yet unclear whether SPH incorporating MHD is a good idea. The MHD equations are solved successfully in many simulations using FDM. Trying to make the simulations more realistic by adding more physics like radiation transport and thermodynamics is easier and more straight forward in FDM than in SPH.

5 Numerical Simulations of MHD Discs

Supercomputer simulations have been used in conjuction with analytic studies to investigate the nature of the angular momentum transport in accretion discs. Simulations provide a means to investigate and experiment with global hydrodynamic instabilities, spiral shock waves, and local MHD instabilities. These results suggest that the fundamental physical mechanism of angular momentum transport in accretion discs has now been identified.

5.1 The Shearing Box Model

The shearing box represents a small piece of a cylindrical Keplerian accretion disc with a Cartesian box rotating with the flow. It is a model which is based on a local expansion of the equations of motion. One picks out a fiducial disc radius R_0 and restricts the analysis to a local patch of linear extent much less than R_0. Using this approximation, the compressible ideal MHD equations for a fluid are:

$$\frac{\partial \mathbf{v}}{\partial t} + \mathbf{v}\cdot\nabla\mathbf{v} = -\frac{1}{\rho}\nabla\left(P + \frac{B^2}{8\pi}\right) + \frac{(\mathbf{B}\cdot\nabla)\mathbf{B}}{4\pi\rho} - 2\boldsymbol{\Omega}\times\mathbf{v} + 2q\Omega^2 x\hat{\mathbf{x}} - \Omega^2 z\hat{\mathbf{z}}, \tag{9}$$

$$\frac{\partial \mathbf{B}}{\partial t} = \nabla\times(\mathbf{v}\times\mathbf{B}), \tag{10}$$

$$\frac{\partial \rho}{\partial t} + \nabla\cdot(\rho\mathbf{v}) = 0, \tag{11}$$

$$\frac{\partial \rho\epsilon}{\partial t} + \nabla\cdot(\rho\epsilon\mathbf{v}) = 0, \tag{12}$$

$$P = \rho\epsilon(\gamma - 1). \tag{13}$$

The term $2q\Omega^2 x$ in the first equation is the expansion of the effective gravitational force (centrifugal + gravitational) at the fiducial point. The constant $q \equiv -\frac{d \ln R}{d \ln R}$; for a Keplerian disc $q = \frac{3}{2}$. The last two equation are the (internal) energy equation and the equation of state for an ideal gas, respectively. (Hawley et al 1996). *B*oundary conditions: The computational domain is a rectangular prism with sides L_x,L_y, and L_z. The shearing box is assumed to be surrounded by identical boxes that are strictly periodic at $t = 0$. A large-scale continuous linear shear flow is present across all the boxes. Thus, at later times the computational box remains periodic in y and z, while in the radial x direction the neighboring boxes are displaced relative to one another in response to the shear flow. We will see the implementation of the shearing box model in different simulations in the coming sections.

5.2 Unstratified Magnetized Shearing Boxes

The unstratified models neglect the vertical structure of the disc, which means:

$$\frac{\partial \phi}{\partial z} = 0, \tag{14}$$

$$\frac{\partial \rho}{\partial z} = 0. \tag{15}$$

This approach is less realistic, but it is also less demanding from a numerical point of view. An advantage is that it allows the study of the nonlinear development of the BH instability independent of buoyancy effects. The model is specified by a group of parameters:

- The shape and size of the box relative to $H = c_s\Omega$. Typically

$$L_x \times L_y \times L_z = (1 \times 2\pi \times 1)H. \tag{16}$$

- The numerical resolution, usually 2^5 to 2^7 grid points along each axis.
- The mean magnetic field $\langle B \rangle$, as measured by comparing the Alfven speed with c_s

The boundary conditions force $\langle B_z \rangle$ and $\langle B_r \rangle$ to be constant in time, while $\langle B_\phi \rangle$ is fixed if and only if $\langle B_r \rangle = 0$. All the simulations that adopted the unstratified model showed the development of MHD turbulence initiated by BH instability and the final state was always independent of all the initial conditions except the mean magnetic field

5.2.1 Numerical Simulations of Unstratified Shearing Boxes

A typical example of these simulations is the work by Hawley, Gammie, & Balbus (1995). It focuses on the onset of the BH instability and the efficiency of angular momentum transport as measured by α , the ratio of the shear stress $W_{r\phi}$to the pressure P

$$\alpha = \frac{2}{3}\frac{W_{r\phi}}{P}. \tag{17}$$

The three-dimensional simulations are local in the sense that they neglect gradients in pressure and density. Their numerical scheme is based on a method of characteristics-constrained transport-algorithm. Density and pressure are constant in the absence of a vertical gravitational force and a uniform shear flow

$$v = -q\Omega x\hat{y}. \tag{18}$$

Boundary conditions: They are periodic in the vertical and azimuthal directions, and shearing periodic in the radial direction. They can be expressed mathematically for a flow attribute f as

$$f(x, y, z) = f(x + L_x, y - q\Omega L_x t, z), \tag{19}$$

$$f(x, y, z) = f(x, y + L_x, z), \tag{20}$$

$$f(x, y, z) = f(x, y, z + L_z). \tag{21}$$

These boundary conditions apply to all variables except the azimuthal component of the velocity, v_y ,which must be adjusted to account for the relative shear between neighboring boxes. Specifically, the azimuthal velocity on the radial (x) boundary at time t is:

$$v_y(x, y, z) = v_y(x + L_x, y - q\Omega L_x t, z) + q\Omega L_x. \tag{22}$$

At times $t = nL_x q\Omega L_x$, $n = 1, 2, 3, ...$ the boxes become strictly periodic again. Such instants are referred to as periodic points.

Results: The simulations showed numerically that magnetic field strength and geometries that were unstable in 2 dimensions remained unstable in 3 dimensions. The linear growth rate obtained from the numerical simulations was in agreement with the local analysis of BH. A significant transport of angular momentum is achieved. The Shakura Sunyaev parameter α can be computed by dividing the measured stress by the initial gas pressure. For the vertical field fiducial model the anomalous viscosity varies over the range $\alpha = 0.2 - 0.7$. In the toroidal field fiducial simulations α is an order of magnitude smaller with $\alpha \sim 0.02 - 0.08$. From the numerical results of the different runs of this simulation I notice the following:

- α scales with the square of the imposed magnetic field strength.
- The calculated value of α varies considerably when varying the box size L_x, L_y, L_z.
- The value of α obtained from this simulation is influenced by other factors, such as artificial viscosity, resistivity, and the numerical resolution.

The weakness of the unstratified shearing box is that the pressure is completely arbitrary. The equations do not change if one adds a constant to the pressure. Hence, there is not an unique way of measuring the magnetic field strength and consequently their estimates of α are meaningless. It is easy to explain the scaling with the square of the imposed magnetic field. The imposed magnetic flux is conserved by the boundary conditions, and serves as the source of the turbulent magnetic field, which is proportional to the imposed flux. The stress is proportional to the product of the turbulent magnetic field and the imposed flux, that is it is proportional to the square of the imposed magnetic flux.

5.3 Stratified Magnetized Shearing Boxes

This model is more realistic than the unstratified model as it includes the vertical tidal potential

$$\Phi = \frac{1}{2}\Omega^2 z^2, \tag{23}$$

so that the vertical density distribution, assuming that the gas is isothermal, is

$$\rho = \rho \exp(\frac{-Z^2}{2H^2}). \tag{24}$$

The stratified shearing boxes include low density regions that require small time steps to fullfil the Courant condition.In this model and because of the high Alfven velocity only a fraction of the zones are assigned to the turbulent center of the disc, the rest are assigned to the nearly force-free disc atmosphere.

5.3.1 Numerical Simulations of Stratified Shearing Boxes

The most important works on stratified shearing boxes are Brandenburg, Nordlund, Stein, & Torkelsson (1995), Stone, Hawley, Gammie & Balbus,S.A. (1996) and Miller,K.A. & Stone,J.M. (2000). In addition to the nature of angular momentum transport the two papers investigated the dynamo activity in accretion discs too.

- **Brandenburg, Nordlund, Stein & Torkelsson (1995)**

The Model: A local three dimensional model simulation, which includes the effects of compressibility and stratification, that aims at finding a dynamo which generates its own turbulence. The basic equations of the simulation are rewritten in such a way that the variables do not have any systematic variation along the x direction. This is achieved by solving only for the deviations u from the Keplerian shear flow . The induction equation is solved for the magnetic vector potential A to ensure that the magnetic field $B = \nabla \times A$ is divergence-free. The governing equations are solved using sixth-order compact derivatives and the third-order Hyman scheme for the time stepping. The grid is constructed with larger spacing in the toroidal direction, because the flow is much smoother in this direction. The model does not allow any actual transport of matter though the disc, because the shearing box is too symmetric.

Boundary conditions: A vertical magnetic field boundary conditions is used on the upper and lower surfaces

$$\frac{\partial A_x}{\partial z} = \frac{\partial A_y}{\partial z} = A_z = 0. \tag{25}$$

Where A_x, A_y and A_z are the components of the magnetic vector potential A. The boundary conditions at the top and bottom of the box are stress- free, and insulating i.e

$$\frac{\partial u_x}{\partial z} = \frac{\partial u_y}{\partial z} = u_z = \frac{\partial e}{\partial z} = 0. \tag{26}$$

Periodic boundary conditions are assumed in the toroidal y direction, and shearing periodic boundary conditions in the radial x direction for all the eight dependent variables. This mean that the flow is periodic with respect to a position in y that is sliding in time with the local Keplerian shear speed. The magnetic flux in the z direction is conserved by the periodic boundary conditions in y direction and quasi periodic boundary conditions in x direction. The radial and azimuthal boundary conditions used in this simulation are the same as in the paper by Stone at al. (1996), but the vertical boundary conditions are different. The vertical boundary conditions used by Brandenburg et al. (1995) do not allow vertical outflow, but they allow the azimuthal magnetic-flux component to change with time, while Stone et al (1996) used periodic boundary conditions in z , which allow flow through the vertical boundaries, but do not allow $\langle B_\phi \rangle$ to evolve. The azimuthal

boundary conditions used by Brandenburg et al. (1995) have the advantage that it enables them to find changes in $\langle B \rangle$, including several field reversals.

Results: The simulations showed that dynamo-generated turbulence is a viable mechanism for turbulent transport in accretion discs. The energy flows from the Keplerian motion into both magnetic and kinetic energies, but around six times more energy goes into the magnetic energy as into the kinetic energy. The Lorentz force pumps half of this magnetic energy flow into kinetic energy. The total α parameter, varies in different models between 0.001 and 0.005. This value is dependent on the resolution such that it increases with improved resolution. The calculated value is remarkably small, which can be justified by:

- The small ratio of the magnetic pressure to the gas pressure.
- The small value of the $\frac{\langle B_x B_y \rangle}{B^2}$, as B_x is smaller than B_y which may depend on the resolution

- **Stone, Hawley, Gammie & Balbus (1996)**

The Model: This group presented a three-dimensional magnetohydrodynamical simulation of the nonlinear evolution of the BH instability in an initially isothermal, vertically stratified model which is local in the plane of the disc but global in the vertical direction in the sense that the computational domain encompasses several scale heights.

The Boundary Conditions: The boundary conditions are quasi-periodic in the toroidal radial direction. In the vertical z-direction boundary conditions are periodic in most of the simulations.These boundary conditions do not allow $\langle B_\phi \rangle$ to evolve.

Results: The unstratified models saturate at a higher level of magnetic energy than the stratified models with comparable initial field strengths, but in general the properties of the saturated turbulent states are similar in the two sets of simulations. The simulations show that weak magnetic fields are unstable and lead to the development of anisotropic MHD turbulence. The turbulence produce Reynolds and Maxwell stresses that transport a significant amount of angular momentum outwards through the disc. The total stress is proportional to the magnetic pressure. The simulations were also used to investigate the dynamo action in accretion discs. The instability acts as a MHD dynamo which amplifies and maintains the magnetic field. The simulations have been used also to study the effect of the turbulence on the vertical structure of accretion discs. After saturation the disc consists of a weakly magnetized core surrounded by a strongly magnetized corona. Changing the vertical boundary conditions does not significantly alter this structure. The vertical structure produced by the instability, particularly the presence of a strongly magnetized corona, may be of relevance to the production of MHD winds from discs.The disc is also stable to buoyancy instabilities, so that buoyancy does not play an important role as a saturation mechanism. $\alpha \leq 0.01$ for most of the simulations, The value obtained for α here may be limited by the numerical resolution of the simulation. It was also found that α is not constant with height as is commonly assumed.

- **Miller & Stone (2000)**

The Model: This group used a three-dimensional magnetohydrodynamical simulations to study the formation of corona above an initially magnetized, isothermal accretion disc. The simulations are local in the plane of the disc, but extended to 5 vertical scaleheights above and below it.

The Boundary Conditions: Periodic shearing boundary conditions are adopted in the x and y directions, while in the z direction free (outflow) boundary conditions which allow mass, energy, momentum, and magnetic field to leave the grid is implemented.

Results: For initially toroidal fields, or poloidal field with a vanishing mean, MHD turbulence driven by the BH instability produces strong amplification of weak fields within two scale heights of the disc midplane in a few orbital times. On long timescale the average vertical disk structure consists of a weakly magnetized turbulent core below two scale heights and a strongly magnetized corona which is stable to the BH instability above. The functional form of the stress with vertical height is best described as flat within $\pm 2H_z$, but propotional to the density above $\pm 2H_z$. The calculated value of α is fairly constant in the disc, the simulations yield an average value of 0.027 for the α parameter within the disc core.

5.3.2 The Effects of Stratification

As real accretion discs are gravitationally stratified, simulations that include vertical gravity are of course more realistic. The effects of stratification on the evolution of a weak magnetic field are small. The weak-field linear instability is not affected by stratification since the most unstable displacements lie in planes normal to the stratification. Even the nonlinear development of the instability continues like it does in unstratified simulations. The stratified models are more difficult to run. Mainly because the amplitude of MHD waves increases with height. This property makes a small numerical error affect the dynamics of the disc severely. The strong MHD waves generated by this active phenomena can be reflected at the numerical boundary producing a physical resonance near the upper boundary leading to numerical instability. One of the methods to overcome this difficulty is to move the upper boundary as far as possible from the disc center using a non-uniform grid, which physically eliminates the change of wave reflection. Another difficulty is that in gravitationally stratified gas layers, various instabilities occur owing to the gravitational free energy, such as convective instabilities, magnetic buoyancy instabilities including the Parker instability...etc. These instabilities, and the resulting mass motion generate various MHD waves and electric currents which could be a source of heat. Magnetic fields significantly enhance the activity of a gravitationally stratified gas layer through coupling with convection and rotation and magnetic buoyancy.

5.4 Global Models

There is so far only two global three-dimensional calculation that includes a magnetic field: Armitage (1998), and Hawley, J.F. (1999) I will review here the Armitage (1998) paper.

- **Armitage (1998)**

The Model: The paper studied the global development of MHD turbulence in accretion discs with a simplified disc model that omits the vertical stratification. The calculations are performed in a volume bounded by $R_{in} = 1$ $R_{out} = 4$, $Z = \pm H = 0.4$. The vertical component of gravity is neglected, that is:

$$\Phi = \Phi(r) = \frac{1}{r}. \tag{27}$$

Boundary conditions: They are periodic in Z, reflecting at

$$r = r_{in}(v_r = B_r = 0), \tag{28}$$

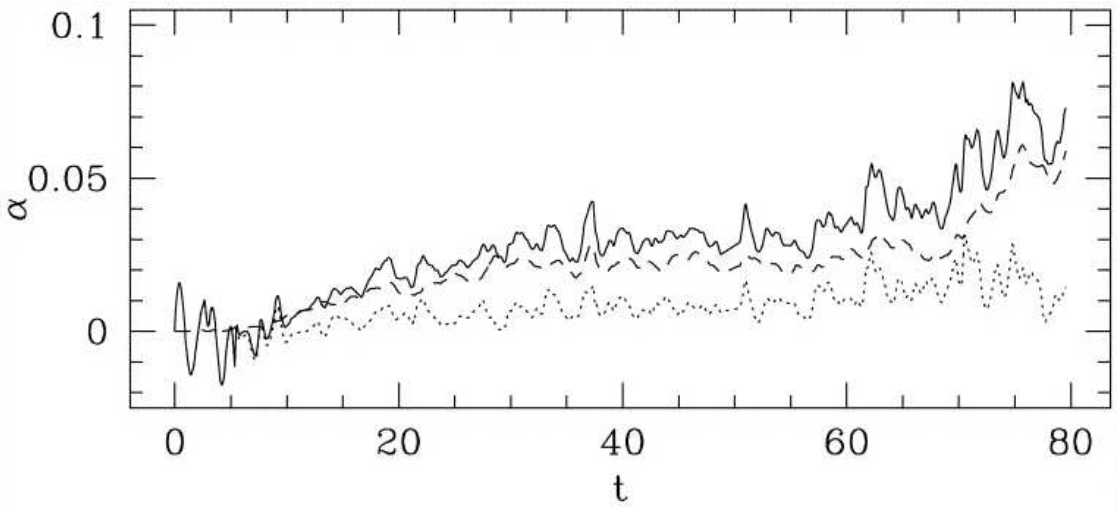

Figure 1: Example of global simulations results (Armitage 1998). Derived Shakura-Sunyaev α parameter at the centre of the grid. The solid line shows the total α, the dashed and dotted lines the contribution from magnetic fluid stress respectively.

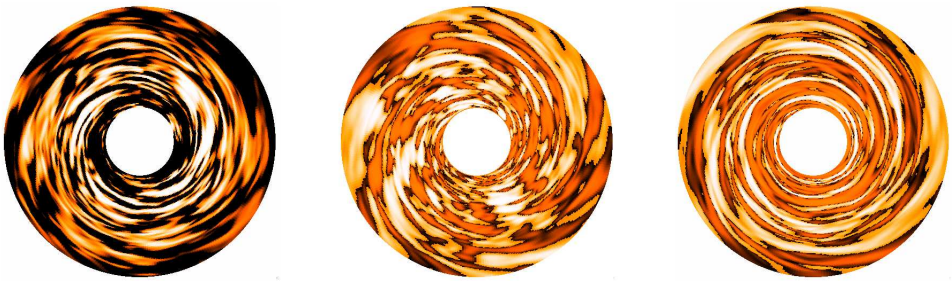

Figure 2: Example of global simulations results (Armitage 1998). The integrated vertical, radial and azimuthal components of the magnetic field, at $t = 80$ orbits.

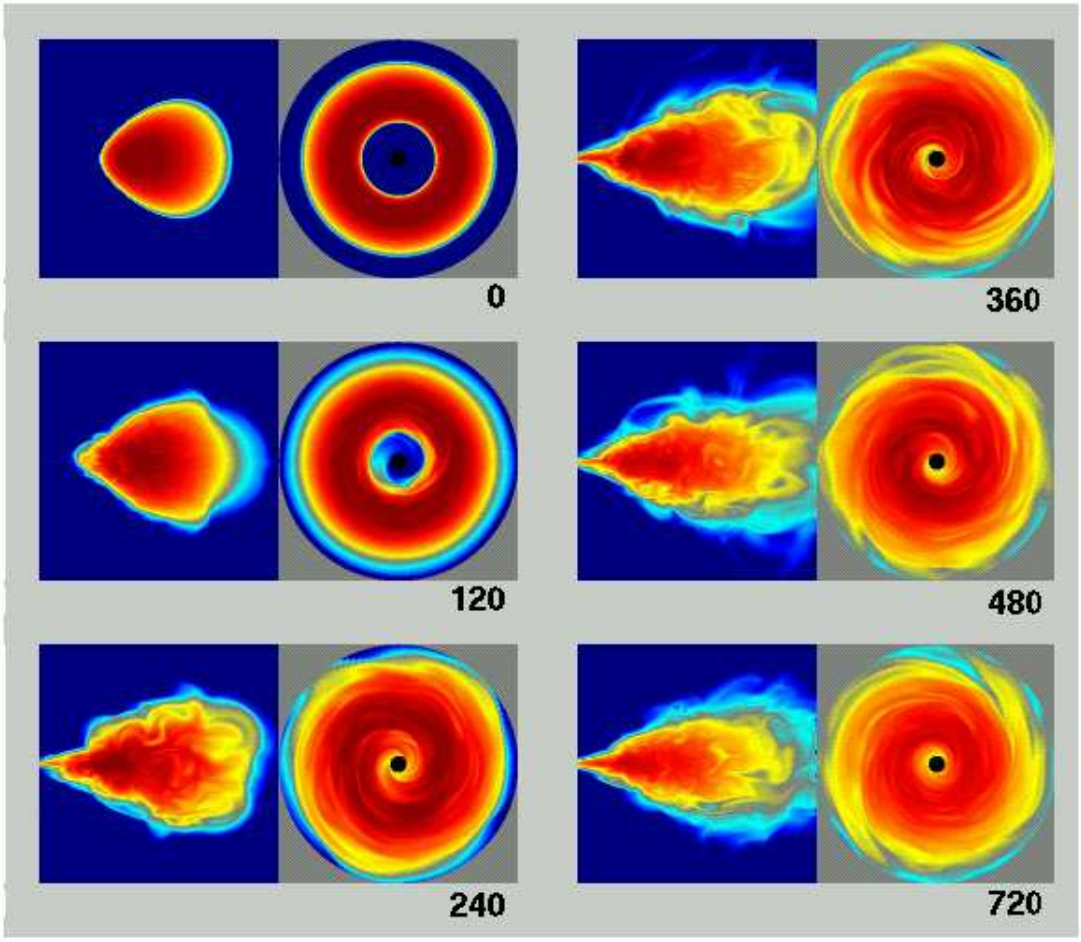

Figure 3: Example of global simulations results (Hawley 1999). Plots of log density labelled by time. At t=120 the BH instability has appeared.

and set to outflow at $r = r_(out)$. The outflow is implemented as a simple extrapolation of the fluid variables into the boundary zones. This boundary condition r_out admits the development of a net vertical magnetic flux as material leaves the grid. The choice of outflow boundary conditions was motivated by the desire to reduce the amplitude of reflected waves at the edge of the grid.

Results: As expected from the local simulations, the MHD instabilities generate sustained turbulence that leads to outward transport of angular momentum. The values of α is calculated to be: $\alpha_M \approx 0.17$. A net vertical magnetic field significantly enhances the strength of the turbulence and raise the derived value of α. Let us compare the resolution in this simulation to the resolution in the local simulations. The grid uses $(n_r = 128, n_\phi = 320, n_z = 32)$ zones. In the ϕ direction $l_\phi = 2\pi R$, and the length of a single grid cell is $\frac{L_\phi}{n_\phi} = \frac{2\pi}{320}R = 0.019R$. The size of the complete shearing box of the local model (Brandenburg et al., 1995). Is $L_\phi = 2\pi H$,with $\frac{H}{R} = \frac{1}{100} = 0.01$, and so L_ϕ is $L_\phi = 2\pi 10^-2R$. We see that the entire shearing box extends over merely 3 grid elements of the global simulation. The poor resolution in the global simulation means that it is using a much larger numerical viscosity.

6 Discussion

6.1 Simulation Results

We have seen that all the simulations confirm the linear stability analysis pioneered by Balbus & Hawley (1991). A weak magnetic field of any topology leads to turbulence and outward transport of angular momentum. There is a wide range of published values of α: from 0.6 with a net vertical field in an unstratified shearing box (Hawley et al., 1995) to 0.001-0.005 for a stratified box without any imposed magnetic field (Brandenburg et al., 1995). Trying to investigate the reasons behind this wide range of values we consider the following:

- The effect of the boundary conditions used.
- Disc structure (local or global).
- Resolution: In some simulations (like Hawley et al 1995) the value of jumped an order of magnitude with higher resolution, sufficiently high resolution is hard to achieve as it is limited by the speed and memory of the computer.All the groups report numerical dependencies in the precise numbers resulting from the simulations. Higher resolution results in larger magnetic field levels, stronger turbulence and larger transport rates.
- The numerical algorithms used, as better algorithms enable us to include more physics which makes the model more realistic.
- Mean magnetic field strength: According to Gammie (1998) α depends on the magnetic field as

$$\alpha = 0.01 + 4\langle v_{Az}\rangle c_s + 14\langle v_{A\phi}\rangle c_s. \tag{29}$$

  where $\mathbf{V_A} \equiv \frac{\mathbf{B}}{\sqrt{4\pi\rho}}$ is the Alfven velocity and $\langle v_{A_z}\rangle$ is the Alvén velocity corresponding to the net vertical field. We can see here that for weak mean fields, $\alpha \approx 10^-2$, while an intermediate strength mean field raise α above this base level. For mean fields that are strong the above equation does not apply.

6.2 Comparison with Observations

Unfortunately there are not so many observations of accretion discs that can be Compared with the theoretical models and the results of the simulations. α can be measured from observations of the dwarf novae outbursts which yield $(0.1 - 0.2)$ which is an order of magnitude larger than the numerically calculated value. Future simulations, which are expected to be more realistic with a higher resolution, more physics, and a global model are expected to give a more accurate value of α. It may be that the difference between the observed and calculated values is a sign that tells us that something is missing in the current models. Future more detailed observations and more realistic numerical simulations may give a better answer to this and help in forming a clearer image about what is going on in the accretion disc. Away from measuring the value of alpha there is another dilemma when comparing with the observations. A stellar astronomer takes as sign of magnetic variability, rapid flare-like variability, emission lines, and non-thermal radiation. In many observed systems the accretion disc seems to switch between two stares with different accretion rates. We expect the magnetic field to be most important in the high state where we need a more efficient mechanism for angular momentum transport, but signs for magnetic activity are more typical for the low state. A possible explanation for this is that magnetic fields are present in both states, but are manifested in different ways. Possibly there are only small-scale fields and the variability associated with them present in the low state. In the high state we expect the small-scale magnetic variability is either quenched for some reason or drenched in the increased overall luminosity of the disc.

References

Armitage P.J., 1998, ApJ 501, L189

Balbus S.A., Hawley J.F., 1991, ApJ 376, 214

Balbus S.A., Hawley J.F., 1996, ApJ 467, 76

Balbus S.A., Hawley J.F., 1998, Rev. Mod. Phys. 70, 1

Brandenburg A., Nordlund A.R., Stein F., Torkelsson U., 1995, ApJ 446, 741

Hawley J.F., Balbus S.A., 1995, PASA 12, 159

Hawley J.F., Gammie C.F., Balbus S.A., 1995, ApJ 440, 742

Hawley J.F., Gammie C.F., Balbus S.A., 1996, ApJ 464, 690

Pringle J.E., 1981, ARA&A 19, 137

Shakura N.I., Sunyaev R.A., 1973, A&A 24, 337

Stone J.M., Hawley J.F., Gammie C.F., Balbus S.A., 1996, ApJ 463, 656

Velikhov E.P., 1959, Sov. Phys. JETP Lett. 36, 995

Galaxy Collisions

Nils Tarras-Wahlberg

Department of Experimental Physics
Chalmers University of Technology and Göteborg University
SE-41296 Göteborg, Sweden
(tarras@fy.chalmers.se)

*

Abstract

I review galaxy collisions following Struck (1999) and major references therein.

References

Struck C., 1999, Phys. Rep. 321, 1

*Astrophysical Dynamics 1999/2000, Alessandro B. Romeo (Ed.), Onsala Space Observatory, 2000.

The Outflow-Disc Interaction in Young Stellar Objects

Michele Pestalozzi

Onsala Space Observatory
Chalmers University of Technology
SE-43992 Onsala, Sweden
(michele@oso.chalmers.se)

*

Abstract

In this work the most spectacular phenomena occurring during the formation of a star are briefly reviewed: accretion through a rotating disc of matter and outflow through the poles of the new stellar object. Magnetic fields have been proposed to be principally responsible for the coexistence of these opposed mechanisms of accretion and outflowing. According to different models, the magnetic fields are either twisted or stretched by the accretion disc, allowing the formation of polar channels through which part of the accreting matter can escape. The high degree of coupling between the physical parameters describing the young stellar object (e.g. circular velocity of the disc and the central object, viscosity, strength and freezing of magnetic fields, etc.) makes detailed understanding of the interaction between accretion discs and outflows very difficult. The models presented here provide only a partial answer to this difficult problem.

1 Introduction

Observing a main sequence star, like our Sun, but much further away with an optical telescope will not impress us much, since it will appear as an unresolved point source of light, without any particular feature. Main sequence stars are in fact objects in the most stable and quiet stage of their life. A slightly higher degree of activity (e.g. flares) can be observed at other wavelengths (e.g. radio or X-rays): synchrotron emission from the very hot plasma in the corona of the star is one of the most evident hints for the existence of strong magnetic fields rooted in the star. Nevertheless this activity is not comparable to the one through which the star had to go before reaching the quiet days of the main sequence. First the collapse of a molecular cloud, which can be of several light years in size. Then the accretion of matter through a disc accompanied by outflows (see Fig. 1). Finally the star reaches the stage of the ignition of nuclear fusion in its core which leads to emission at optical wavelengths, which will characterize its life on the main sequence.

I concentrate on the second phase mentioned above and explain, on the basis of both on theory and observations, the coexistence of two apparently opposite phenomena as

*Astrophysical Dynamics 1999/2000, Alessandro B. Romeo (Ed.), Onsala Space Observatory, 2000.

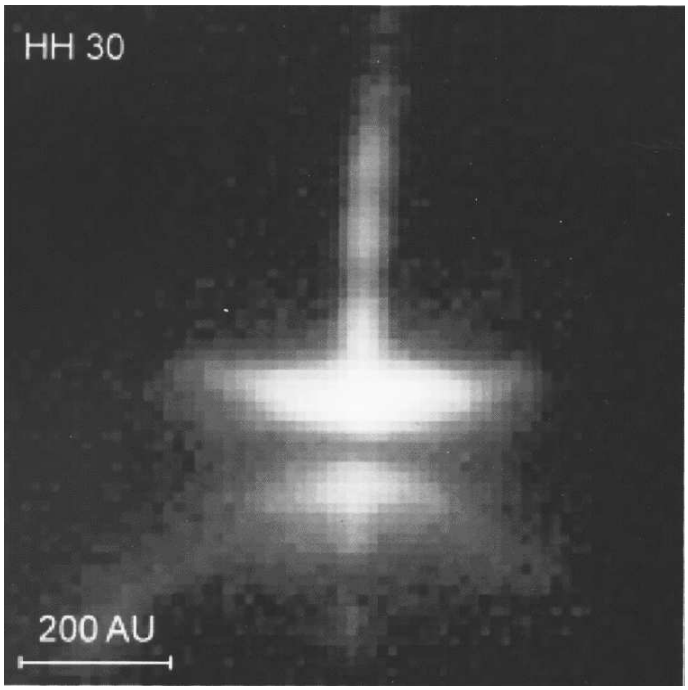

Figure 1: Single wavelength Hubble Space Telescope (HST) images do not give information about the dynamics of young stellar objects but they are able to constrain their geometry. Here is shown HH 30, a T Tauri star, with a disc and two opposite polar outflows. Picture taken from the NASA archive.

accretion and outflow of matter. To do this I will first introduce briefly (in section 2) the physical principles which are needed for such a study. I will then review a sample of theoretical models and the results of recent simulations (section 3). In section 4 I will draw the best links between the model predictions and the observed phenomena. As a summary, in section 5 I will try to delineate the further work in the field. The last section summarizes the discussion occurred at the end of the oral presentation.

2 Basic Equations

Magnetohydrodynamics is the study of the motions of a fluid in the presence of magnetic fields. We consider the material accreting and outflowing from a star as a fluid because the mean free path l of a particle is much smaller than the length of interest L (in our case $l \sim 10^{14}$ cm and $L \sim 10^{19}$ cm. We therefore will need a set of equations which include both the dynamics of a fluid and the presence of magnetic fields.

First the conservation of the *mass* from the hydrodynamic equations:

$$\frac{\partial}{\partial t}\rho + \nabla(\rho \mathbf{v}) = 0 \tag{1}$$

We then need an equation for the conservation of *momentum*:

$$\rho[\frac{\partial}{\partial t}\mathbf{v} + (\mathbf{v}\cdot\nabla)\mathbf{v}] + \nabla p - \rho\mathbf{g} = \frac{1}{4\pi}(\nabla \times \mathbf{B}) \times \mathbf{B} \tag{2}$$

Notice that the term on the right marks the presence of the magnetic fields with the magnetic force. p represents the pressure and $\mathbf{g}$ the gravitational potential (which can

have whatever shape we wish).
The *energy* equation looks like the following:

$$\frac{\partial}{\partial t}E + \nabla \cdot (E\mathbf{v}) = -\mathbf{g}\mathbf{v} + \frac{1}{4\pi}\eta \mid \nabla \times \mathbf{B} \mid^2 \tag{3}$$

where η corresponds to the electric diffusivity.
Finally we need *field equations*:

$$\frac{\partial}{\partial t}\mathbf{B} - \nabla \times (\mathbf{v} \times \mathbf{B}) = -\nabla \times (\eta \nabla \times \mathbf{B}) \tag{4}$$

$$\nabla \cdot \mathbf{B} = 0 \tag{5}$$

This set of equations needs a few lines of explanation. First, in magnetohydrodynamics (MHD) we assume *local neutrality*. Because of the very low density, the charged particles of both polarities (electrons and ions) are supposed to fill the same space equally. This does not rule out the existence of different drift velocities between the two species. It means that the currents exist but the electric fields can be neglected. Hence the Lorentz force looks like the following:

$$\frac{1}{c}\mathbf{J} \times \mathbf{B} = \frac{1}{4\pi}(\nabla \times \mathbf{B}) \times \mathbf{B} \tag{6}$$

Since the electric fields are considered small enough to be neglected, their changes in time are also negligible. So we have

$$(\nabla \times \mathbf{B}) = \frac{4\pi}{c}\mathbf{J} + \frac{1}{c}\frac{\partial}{\partial t}\mathbf{E} \tag{7}$$

where the last term will be equal to 0. In addition, if we rule out all dissipation effects ($\eta = 0$) because of the very low density of the plasma, we have the right hand side of equation (4) equal to 0. In that case we talk about field freezing, which means that the field lines follow every movement of the matter in which they are embedded, producing changes in the geometry of the magnetic field and in the strength of the magnetic flux.

The solution of this system of equations is a great challenge in both theoretical modelling and the numerical computation. It will trace the magnetic field lines around young stellar objects and meet the observations which have been carried out with all kind of techniques and at all wavelengths. In the next section we will have a look at the models which give the best fit to the observed data.

3 The Models

From the literature it is possible to recognize two major *schools* in modelling the magnetic fields around young stellar objects. The first (e.g. Shu et al., 1988) considers the outflows as centrifugally driven winds; the second stresses the twisting of the magnetic field lines.

3.1 Magnetocentrifugally Driven Outflows

Shu et al. (1988, 1991, 1994) proposed a model where the outflows detectable around young stellar objects are driven basically by the centrifugal force produced by the fast rotating central object. The latter is supposed to rotate nearly at break up speed. The poloidal magnetic field lines are squeezed towards the surface of the star, producing big

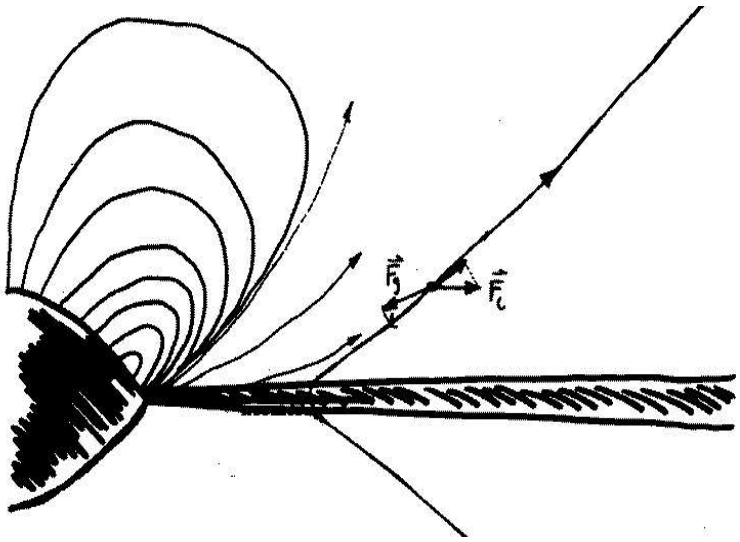

Figure 2: The model of magnetocentrifugally driven outflows by Shu et al. (1988). Note that, as a particle recedes from the star along a field line, the gravitational force $\mathbf{F}_g$ becomes weaker, whereas the centrifugal force $\mathbf{F}_c$ becomes stronger.

loops expanding along polar directions. The accretion disc drives the matter towards the star. Some of the matter travelling onto the disc surface to the star can leave the plane of the disc and fly along the squeezed field lines. In Fig. 2 it is possible to see the geometry of the field lines close to the central object and how the centrifugal force $\mathbf{F}_c$ wins over the gravitational attraction $\mathbf{F}_g$ the further the particle travels along the field line (Pelletier et al., 1992). The problem with this model is the collimation of the outflow. Observations show in some cases evidence for a very efficient mechanism of collimation of the matter flying away from the central object. This effect is not reproducible with this model. An example of an application of the model is given in Shu et al., 1994, on SU Aur a classical T Tauri star. $M_\star = 2.25 M_\odot$, $R_\star = 3.6 R_\odot$ give a mass flow from the disc $\dot{M}_D = 6 \times 10^{-8} M_\odot/yr$ and a magnetic field strength $B_\star = 300G$. The flow velocity will be around 200 km/s.

3.2 Twisting the Magnetic Fields

In the following models the mechanism that drives the outflows is not a wind created by the centrifugal force. The forces acting as launching the matter away from the central object are considered to originate only by the twisting of the magnetic field lines, which is able to open polar channels and draw matter from the accreting disc towards the interstellar space.

The first of these was proposed by Uchida & Shibata, 1985. It considers an interstellar magnetic field, frozen into the interstellar medium. Due to the collapse of the original molecular cloud the magnetic field lines are constrained to come closer to the central object, and because of the rotation of the accretion disc they will be twisted. The result is shown in Fig. 3. The twisting of the field leads to the appearance of a $\mathbf{J} \times \mathbf{B}$ force: $\mathbf{J}$ is radial due to infalling material, $\mathbf{B}$ leaves its initial configuration parallel to the rotation axis and, because of the twist due to the rotation of the disc, lies more and more in the plane of the disc. The $\mathbf{J} \times \mathbf{B}$ force is therefore oriented perpendicular to the disc and is able to produce large scale weakly collimated outflows. The collimated hot optical jets,

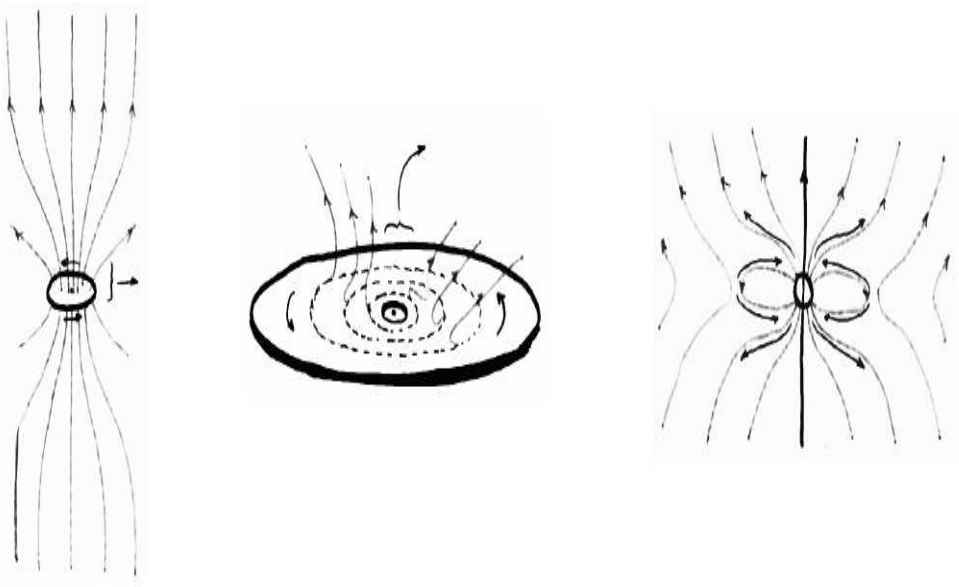

Figure 3: The model by Uchida & Shibata (1985). The three panels show a progressive zoom into the star formation region. Note in the right panel the *closed* and *opened* field lines.

on the other hand, are considered to have their origin closer to the star: material falling to the surface of the star can be blown off in the polar direction along the "open" field lines (these are not strictly open, they in fact reconnect with the interstellar field).

The second model comes from Newman et al. (1992) (Fig. 4). The important assumption here is $\mathbf{J} \times \mathbf{B} = 0$, which indicates a force free plasma. The Poynting theorem applied to this condition shows that because of the differential rotation of the disc (footpoints of the poloidal field travel apart form each other) the energy of the field has to increase. This energy enhancement causes the field lines to "inflate", especially in the direction of the poles. Material can then escape along the inflated field lines, away from the disc

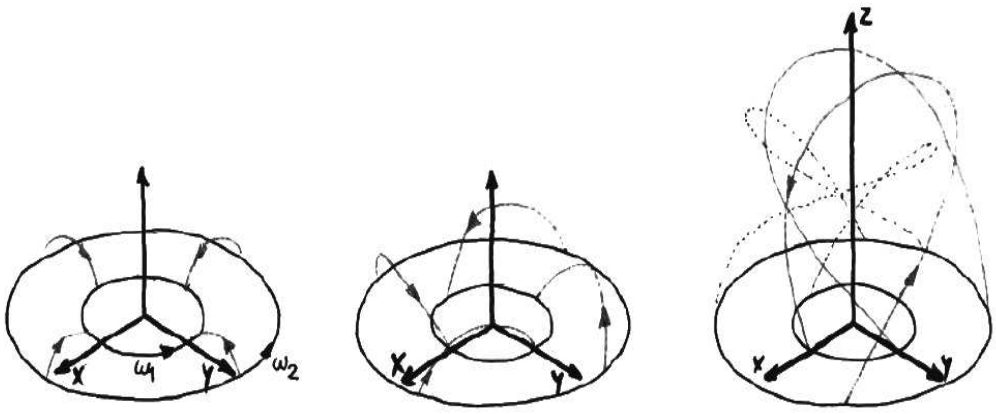

Figure 4: The Newman et al. (1992) model shows how differential rotation can twist the magnetic field lines, forcing them to expand in the polar direction. The time sequence starts from the left drawing.

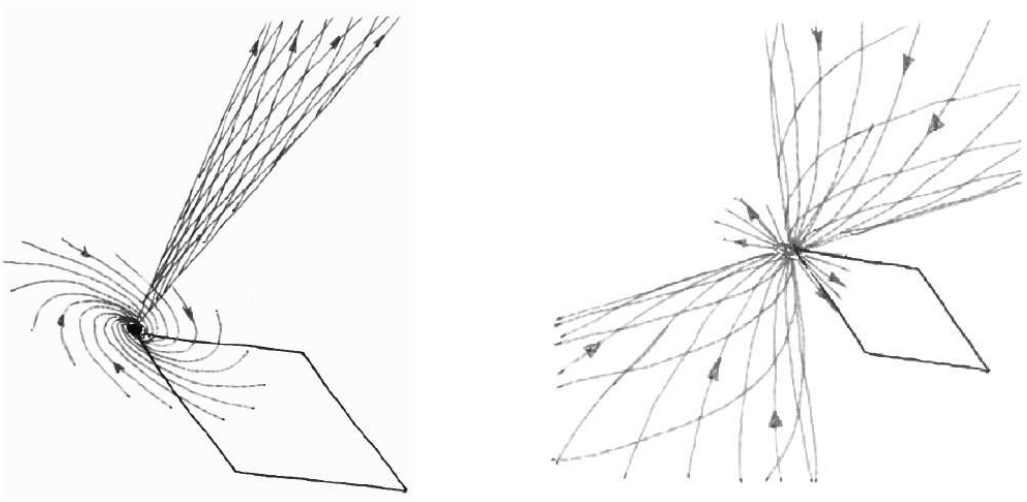

Figure 5: The Henriksen & Valls-Gabaud (1994) model lets open a more general scenario, even a polar inflow with equatorial outflow (right panel).

surface. Simulations by Lovelace et al. (1995) show that very little time is needed in order to reach a reasonable field inflating, which means that the phenomenon of outflow is present at the very beginning of the formation of the star, as soon as the accretion disc is present.

The third model was proposed by Henriksen & Valls-Gabaud (1994) and is called *cored apple*. It is explicitly said in the article that this model cannot reproduce any observation with high fidelity. Nevertheless it serves to show that no possibility can be ruled out. In particular their simulation shows, beside a known equatorial-infall-/polar-outflow-model, the opposite scenario of having a polar inflow (better called infall) and an outflow in the equatorial plane as (see Fig. 5). This mechanism is supposed to appear at the very beginning of the star formation, i.e. during the collapse of the molecular cloud, when yet no disc-like geometry has been created from the accreting material. Only a thick torus is present. The engine of the outflow is only the rebounding of the free falling material. It is even possible for some of the gas to miss the central object and to be directly conducted outwards. The model is however not able to reproduce field energies, pressures and flow velocities measured by observation, especially when the distance to the central object becomes greater than 100 AU (tests of the model have been carried out on VLA 1623, see Henriksen & Valls-Gabaud, 1994).

There have also been several attempts of modelling time-dependent accretion and outflow, see e.g. Goodson et al., 1997, 1999a, 1999b. They basically assume a radially oscillating disc, which periodically squeezes the poloidal magnetic field (field configuration of Newman et al., 1992), which inflates and allows material to flow out in the form of "bullets". The model is in good agreement with observations at different wavelengths of HH 30 (see Fig. 1) and DG Tau, two classical T Tauri stars. Further attempts of describing the material ejection time dependence claim to trace both the phenomena around a black hole and around a protostar (Ouyed et al., 1997).

The latest models are able to combine the existence of a fast, hot and narrow outflow (near to the rotation axis) with a slow outflow, colder and closer to the disc. The first would be driven by the dynamo action of the disc which gives raise to an azimuthal field, the second would be centrifugally driven. The former would be responsible for carrying

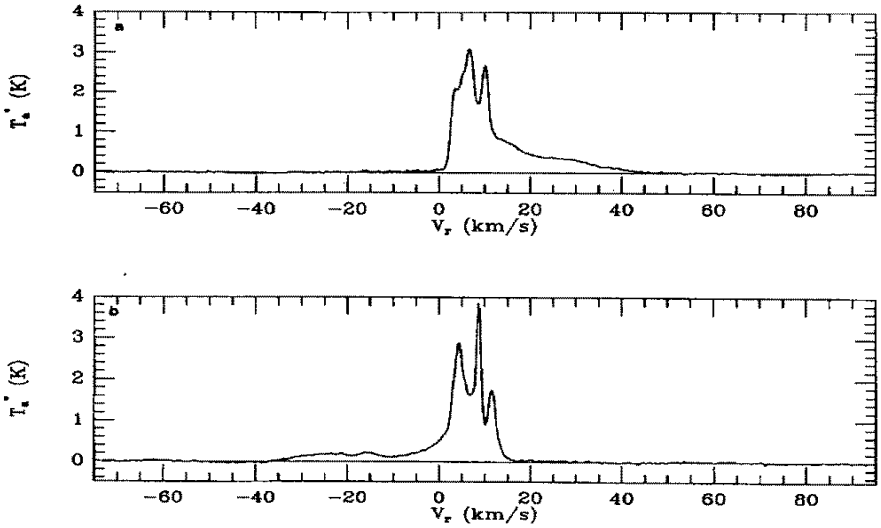

Figure 6: The emission spectrum of the CO transition $J = 2 \rightarrow 1$ towards the outflow in NGC 2264G. The upper panel shows the emission of the redshifted lobe of the outflow, the lower panel the emission of the blueshifted (Lada & Fich 1996).

material away from the disc, the latter to transport angular momentum outwards, along the disc (Brandenburg et al., 2000).

4 Observations: The Reality

From the pictures of the HST we get a static image of a forming star (Fig. 1). All information of the dynamics in that region is completely missing. In order to supply this information it is important to combine different techniques. In particular, I will present some results obtained from spectrometric studies of those regions at millimeter wavelengths. The reason for using radio observations instead of optical ones is simple: optical radiation is absorbed by the great amount of dust present around the central object; radio waves on the contrary get through and carry very important information about the interior of the cloud. Infrared observations are also important, since the dust scatters the UV-light from the star to longer wavelengths producing a *red excess*, i.e. a higher flux in the infrared than would be expected from the star. This excess radiation gives us information about the amount of dust around the forming star.

An observed spectral line will often be shifted in frequency, because of the relative radial velocity between us and the observed object (Doppler-effect). From the amplitude of that shift and from the shape of the spectral line it is possible to draw conclusions about the relative motion of the matter, e.g. if it is moving towards us or away from us. In Fig. 6 a typical spectrum is shown. Using an interferometer the data can be mapped in both space and velocity to study the source dynamics. Clearly noticeable is the velocity distribution of the matter at different distances from the central object (Fig. 7).

But even more useful for the study of the magnetic fields is the measure of the polarization of the light. By observing at millimeter and submillimeter wavelengths it is possible to measure the amount and direction of polarization as e.g. shown in the paper by Tamura et al. (1999). Dust particles aligned with the magnetic fields scatter UV-light from the star producing a slight polarization. In Fig. 8 one can see the orientation

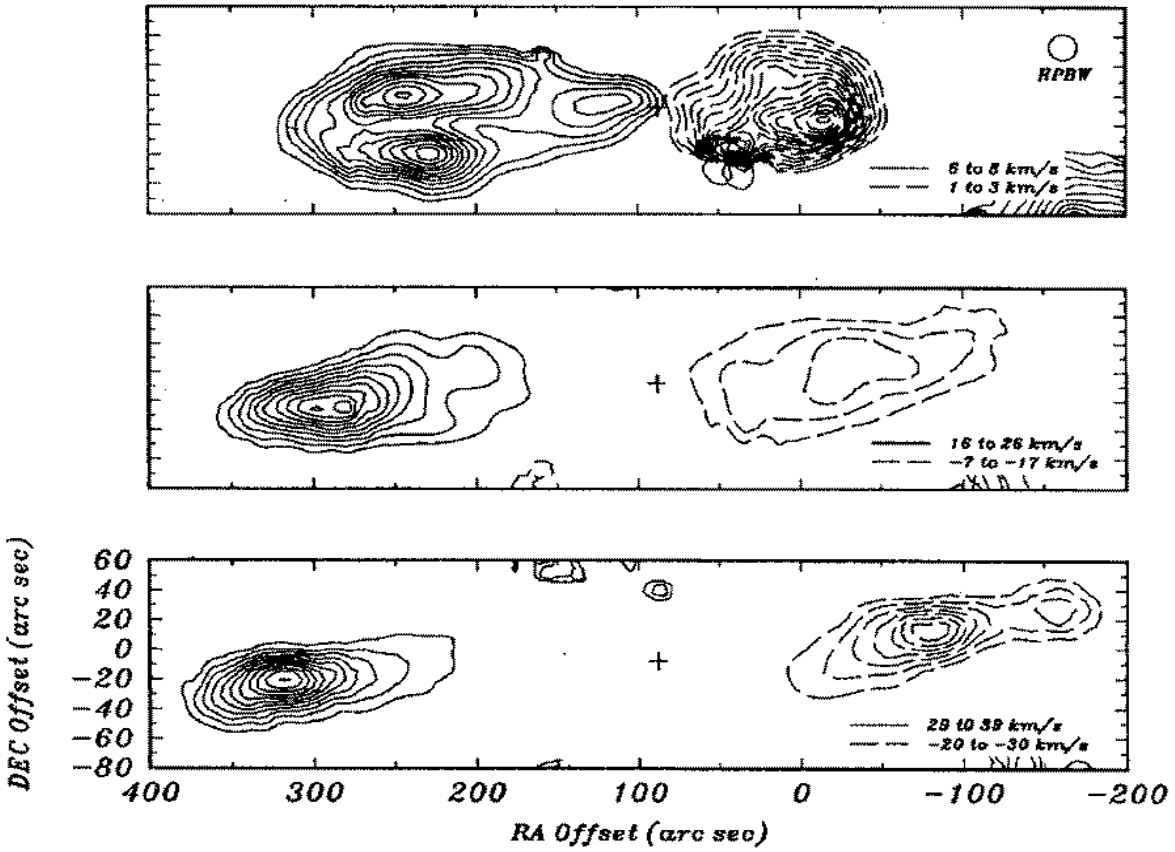

Figure 7: From the spectrum above it is possible to map the emission spatially: every slide corresponds to a range relative velocities, showing how the material is distributed both in space and velocity (Lada & Fich 1996).

of the polarization (thick line) superimposed on CO contours which traces the outflows. Realizing that the magnetic field is oriented along the disc, one can conclude that the toroidal component of the magnetic field is dominating the configuration around the two objects. It is also conceivable that determining the age of young stellar objects will be possible through measuring of the polarization: the more alignment with the accretion disc is detected, the older is the YSO (as time goes by the configuration is geometrically more defined and the magnetic field more twisted in the toroidal direction). A discussion about the possible correlation between "order" in the magnetic field and age is presented by Greaves et al. (1997).

The choice between one theoretical model and another is not always clear. Fig. 9 shows a plot of polarization against viewing angle. The latter is calculated based on geometrical considerations (see Greaves et al., 1997). The clear correlation between the polarization angle and the angle of view is striking and this suggested to the authors different conclusions about the geometry of the star-disc-outflows system. From the diagram in Fig. 9 one can see that when the outflow lies in the plane of the sky ($\Theta = 90^o$) the magnetic field lies perpendicular to the outflow direction. The opposite happens when the outflow is oriented close to the line of sight: the magnetic field seems to be parallel to the outflow. The authors test against the last three models of section 3. Though a definitive choice between models is not possible they can nevertheless possible to rule out one of them in some cases.

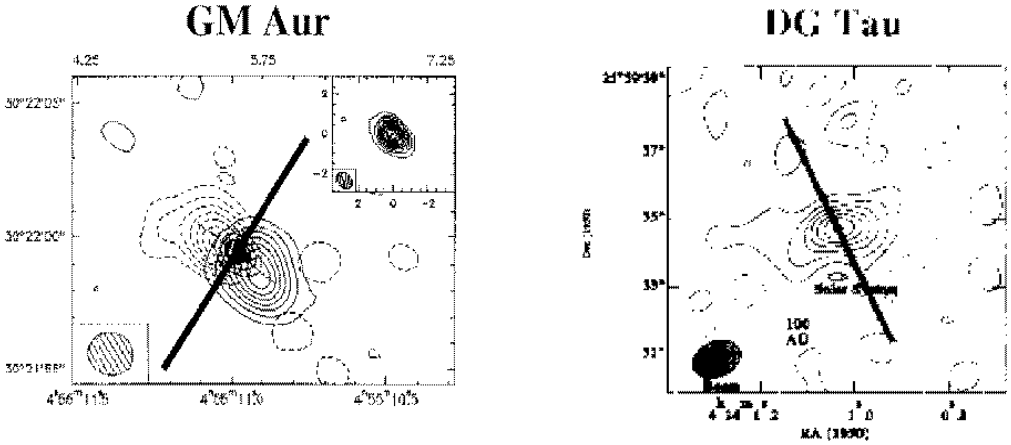

Figure 8: Two examples of a measurement of the polarisation of the mm or sub-mm continuum emission coming from young stellar objects (in this case two classical T Tauri stars). The thick line indicates the orientation of the magnetic field, which lies perpendicular to the outflows shown in the CO. One can conclude that the toroidal component of the magnetic field dominates the configuration around the YSO, indicating an advanced state of evolution (the magnetic field lines have been twisted for long time) (Tamura et al. 1999).

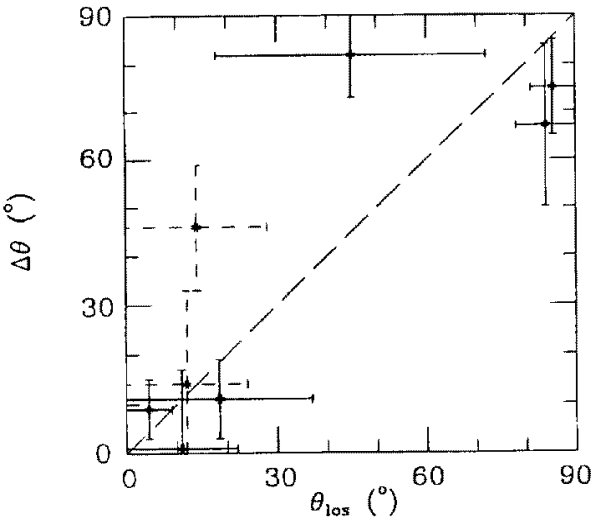

Figure 9: This diagram shows the correlation between $\Delta\Theta$ (angle between the magnetic field and the outflow direction) and Θ_{los} (angle between the outflow and the line of sight to the observer, estimated geometrically. From this diagram it is possible to determine the geometry of the object (Greaves et al. 1997).

5 What Remains to Be Done

In my opinion, the greatest challenge of the next generation of instruments (ALMA for the submillimeter, optical and infrared interferometry, etc.) is to achieve higher spatial resolution in order to be able to *zoom* into the deepest regions of the formation of a star.

Polarization measurements are also well suited to study the presence and the evolution of magnetic fields in star formation regions. All this will be a great contribution to the modelling of both jets from black holes and outflows from YSO's. In active stars (pre main sequence), the tracing of the magnetic fields can also be done by observing synchrotron emission from the plasma of the corona. These studies give insight into the existence and evolution of the corona in early phases of stellar evolution, in order to better understand the origin of e.g. the solar corona. An ongoing project tries in fact to detect T Tauri stars at very high resolution through synchrotron emission, with the aim of tracing the distribution of the hot plasma and consequently of the magnetic field.

6 Questions and Discussion

- **Student**: Where does the outflowing matter go? Does it come back on the star later on?

  M. Pestalozzi: The matter is blown away from the star and will in principle not participate in the formation of the star where it originated. Eventually it might be part of the formation of another star in the neighbourhood. When stars form in clusters the star formation rate is triggered exactly by this kind of phenomenon, which spreads out material into the interstellar space.

- **A. Romeo**: How does accretion occur?

  M. Pestalozzi: A single particle moving in a central field has a constant angular momentum. This fixes the characteristics of the orbits that the particle can have (the shorter the radius, the higher the rotation velocity). In order to fall towards the central object the particle has to lose angular momentum and energy, which in a YSO occur through the frequent collisions of gas particles. Research is in progress to understand how these dissipative phenomena are correlated.

- **A. Tappe**: Jets from a black hole and outflows from a YSO: are they the same phenomena? Will it be possible to join them in the same class?

  M. Pestalozzi: In the simulations by Ouyed, Pudritz & Stone (1997) the propagation of jets and outflows does not differ, except for the scale. However YSO and black holes are physically very different objects, especially close to the center. The unification of the theories describing outflows or jets is probably not possible at scales comparable to the size of the central object. Further out the morphology of the dynamics of the outflowing material have actually similar characteristics in both type of objects.

- **M. Thomasson**: How does polarization of light occur?

  M. Pestalozzi: Light coming from the star scatters on the dust particles which lie around the star (either in the disc or in general in the cocoon of the forming star). Magnetic fields on the other hand have the capacity of orienting the dust particles along the field lines, according to their magnetic properties: every elongated particle will feel a magnetic momentum, which will force the particle to assume the less

expensive position in terms of energy. In this situation, light which scatters with *oriented* dust will orient its fields, producing a polarization along the major axis of the dust particles.

- **M. Thomasson**: Where is the force that drives the matter out of the plane (e.g. in Newman et al., 1992)?

  M. Pestalozzi: In the model by Uchida & Shibata, 1985 it is the $\mathbf{J} \times \mathbf{B}$ force which increase with the twisting of the field lines by the rotation of the disc. In Newman et al., 1992, material follows the field lines which have been inflated by the stretching of the field lines due to differential rotation of the disc.

- **A. Tappe**: Open field lines: is this possible?

  M. Pestalozzi: What is meant by *open field lines* are not lines which will never close, opening the possibility to the existence of magnetic monopoles. These lines are supposed to reconnect with the lines of the interstellar magnetic field. They are virtually open for the central object we are considering.

- **A. Tappe**: Is it possible to tell which model is right and which is wrong? And if yes, how?

  M. Pestalozzi: No. There are better models and worse ones. The whole thing is about how well a certain model fits the observations. Some of the presented models are better for the explanation of some observations but not of others (see Greaves et al., 1997).

- **V. Minier**: You are speaking about low-mass star formation. What about high-mass star formation? Is any model possible for it?

  M. Pestalozzi: I was actually expecting that question. In my opinion that I have been cultivating during the preparation of this seminar, there should not be any difference between the formation of a low-mass star and a high-mass star, except for the scale of the phenomena. The problem comes from the time scale and the chance to observe a star in this phase: high-mass stars are supposed to form and evolve quicker than low-mass stars. This already puts a constraint on the *chance* of finding a high-mass star exactly in the evolutionary phase we would like. In addition, there are many more low-mass stars than high-mass ones. In any case, basing our consideration on the existent literature, I suggest to look at a high mass star formation applying Henriksen's model. Since it seems to be difficult for a 50 $M_\odot$ star to keep intact discs or other nice features, the model of outflows created only by the accretion seems to me the most appropriate to describe the early phase of evolution.

- **A. Tappe**: The collimation is proportional to the twisting, or better to the velocity difference between the rings where the footpoints of the magnetic field lie. Is that correct?

M. Pestalozzi: Yes. It is also well presented in the article to which I was referring. Actually in the proposed model the authors needed to turn the simulation only about a bit more than one turn in order to get those very pinched field lines.

- **D. de Mello**: On the HST viewgraphs you showed at the beginning a lengthscale is indicated. Could you compare it to the one you get observing with VLBI?

M. Pestalozzi: In fact with VLBI observation we are able to zoom in by about two orders of magnitude inside the objects we see in the HST picture. This seems to do all simulations about the magnetic fields useless and a comparison between HST images and VLBI data nonsense. In fact the simulations try to reveal real mechanism that starts the outflows, almost at the stellar surface. What we see with the HST images is a constraint on the geometry at a larger scale. The models must then be able e.g. to collimate the outflows within the distance form the central object that HST images indicate. Also the accretion mechanisms must obey those geometrical boundary conditions. In such complex problems of MHD in YSOs where all effects seem to couple (viscosity, accretion, outflow, magnetic fields, rotation, diffusion, ...) it is important to have at least some kind of boundary conditions on the geometry on which you can build a model.

References

Brandenburg A., Dobler W., Shukurov A., von Rebowski B., 2000, MNRAS, in press

Goodson A.P., Winglee R.M., Böhm K.-H., 1997, ApJ, 489, 199

Goodson A.P., Böhm K.-H., Winglee R.M., 1999, ApJ, 524, 142

Goodson A.P., Winglee R.M., 1999, ApJ, 524, 159

Greaves J.S., Holland W.S., Ward-Thompson D., 1997, ApJ, 480, 255

Henriksen R.N., Valls-Gabaud D., 1994, MNRAS, 266, 681

Lada C.J., Fich M., 1996, ApJ, 459, 638

Lovelace R.V.E., Romanova M.M., Bisnovatyi-Kogan G.S., 1992, MNRAS, 275, 244

Newman W.I., Newman A.L., Lovelace R.V.E., 1992, ApJ, 392, 622

Ouyed R., Pudritz R.E., Stone J.M., 1997, Nature, 385, 409

Pelletier G., Pudritz R.E., 1992, ApJ, 394, 117

Shu F.H., Lizano S., Ruden S.P., Najita J., 1988, ApJ, 328, L19

Shu F.H., Ruden S.P., Lada C.J., Lizano S., 1991, ApJ, 370, L31

Shu F.H., Najita J., Ostriker E.C., Wilkin F., 1994, ApJ, 429, 781

Shu F.H., Najita J., Ostriker E.C., Shang H., 1995, ApJ, 455, L155

Tamura M., Hough G.H., Greaves J.S., Morino J.-I., Chrisostomou A., Holland W.S., Momose M., 1999, ApJ, 525, 832

Uchida Y., Shibata K., 1985, PASJ, 37, 515

Jets from Herbig-Haro Objects

Jiyune Yi

Onsala Space Observatory
Chalmers University of Technology
SE-43992 Onsala, Sweden
(jiyune@oso.chalmers.se)

*

Abstract

Herbig-Haro objects appear as groups of small semi-stellar fuzzy nebulae with characteristic emission line spectra of hydrogen and forbidden low excitation lines of mainly [OI], [NII] and [SII]. They are considered to be manifestation of early stages of star formation, and their ubiquitous jets probe the mass ejection and accretion history of young stars. Jets in Herbig-Haro objects have a knotty substructure and show often considerable wiggling. The knots provide a means to measure transverse motions, and the large proper motions constrain the modelling of Herbig-Haro objects (e.g., shocked cloudlet, interstellar bullet, or stellar wind cavity models).

At this workshop I start with a brief historical backgound of Herbig-Haro objects and then discuss their spectra at different wavelengths as diagnostics of shock properties. Observational properties of jets are then discussed. Different types of shocks are briefly reviewed. As the main topic of my talk relating to this workshop, I discuss the structure of the so-called 'working surface'. When two fluids collide supersonically, the jets impact the ambient medium, producing two shocks: a shock in which material from the environment is accelerated, called the bow shock, and a shock in which the jet material is decelerated, called the Mach disk. The whole double shock structure is often called the working surface. The shocks may be separated by a contact discontinuity. A couple of models for the working surface are reviewed, and a more refined 'internal working surface' model is also introduced. Differences between radiative and adiabatic shocks, and between stellar and extragalactic jets are presented as well.

References

Biro S., Raga A., 1994, ApJ 434, 221

Blondin J.M., Konigl A., Fryxell B.A., 1989, ApJ 337, L37

Blondin J.M., Fryxell B.A., Konigl A., 1990, ApJ 360, 370

Burrows C.J., 1996, ApJ 473, 437

*Astrophysical Dynamics 1999/2000, Alessandro B. Romeo (Ed.), Onsala Space Observatory, 2000.

Hartigan P., 1989, ApJ 339, 987

Hartigan P., Bally J., Reipurth B., Morse J., 2000, In: Mannings A., Boss P.B., Russell S.S. (eds.) Protostars and Planets IV. University of Arizona Press, Tucson, in press

Heathcote S., Reipurth B., 1992, AJ 104, 2193

Reipurth B., 1999, PhD thesis, University of Copenhagen, Copenhagen

Reipurth B., Heathcote S., 1991, A&A 246, 511

Reipurth B., Heathcote S., 1992, A&A 257, 693

Origin and Propagation of Extragalactic Jets

Alessandro Laudati

International Master of Science Programme
Nanoscale Physics and Engineering
Chalmers University of Technology
SE-41296 Göteborg, Sweden
(mp98alla@dd.chalmers.se)

*

Abstract

I review the origin and propagation of extragalactic jets following Ferrari (1998) and major references therein.

References

Ferrari A., 1998, ARA&A 36, 539

*Astrophysical Dynamics 1999/2000, Alessandro B. Romeo (Ed.), Onsala Space Observatory, 2000.

Ionization Fronts and Photo-Dissociation

A. O. Henrik Olofsson

Onsala Space Observatory
Chalmers University of Technology
SE-43992 Onsala, Sweden
(henrik@oso.chalmers.se)

*

Abstract

The study of ionized regions in space has been going on for several decades. During these years, the field has branched out in many directions and the foci of interest have shifted over time. The article below is an attempt to cover the most important issues of the entire field from both theoretical and observational perspectives. Although a lack of space and time forces compromises in this ambition, the article hopefully can be used as an introduction to the subject, or as a quick reference for experts in adjoining research areas who simply have forgotten a key term or concept.

1 Introduction

The original intention with this paper was to first review the concept of *ionisation fronts*, boundary regions between ionized and neutral matter in space, and then focus in on a phenomenon often occurring in connection with such regions, namely photo dissociation, i.e., the destruction of molecules due to energetic photons.

As it turns out, ionisation fronts are for natural reasons closely related to *HII regions* which is simply the term used for volumes in interstellar space in which matter (hydrogen) is ionized. In order to understand ionisation fronts, it is proper to start by defining and describing HII regions in general.

Now, it quickly became apparent to the author of this article that

- The concept of HII regions is a complex one, especially when trying to relate theory with observations.

- The intended second part, the photo dissociation regions, is virtually a whole research field of its own and is not easily treated in a limited amount of time

*Astrophysical Dynamics 1999/2000, Alessandro B. Romeo (Ed.), Onsala Space Observatory, 2000.

We will here concentrate on the first part, which is more fundamental and perhaps more interesting from a thermodynamical point of view. The second part will be restricted to an example of a hot topic in connection with photo dissociation and its chemical effects.

The outline of the paper roughly follows that of a talk given at OSO in January, 2000. The following subject matters are dealt with in the sections of the paper:

- HII regions: Theory
- HII regions: Observables
- HII regions: Classification
- HII regions: A selection of complications and interrelations
- HII regions and PDRs: Example of a hot topic

The purpose of the penultimate section is to leave the reader with some hints about what needs to be taken into consideration if one wants to proceed beyond the very basic level of this article in the general topic of HII regions.

The last section will have to serve as conclusion of the paper as well.

2 The Standard Model of Expanding HII Regions

Most of this model review has been inspired by Shu (1992), but other works consulted are Yorke (1986), Dyson and Williams (1997) and Spitzer (1978).

The model concerns the formation of HII regions as a result of massive stellar births. Although the general applicability might be questioned (discussed later), most of the known types of HII regions are related to star formation or, at least, to stellar radiation.

Firstly, we need to define the model components:

Initial Model System. An infinite, homogeneous, atomic hydrogen gas cloud with constant temperature and number density. The figures usually assumed for the two aforementioned quantities are $T_0 = 100$ K and $n_0 = 100$ cm^{-3}, respectively.

Model Stimulus. A massive ("OB"[1]) star turns on instantly at $t = 0$ and will thereafter have constant luminosity (radiative power output), cf. Figures 1a) and 1b). Stellar size and gravity are neglected.

Model Constraints. In the model, we keep the temperature in the ionized gas at 10000 K at all times, a value well within the observed range for most real HII regions. This high temperature also implies that a radiative treatment of the problem will not be sufficient; gas dynamics must be employed.

The evolutionary process taking place after $t = 0$ can be divided into two phases[2]. These will be described chronologically (or "fairytale style") in the following two subsections. Time scale estimates for these phases will not be provided here (we refer to aforementioned references).

---

[1] O- and B-stars are samples of a stellar classification mainly depending on the effective surface temperature. O-stars have surface temperatures in the regime 30000–50000 K, while B-stars have lower values 10500–29000 K.

[2] There is in fact a third phase sometimes mentioned in this context, concerning a late time when the central star starts to wander off the main sequence. This phase will here be left out of the discussion altogether.

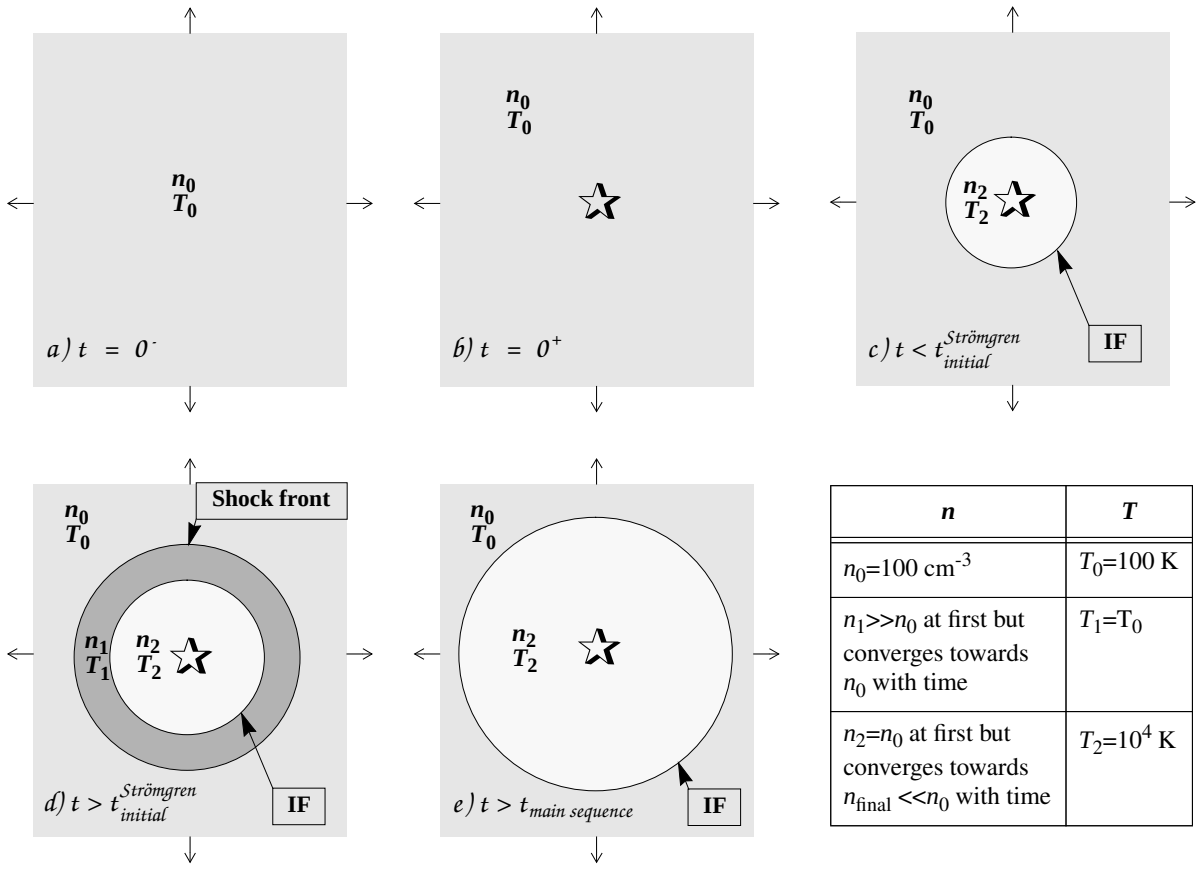

n	*T*
n_0=100 cm^{-3}	T_0=100 K
n_1>>n_0 at first but converges towards n_0 with time	T_1=T_0
n_2=n_0 at first but converges towards n_{final} <<n_0 with time	T_2=10^4 K

Figure 1: *a) to e):* A cartoon illustration of the evolutionary path of the standard model. The arrows at the edges of the figures indicate extension out to infinity. Proportions and scales are strictly schematic. *Table:* Lists the behaviour of the physical parameters denoted in the figures.

2.1 Stage A: The Formation Phase

At $t = 0$, the stellar radiation will start to ionize the gas isotropically outwards at a speed equal to photon speed (c_0). A spherical ionisation front (IF hereafter) is thus created, Figure 1c). After some time, when the photon density decreases due to volume expansion, recombination events start to become important affecting the speed of IF propagation. At the end of the first stage, the number of recombination events in the HII region will equal the number of ionizing photons released from the star. We can write this as

$$N_* = \frac{4}{3}\pi R^3 n_0^2 \alpha$$

where

N_* =number of ionizing photons[3] released per second from the star. Typical value (for an O5-star): 5.6×10^{49} s^{-1}

R =radius of the IF

n_0 =atomic hydrogen number density. Typical value: 10^2 cm^{-3}

[3]Photons beyond the *Lyman limit*, i.e., photons capable of ionizing hydrogens atoms in their electronic ground state ($\Leftrightarrow E_{photon} \geq 13.6$ eV).

α =recombination coefficient. Typical value: 2.6×10^{-13} cm^3 s^{-1}

n_0 is squared because the recombination rate depends both on proton and electron density and we assume $n_{\rm electron} = n_{\rm proton} = n_0$.

We can thus estimate a radius at the end of stage A:

$$R_{\rm initial}^{\rm Strömgren} = \left(\frac{3N_*}{4\pi n_0^2 \alpha}\right)^{\frac{1}{3}} \approx 5.6 \text{ pc}, \quad \text{using typical values}^4$$

This is called "the initial Strömgren sphere" and was first derived by Strömgren (1939). We have neglected any gas motion in this first stage, which is important in stage B.

2.2 Stage B: The Expansion Phase

The temperature of 10000 K inside the IF during stage A creates an overpressure as the IF progresses. However, since the gas has a certain dynamic reaction time and the IF in the beginning is moving nearly at the speed of light, the resulting pressure wave will be lagging the IF in stage A.

In stage B, the pressure wave has overtaken the IF and has turned into a shock front[5] since the speed of the pressure wave was the sound speed *inside* the IF, which is greater than the sound speed of the matter outside the IF[6]. Since the gas has now reacted dynamically to the pressure imbalance, the gas inside the shock front is set in outward motion. This means that the particle density at a given radius will decrease and consequently let photons penetrate farther out (the recombination rate goes down). Hence, the IF is allowed to continue to move outwards. The density of the material between the shock front and the IF will be high due to swept up material. See Figure 1d).

The shock front will race outwards until its amplitude vanishes (at infinity in the model). The IF will continue to expand until the ionized gas reaches pressure balance with the outside neutral material. Since the shock has dissipated at this time, the density of the outside material is once again the original one n_0 (the temperature outside the IF has remained at T_0 at all times since the shock was isothermal), Figure 1e). By comparing equations of state, we get:

$$2n_{\rm final}T_2 = n_0 T_0$$

The corresponding radius will be

$$R_{\rm final}^{\rm Strömgren} = \left(\frac{3N_*}{4\pi n_{\rm final}^2 \alpha}\right)^{\frac{1}{3}}$$

By combining these equations, we get $n_{\rm final} \approx .5$ cm^{-3} and $R_{\rm final}^{\rm Strömgren} \approx 200$ pc. This evolutionary state is doubtfully observed in the real universe, for various reasons. As already mentioned, the applicability (or fidelity) of the model will be discussed in a later section.

---

[4] 1 pc $\approx$ 3.26 ly $\approx 3\times10^{18}$cm

[5] An *isothermal* shock to be more exact. Briefly, that means that the temperature is the same in front of and behind the shock front, but not inside the shock front itself. See Shu (1992) or any advanced level textbook on gas dynamics.

[6] The sound speed (or c_s=$\sqrt{\frac{d\rho}{dp}}$) in the isothermal case depends only on temperature. Thus $c_s^{\rm T=10000K} > c_s^{\rm T=100K}$.

2.3 Further Details and Nomenclature

Certain names and quantities are essential to be familiar with if one wants to discuss the theory of HII regions quantitatively or read the literature in the field. A few of them will therefore be explained below (*without* any mathematical motivation; see references for deeper derivation/justification).

IFs are classified into two main groups, depending on one parameter:
The velocity at which matter flows into the IF from the outside, relative to the motion of the IF itself.

Mathematically, it can be shown that

$$\begin{array}{ccc} v_1 \geq v_R & \text{or} & v_1 \leq v_D \\ \text{“R-type”} & & \text{“D-type”} \end{array}$$

where $v_R > v_D$ are simply values delimiting the solution space for the relevant equations[7]. Note that the subscript “1” (as in v_1) indicates a quantity related to the matter outside the IF. This means that when considering a **stage A** IF using the subscripts adopted in the previous subsections, the v_1 above should be substituted for v_0.

A further subdivision depends on the density contrast behind and ahead of the IF. The two terms used in this case only signify how close the ratio $\frac{\rho_2}{\rho_1}$ is to unity *relative to the allowed range of values this ratio can take on.*

$$\begin{array}{rcl} \rho_2 \text{ closer to } \rho_1 \text{ in allowed range} & \Rightarrow & \text{“Weak”} \\ \rho_2 \text{ further away from } \rho_1 \text{ in allowed range} & \Rightarrow & \text{“Strong”} \end{array}$$

For R- and D-fronts, the shift from weak to strong takes place when v_1 takes on its extreme values v_R and v_D, respectively. At that point, they are called “critical”.

Now, it turns out that from $t = 0$, the evolution of the IF in the model discussed here, progresses as follows:

$$\text{Weak R-type} \longrightarrow \text{R-critical } (v_1 = v_R) \longrightarrow \text{D-critical } (v_1 = v_D) \longrightarrow \text{Weak D-type}$$

thus implying that v_1 has to change discontinuously from v_R to v_D. This is mediated by the aforementioned sudden passage of the pressure wave through the IF, which marks the transition from stage A to stage B.

3 Observables of HII Regions

The primary signpost of an HII[8] region is the bremsstrahlung, or “free-free emission”, produced in the plasma. The process responsible for this type of radiation is the acceleration of electrons by collisions with protons (see any literature on radiation theory, e.g. Rybicki and Lightman 1979 for a theoretical derivation, or Gordon 1988 for the applied case). This emission has a “hot” thermal profile for the frequency range where it is opti-

[7] The subscripts R and D stands for “rarefied” and “dense”, respectively.

[8] The notation HII is by definition referring to the characteristic line spectrum of singly ionized hydrogen; such a spectrum does H^+ of course not posess since free protons have no bound states.

cally thick[9], i.e., the intensity increases with frequency for low frequencies until it reaches the turnover frequency where the emission gets optically thin and the intensity starts to decrease with frequency. This usually happens at 1-10 GHz.

Another way of identifying and studying HII regions is through *recombination lines* (recommended reference: Gordon 1988). These lines are produced when electrons are cascading down along the electronic Bohr levels after recombining with a proton. The downward transitions are usually produced by spontaneous emission, but in some cases, for certain transitions, we need to invoke stimulated emission (i.e., maser[10] action) to explain observed lines. The most intense recombination lines are the α ($\Delta n = 1$) and β ($\Delta n = 2$) lines of hydrogen and helium.

In most types of HII regions, infrared (IR) emission (presumably from dust) is observed. The dust could be located outside as well as within the HII region (Natta and Panagia 1976) and is heated directly by the stellar emission (e.g. Garay and Lizano 1999). In addition, CHII and UCHII (defined below) often have an associated small but hot-profiled IR source (again, likely due to heated dust). It should be noted that the presence of a characteristic IR source is not an exclusive proof of an HII region (Menten et al., 1999).

Other indicators of ionized gas are collisionally excited forbidden lines from singly or multiply ionized metals[11].

4 Observational Classification of HII Regions

The attempt in this section to find a coherent classification scheme depending on a few observed properties, by browsing through a moderate amount of papers on the subject, admittedly failed to a certain extent. The list presented below is constructed fairly ad hoc. Part of the information gaps evident in this list might be due to the bias of using newer reference articles ($\sim$ last 25 years) rather than older. In other words, the author would like to warn the reader that some facts given here may be misleading or even outright wrong depending on misconceptions (as a result of too few good references found) but also very possibly due to diverging or ambiguous information given in references treating the same thing.

The references given here are often more of examples where the terminology is used or where the particular object type is discussed.

4.1 List of Types

Giant HII regions. Huge, irregularly shaped regions observed in other galaxies as well as in our own Milky Way. Sizes about 100-1000 pc (unclear). Are mostly connected with clusters of massive stars (OB-stars). Are probably merged collections of HII regions of smaller types. See e.g. Scheffler and Elsässer (1987).

Hollow HII regions. Somewhat more regularly shaped. Have a cavity inside them where also a few illuminating stars are located. Sizes about 50 pc. Further reading in Dorland et al. (1986).

[9] Optical thickness is very simplified a measure of the probability of a photon getting trapped before escaping from the region under consideration

[10] A maser is the microwave equivalent of a laser.

[11] Traditionally in astronomy, by "metals" are meant elements heavier than He.

Extended HII regions. Low electron density. Around 20 pc. Referred to in Garay and Lizano (1999) and observed in Garay and Rodríguez (1983).

"Normal" HII regions. Few references found, possibly because the attention over the last 30 years turned more towards compact HII regions (see below). Sizes on the order of 10 pc? In Churchwell et al. (1978) observed properties of what Garay and Lizano (1999) refer to as "typical" HII regions are provided.

Evolved HII regions. One to a few pc sized objects, regularly shaped but often elongated ("walnut" or "cometary" shaped). Associated with GMCs[12]. Includes "blister type" HII regions. E.g. Fich (1993) and Priestley and Hoare (1999).

Compact HII regions (CHII). Embedded in GMCs. Often spherical, but sometimes cometary or shellike. Sizes in the range .1-1 pc. E.g. Tieftrunk et al. (1997).

Ultracompact HII regions (UCHII). As previous, but smaller: $< .1$ pc. Sometimes cometary. E.g. Wood and Churchwell (1989) and Tieftrunk et al. (1997). Recent observations (Kurtz et al., 1999) suggest that the current conception of a UCHII is obsolete.

The electron densities for these categories roughly span over a range of $1–10^5$ cm^{-3}, increasing from top to bottom in the list.

In addition, there are

Diffuse HII regions. Weak emitters (either small and low density, or large and very low density). E.g. Scheffler and Elsässer (1987) and Tieftrunk et al. (1997).

4.2 Observations and Theory: Do They Match?

An easy way out would be to assign all the categories above (except the last one) to different evolutionary stages in the standard model ending with the first item on the list. All types smaller than $\sim$5 pc would then be stage A regions. The problem with this is that the compact and ultracompact types will be statistically overrepresented in observational counts when comparing with the short time an HII regions would spend being smaller than 1 pc (e.g. Garay and Lizano 1999).

A way to counteract this, is to invoke confinement mechanisms that keep the spacial extension of the region small over time. So called ram-pressure has been suggested as such a mechanism, see e.g. Shu (1992). Mass injection through photo evaporation is another (Garay and Lizano 1999, and references therein).

On the other hand, we know that we make an error by setting the initial number density in the model to a value that is typical for dense diffuse gas, when we know that HII regions in reality are formed within molecular clouds having core densities seven orders of magnitude higher. For example, by simply increasing the initial number density in the model by a factor of 1000, we get an $R_{\rm initial}^{\rm Strömgren}$ below a tenth of a parsec, thus implying that most compact HII regions are in fact stage B regions. A similar line of arguments is recited in Garay and Lizano (1999) in reference to earlier works.

A number of more or less plausible explanations exists in addition (see supplied review type references, e.g. Garay and Lizano 1999).

[12]Giant Molecular Clouds. Molecular gas cloud complexes with characteristic sizes of tens of parsecs and where formation of massive stars is taking place.

Further complications are that most material in GMCs is molecular, and not atomic, in its constitution, and that there may be strong temperature gradients present with an average well below the adopted 100 K.

Because of this and several other complexities hinted in the next section, the best applicability of the standard model (especially when using the initial conditions prevailing in the literature) is probably for regions which form near the end of the evolutionary cycle of the parent molecular cloud. The cloud is eventually destroyed or dissipated by the consecutive formation of many HII regions. This phase may begin with the formation of blister type regions[13]. Perhaps after this, HII regions are allowed to expand into the surrounding diffuse medium more according to the standard model, albeit one should keep in mind that the whole region of space has probably already been modified by one or many supernova explosions at this time.

5 Things to Worry about...

It would be futile, or perhaps impossible, to try to cover all aspects of HII regions and their connection to, and significance for, the rest of the universe. As a crude substitute, a bubble graph summary of complications that arise when reading through the literature, is shown in Figure 2.

Most certainly, there are things left out, but that is (un)fortunately inevitable in our universe where everything seems to depend on everything else.

One thing that deserves attention, and that has not been mentioned already, is the role of HII regions in the recycling process of matter in the galaxy. In particular, there is a scheme where the isotropic gas motion created by HII regions (which as we have seen can continue over hundreds of parsecs) pushes ionized matter out of the galactic plane, where it later cools and recombines, and then "rains" back and refuels the disc clouds with neutral material (Larson, 1996). Such a process could indeed be of vital importance for our understanding of galactic evolution in general.

The material on which Figure 2 is founded is virtually all the references given here (and listed at end), plus a few more: Garnett (1993), Maciel and Pottasch (1982), Lasker (1966), Tenorio-Tagle (1977), Tenorio-Tagle (1979), Gail and Sedlmayr (1979), Mac Low et al. (1991) concerning the respective topics "metallicity etc", "dust and heating", "magnetic fields", "shock effects", "champagne flow/density gradient", "dust and morpholoy" and "bow shock model".

6 Photo-Dissociation Regions

While the IF constitutes the boundary between ionized and neutral hydrogen, there is (in an HII region associated with a molecular cloud) a similar transition zone separating hydrogen atoms from hydrogen molecules. This zone is located outside the IF and is denoted *Photo Dissociation Region*, or PDR[14]. Good general references are Hollenbach and Tielens (1997) and Sternberg and Dalgarno (1995).

Since the atomic/molecular transitions take place at different radial distances for different elements and species, the term PDR is usually taken to mean the region from the

[13]The origin of blister type regions is still unclear and has been disputed over the last two decades. See included references.

[14]PDR is also somtimes taken to mean "Photon Dominated Region".

Figure 2: A bubble graph displaying some of the intricacies run upon when seeking deeper understanding of HII regions.

IF and out to a point where the chemistry or thermal balance is no longer heavily affected by penetrating energetic photons (Hollenbach and Tielens 1997).

The PDRs have been modelled extensively and currently account for a very active field of research. A few notes about PDR modelling will be provided below.

In the typical model, a far ultraviolet (FUV) field is injected into a semi-infinite molecular cloud through a planar interface. The resulting predictions suggest sharp transitions where different elements go from atomic to molecular form. The model takes into account such things as (photo)chemical reactions, several dust effects (physical and chemical), radiation transport and scattering, heating and cooling through atomic and molecular lines etc. Detailed models even include the clumpy structure of molecular clouds by letting photons scatter between the clumps in multiple directions (Meixner and Tielens 1993).

Surprisingly though, there seem to be little consideration of the fact that we, for a stage B HII region at not too late times, expect that an isothermal shock fairly recently has passed through the material ahead of the IF. The steady state solutions calculated by the models may not, loosely spoken, be the best reflection of the real situation in this case (molecular shock chemistry in general is treated in Mitchell 1984). Although Stoerzer and Hollenbach (1998) conclude that non-equilibrium effects are relatively minor (at least for a few observables), there is no discussion about potential shock effects.

Granted that most models (e.g. Draine and Bertoldi, 1996) in general aim to simulate a more general kind of PDR (for example cloud edges exposed to the interstellar radiation field), one would still think that there are scientific rewards in an attempt to apply PDR theory to the aforementioned special case.

In this context, it might be appropriate to mention that there are recent observations (Rodríguez-Franco et al. 1998; Greaves and Church 1996) of dense filaments in GMCs near IFs that belongs to fairly evolved HII regions. These filaments could in fact be interpreted as shock-compressed material. To find the filaments, a molecular tracer thought to be favoured by PDR processes, namely the CN radical, was used.

In case the last very up-to-date scientific result was not enough of an appetizer to trigger a deeper interest in the field, the author would like to conclude this paper by reciting a comment made in the discussion following the talk referred to in the introduction: "It could in fact be fruitful to try to find a true textbook case stage B region and look for the shocked envelope in various ways. If not found, it could be a serious challenge to the standard model. Similar studies were carried out several decades ago, but the far superior equipment today motivates renewed efforts."[15]

References

Churchwell E., Smith L. F., Mathis J., Mezger P. G., and Huchtmeier W., 1978, A&A 70, 719

Dorland H., Montmerle T., and Doom C., 1986, A&A 160, 1

Draine B. T. and Bertoldi F., 1996, ApJ 468, 269

Dyson J. E. and Williams D. A., 1997, The physics of the interstellar medium. Institute of Physics Publishing, Bristol

[15] At this, the speaker proudly replied that a blueprint for an observing proposal suggesting nearly the same thing had been produced by him not two days ago in response to an annoying inability to find any mention of observational evidence for shocked envelopes around stage B regions in the literature.

Fich M., 1993, ApJS 86, 475

Gail H. P. and Sedlmayr E., 1979, A&A 77, 165

Garay G. and Lizano S., 1999, PASP 111, 1049

Garay G. and Rodríguez L. F., 1983, ApJ 266, 263

Garnett D. R., 1993, PASP 105, 996

Gordon M. A., 1988, In: Verschuur G.L., Kellermann K.I. (eds.) Galactic and Extragalactic Radio Astronomy. Springer-Verlag, Berlin and New York, p. 37

Greaves J. S. and Church S. E., 1996, MNRAS 283, 1179

Hollenbach D. J. and Tielens A. G. G. M., 1997, ARA&A 35, 179

Kurtz S. E., Watson A. M., Hofner P., and Otte B., 1999, ApJ 514, 232

Larson R. B., 1996, In: The Interplay Between Massive Star Formation, the ISM and Galaxy Evolution, Proceedings of the 11th IAP Astrophysics Meeting, Editions Frontieres, Gif-sur-Yvette, p. 3

Lasker B. M., 1966, ApJ 146, 471

Mac Low M. M., van Buren D., Wood D. O. S., and Churchwell E., 1991, ApJ 369, 395

Maciel W. J. and Pottasch S. R., 1982, A&A 106, 1

Meixner M. and Tielens A. G. G. M., 1993, ApJ 405, 216

Menten K. M., Sridharan T. K., Wyrowski F., and Schilke P., 1999, In: The Physics and Chemistry of the Interstellar Medium. Proceedings of the 3rd Cologne-Zermatt Symposium, Zermatt, September 22-25, 1998, GCA-Verlag, Herdecke, p. 269

Mitchell G. F., 1984, ApJS 54, 81

Natta A. and Panagia N., 1976, A&A 50, 191

Priestley C. and Hoare M. G., 1999, In: The Physics and Chemistry of the Interstellar Medium. Proceedings of the 3rd Cologne-Zermatt Symposium, Zermatt, September 22-25, 1998, GCA-Verlag, Herdecke, p. 144

Rodríguez-Franco A., Martín-Pintado J., and Fuente A., 1998, A&A 329, 1097

Rybicki G. B. and Lightman A. P., 1979, Radiative processes in astrophysics. Wiley-Interscience, New York

Scheffler H. and Elsässer H., 1987, Physics of the galaxy and interstellar matter. Springer-Verlag, Berlin and New York

Shu F. H., 1992, The physics of astrophysics. Vol.2: Gas dynamics, A Series of Books in Astronomy. University Science Books, Mill Valley

Spitzer L., 1978, Physical processes in the interstellar medium. Wiley-Interscience, New York

Sternberg A. and Dalgarno A., 1995, ApJS 99, 565

Stoerzer H. and Hollenbach D., 1998, ApJ 495, 853

Strömgren B., 1939, ApJ 89, 526

Tenorio-Tagle G., 1977, A&A 61, 189

Tenorio-Tagle G., 1979, A&A 71, 59

Tieftrunk A. R., Gaume R. A., Claussen M. J., Wilson T. L., and Johnston K. J., 1997, A&A 318, 931

Wood D. O. S. and Churchwell E., 1989, ApJS 69, 831

Yorke H. W., 1986, ARA&A 24, 49

THE END

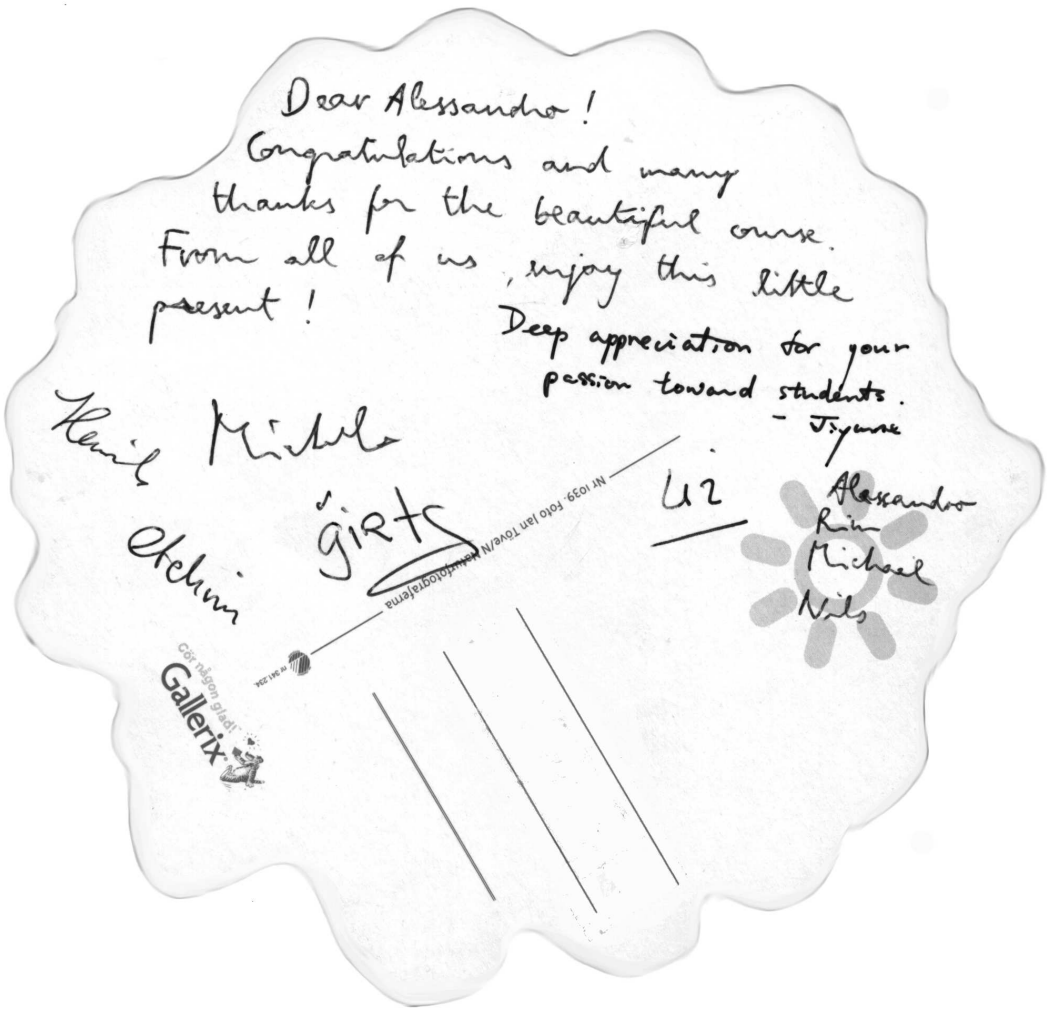

Mendelssohn *Symfoni nr 4, "Den italienska"*
Brahms *Pianokonsert nr 1*
DIRIGENT *Hans Graf*
SOLIST *Stephen Kovacevich* PIANO
Göteborgs Symfoniker

All my best wishes to all of you for
a happy life and a brilliant career !!!
Alessandro

... OR A NEW BEGINNING?